Environmental
Studies
Research
Fund

216

Analysis of Acoustic Particle Motion Data from the Svein Vaage Airgun Study

Analyse des données sur le mouvement des particules sonores de l'étude sur les canons à air de Svein Vaage

Canada 2018

Analysis of Acoustic Particle Motion Data from the Svein Vaage Airgun Study

Final Report

Submitted to:

Environmental Studies Research Fund
Project Identification Code: 2014-02S

Authors:

Graham Warner
Alexander MacGillivray
Bruce Martin

21 September 2018

P001276-001
Document 01656
Version 1.0

JASCO Applied Sciences (Canada) Ltd
Suite 2305, 4464 Markham St.
Victoria, BC V8Z 7X8 Canada
Tel: +1-250-483-3300
Fax: +1-250-483-3301
www.jasco.com

Suggested citation:

Warner, G.A. and A.O. MacGillivray. 2018. *Analysis of Acoustic Particle Motion Data from the Svein Vaage Airgun Study: Final Report*. Document Number 01656, Environmental Studies Research Funds Report Number 216, Version 1.0. Technical report by JASCO Applied Sciences for Environmental Studies Research Fund, Dartmouth, NS, Canada. 57 pp + appendices.

Disclaimer:

The results presented herein are relevant within the specific context described in this report. They could be misinterpreted if not considered in the light of all the information contained in this report. Accordingly, if information from this report is used in documents released to the public or to regulatory bodies, such documents must clearly cite the original report, which shall be made readily available to the recipients in integral and unedited form.

Contents

Figures

Tables

Executive Summary

This report is part of the Environmental Studies Research Fund Project 2014-02S final deliverables. The overall project objectives were to provide new results that will inform future environmental assessments of human activities on Canada's East Coast. The project was broken into two major programs:
1) measurement of the existing soundscape and the presence of vocalizing marine life; and
2) understanding the effects of the acoustic footprint of seismic surveys in the study area. Measurements of the soundscape were made continuously at 20 sites from Labrador to Nova Scotia over a two year period. To study of the effects of seismic sound, computer-based acoustic propagation modeling was performed that was validated by field measurements

The acoustic monitoring program deployed twenty marine acoustic recorders off Canada's east coast between August 2015 and July 2017 (Delarue et al. 2018). The recording protocol was selected to monitor marine mammal acoustic occurrence and characterize the underwater soundscapes of selected areas. The monitored locations ranged from the Scotian Shelf to the southern Labrador shelf through the Grand Banks of Newfoundland. The choice of monitored locations represents a balance between areas of potential interest for oil and gas development and less-sampled locations that were known or presumed to be important to marine mammals.

The underwater soundscape and its noise contributors were quantified. Drilling platforms contributed significantly to the local soundscape of targeted areas. Seismic survey sounds were detected over wide areas, particularly north of the Flemish Pass. Vessels were detected at all stations, with the highest vessel sound levels measured at stations near shipping lanes or near active drilling platforms.

The study provided unprecedented insight into the occurrence of marine mammals off Eastern Canada. Species richness was consistently higher at deep stations along the continental slope than at nearshore stations or at stations on the continental shelf. Stations in the southern parts of the study area maintained high species richness throughout the year, whereas northern stations saw a decline in winter and spring. The year-round presence of Cuvier's and Sowerby's beaked whales south of the Grand Banks and northern bottlenose whales north of the Flemish Pass and off southern Labrador, represents valuable new information. The year-round presence of sperm whales in the Flemish Pass area contrasts with the seasonal decline in detection rates observed throughout the study area in winter and highlights the area's potential importance for this species. Bearded, grey, and harp seal acoustic detections were associated with male sound production during the breeding season, when these species are most vocally active. Baleen whales showed pronounced seasonal variations in acoustic occurrence, which was attributed to the seasonality of their vocal behaviour, migratory movements, or both. Blue whales occurred nearly year-round in the Cabot Strait, and into January at most stations. In winter, they were common at deep offshore stations east of the Grand Banks. Sustained fin whale acoustic signals from September to March at most stations (excluding those with seasonal ice cover) indicates that this species does not migrate seasonally out of Canadian waters, as was traditionally believed. In summer and fall, sei whales regularly occurred at deep stations ranging from the Flemish Pass to southern Labrador.

This report is the first of two reports dealing with modeling of sound from seismic airguns arrays. Geophysical survey sources, such as seismic airguns, emit high-intensity sounds and have the potential to harm or disturb marine organisms. Sound fields from airguns are typically described in terms of sound pressure, but pressure is often not the most relevant parameter for assessing effects in non-mammalian species. For fishes and invertebrates, acoustic particle motion (the motion of an infinitesimal portion of the medium, relative to the medium as a whole) is more appropriate. It is known that all fishes are capable of directly sensing the particle motion component of sound, while relatively few fishes additionally sense the pressure component. Furthermore, animals such as crustaceans with statocyst-based hearing are thought to only sense particle motion. Because of increasing concern over the effects of anthropogenic sounds on these marine species, more complete descriptions of the sound fields to which animals are exposed are needed. The absence of ground-truthed models for acoustical particle motion from seismic airguns is an important knowledge gap that ESRF Research Study 2014-02S seeks to address.

In 2010, the Oil and Gas Producers (OGP) E&P Sound and Marine Life Joint Industry Program (JIP) commissioned PGS Geophysical to make extensive measurements of sound emissions from single airguns and airgun clusters at a deep fjord in Norway. The JIP study was named in honour of the late

Svein Vaage, a pioneer in the field of geophysical surveying. During the Svein Vaage study, PGS obtained detailed particle motion measurements at distances between 1 and 54 m from single airguns in order to characterize the near-field, high-amplitude particle motion that is most likely to cause biological effects. These measurements were obtained using a new type of particle motion sensor, called the M20, which was developed by Geospectrum Technologies Incorporated (GTI). The JIP shared a copy of the Svein Vaage dataset with JASCO, so that we could analyze the measurements and use them to improve and validate our particle motion models for seismic airguns.

Chapter 1 of this report presents the results of a detailed analysis of the Svein Vaage particle motion measurements. Our analysis found several issues with the calibration of the data from the M20 particle motion sensors, particularly with the absolute levels recorded on the accelerometer channels and in the logged positions of the sensors. Thus, we used measurements from several other calibrated hydrophones, which were deployed at the same time as the M20 sensors, to derive corrections for the sensitivities and positions of the M20 sensors. We also used information on the calibrations of the M20 sensors, provided by GTI, to correct the data for their frequency-dependent sensitivity. The results of this analysis were used to correct the identified issues and to obtain calibrated measurements of particle motion that could be used for subsequent airgun model validation.

Chapter 2 of this report presents model validation results for pressure and particle acceleration from single airguns using JASCO's Airgun Array Source Model (AASM). We performed the model validation using the Svein Vaage measurements, after applying correction factors for the M20 particle acceleration channels that we derived in Chapter 1. These results showed that AASM accurately predicted measured particle motion from single airguns, with best agreement between at frequencies below 300 Hz (i.e., where airguns generate most of their acoustic energy). Thus, AASM can be used for accurately modelling exposures of marine organisms to particle motion from seismic airguns at short range, which is particularly important for assessing potential impacts to fish and invertebrates.

The results of this study were used in Deveau et al. (2018), which contains the modeled acoustic footprints for hypothetical seismic surveys conducted near each of the monitoring locations and provides the radii to at which the sound levels exceed the (NMFS 2018) exposure thresholds for acoustic injury (temporary or permanent hearing threshold shifts). The modeling analysis also compared the results from modeling a generic sand bottom with a bottom whose geo-acoustic properties were obtained in Chapter 1. The modeling study concluded that use of local bottom properties is important for obtaining accurate propagation loss values and therefore realistic radii for possible acoustic injury and disturbance to marine life.

The propagation loss measurements analyzed in Chapter 1 were also analyzed to attempt to make direct measurements of particle motion from the single airgun. The data were of limited value because the airgun did not get close enough to the recorders to generate the particle motion effects of interest. Through a literature review and theoretical analysis it was determined that a full airgun array needs to be within ~50 m of the seabed to generate the interface waves of concern. Single airguns are unlikely to cause these effects in most situations. The lessons learned from the 2016 experiment were applied for the fall 2016 acoustic measurements of crab exposures to seismic sound. A detailed report on particle motion is contained in the report for that project (2014-01S).

Sommaire

Ce rapport est le deuxième de trois rapports finals du projet 2014-02S du Fonds pour l'étude de l'environnement. Les objectifs généraux du projet visaient à fournir de nouveaux résultats afin d'éclairer les évaluations environnementales futures des activités humaines sur la côte est canadienne. Le projet était divisé en deux grands programmes : 1) Mesure de l'environnement acoustique actuel et de la présence de vie marine qui contribue au paysage sonore et 2) Compréhension des effets de l'empreinte acoustique des relevés sismiques dans la zone d'étude. Les mesures de l'environnement acoustique se sont effectuées de façon continue à vingt sites situés entre le Labrador et la Nouvelle-Écosse au cours d'une période de deux ans. Pour étudier les effets des bruits sismiques, un modèle informatisé de la propagation sonore a été réalisé et il a été validé avec des mesures prises sur le terrain.

Le programme de surveillance acoustique a déployé vingt capteurs acoustiques sur la côte est canadienne entre août 2015 et juillet 2017 (Delarue et al. 2018). Le protocole d'enregistrement sélectionné visait à surveiller les activités sonores des mammifères marins et à caractériser l'environnement sonore sous-marin des zones sélectionnées. Les zones contrôlées se situaient entre la plate-forme néo-écossaise et le plateau continental sud du Labrador, en passant par les Grands Bancs de Terre-Neuve. Les choix de zones contrôlées constituent un équilibre entre les zones d'intérêt potentiel pour l'exploitation du pétrole et du gaz et les zones moins bien étudiées qui sont connues ou présumées importantes pour les mammifères marins.

L'environnement sonore sous-marin et les éléments qui y contribuent ont été quantifiés. Les plates-formes de forage ont contribué considérablement à l'environnement sonore local des zones ciblées. Le bruit des relevés sismiques a été détecté sur de vastes étendues, particulièrement au nord de la passe Flamande. Des navires ont été détectés à toutes les stations, et les stations près des routes maritimes ou des plates-formes de forage en opération ont affiché les niveaux sonores les plus élevés.

L'étude a fourni un aperçu sans précédent des activités des mammifères marins au large de la côte est du Canada. La diversité des espèces était toujours plus élevée au large de la pente continentale qu'aux stations littorales ou qu'à celles situées sur le plateau continental. Les stations situées dans les régions sud de la zone d'étude maintenaient une diversité des espèces élevée toute l'année, alors que celle des stations nordiques déclinait en hiver et au printemps. La présence à longueur d'année des baleines à bec de Cuvier et de Sowerby au sud des Grands Bancs et des baleines à bec au nord de la passe Flamande et au large de la côte sud du Labrador constitue de l'information nouvelle et précieuse. La présence à longueur d'année de cachalots dans la région de la passe Flamande contraste avec le déclin saisonnier des taux de détection observés dans l'ensemble de la zone d'étude en hiver et souligne l'importance potentielle de la zone pour ces espèces. Les détections acoustiques des phoques barbus, des phoques gris et phoques du Groenland ont été associées à la production de sons par les mâles pendant la période de reproduction, la période où ces espèces produisent le plus de son. L'activité sonore des baleines à fanons a démontré des variations saisonnières prononcées qui ont été attribuées au cycle saisonnier de leur comportement sonore, de leurs mouvements migratoires ou des deux. L'activité sonore des rorquals bleus a été décelée presque toute l'année dans le détroit de Cabot et jusqu'en janvier à la plupart des stations. En hiver, ils étaient de fréquemment détectés aux stations en mer profonde des Grands Bancs. La présence continue, de septembre à mars, des signaux sonores du rorqual commun à la plupart des stations (sans compter celles comportant une couche de glace saisonnière) indique que l'espèce ne quitte pas les eaux canadiennes de façon saisonnière, contrairement à ce que nous pensions. En été et à l'automne, la présence du rorqual boréal a été régulièrement détectée aux stations profondes de la passe Flamande jusqu'au sud du Labrador.

Ce rapport constitue le premier de deux rapports sur la modélisation de l'activité sonore produite par des batteries de canons à air lors de relevés sismiques. Les sources de levés géophysiques, comme les canons à air, émettent des sons à haute intensité et sont susceptibles de nuire aux organismes marins ou de les perturber. Les champs acoustiques produits par les canons à air sont généralement définis selon leur pression sonore, mais la pression n'est souvent pas le paramètre le plus pertinent en ce qui concerne l'évaluation de l'impact sur des espèces autres que les mammifères. Pour les poissons et les invertébrés, le mouvement des particules sonores (le mouvement d'une portion infinitésimale du milieu, relativement à l'ensemble du milieu) est un paramètre plus pertinent. Il est bien connu que tous les poissons ont la capacité de percevoir directement la composante du mouvement des particules d'un son, alors que relativement peu de poissons peuvent, en plus, percevoir la composante de la pression. De plus, on croit que les animaux, tels les crustacés dont l'ouïe repose sur le statocyste, ne perçoivent que le mouvement des particules. En raison des préoccupations croissantes relativement aux effets des sons d'origine anthropique sur ces espèces marines, il est essentiel d'établir des descriptions plus complètes des champs acoustiques auxquels sont exposés les animaux. L'absence de modèles témoins pour le mouvement des particules sonores produites par des canons à air constitue un manque de connaissance important que l'étude de recherche 2014-02S du FEE tente d'aborder.

En 2010, le programme conjoint de l'industrie (JIP - Joint Industry Program) sur les effets de l'exploration et de la production pétrolière et gazière en matière d'environnement acoustique et de vie marine a chargé PGS Geophysical de prendre des mesures complètes des émissions sonores produites par un canon à air unique et par des batteries de canons à air dans un fjord profond en Norvège. L'étude de JIP a été nommée en l'honneur de feu Svein Vaage, un pionnier dans le domaine des relevés géographiques. Au cours de l'étude Svein Vaage, PGS a obtenu des mesures détaillées du mouvement des particules produites par un canon à air unique, à des distances de 1 à 54 m, afin de caractériser le mouvement des particules de grande amplitude, du champ proche, qui est susceptible de causer des effets biologiques. Ces mesures ont été obtenues grâce à un nouveau type de capteur de mouvement de particules, le M20, qui a été mis au point par Geospectrum Technologies Incorporated (GTI). Le JIP a transmis une copie de l'ensemble de données de l'étude Svein Vaage à JASCO pour nous permettre d'analyser les mesures et de les utiliser à des fins d'amélioration et de validation de nos modèles de mouvement des particules produites par des canons à air sismiques.

Le chapitre 1 de ce rapport présente les résultats d'une analyse approfondie des mesures du mouvement des particules de l'étude Svein Vaage. Notre analyse a décelé plusieurs problèmes dans l'étalonnage des données des capteurs de mouvement de particules M20, particulièrement en ce qui concerne les niveaux absolus enregistrés sur les canaux accélérométriques et la position consignée des capteurs. Par conséquent, nous avons utilisé des mesures provenant d'autres hydrophones étalonnés, déployés en même temps que les capteurs M20, en vue de déterminer l'écart de sensibilité et de position des capteurs M20. Nous avons également utilisé l'information sur l'étalonnage des capteurs M20, fournie par GTI, afin de corriger les données de sensibilité qui varient en fonction de la fréquence. Les résultats de cette analyse ont servi à corriger les problèmes décelés et à obtenir des mesures étalonnées du mouvement des particules qui peuvent être utilisées pour vérifier de futurs modèles de canons à air.

Le chapitre 2 de ce rapport présente les résultats de vérification du modèle pour la pression et l'accélération acoustique provenant d'un canon à air uniques, à l'aide du Modèle de batteries de canons à air de JASCO (AASM – JASCO's Airgun Array Source Model). Nous avons effectué la vérification de modèle à l'aide des données de Svein Vaage, après avoir appliqué les facteurs de correction pour les canaux d'accélération acoustique M20, dérivés au chapitre 1. Ces résultats ont démontré que le modèle AASM a prédit avec exactitude le mouvement de particules mesurées d'un canon à air unique. La meilleure concordance s'est située aux fréquences inférieures à 300 Hz (c.-à-d. aux fréquences où les canons à air produisent la majorité de leur énergie acoustique). Par conséquent, le modèle AASM peut être utilisé pour adéquatement modéliser l'exposition d'organismes marins au mouvement de particule produit par des canons à air de courte portée, ce qui est particulièrement important pour évaluer les impacts potentiels sur les poissons et les invertébrés.

Les résultats de cette étude ont été utilisés dans l'étude Deveau et al. (2018) qui contient les empreintes acoustiques modélisées des relevés sismiques hypothétiques menés à proximité de chacun des sites de surveillance et qui indique le rayon où les niveaux acoustiques excèdent les seuils d'exposition ([NMFS] National Marine Fisheries Service 2018) susceptibles d'endommager l'ouïe (variations temporaires ou permanentes du seuil auditif). L'étude théorique a également comparé les résultats de modélisation d'un plancher océanique sablonneux avec un plancher dont les propriétés géoacoustiques ont été tirées du chapitre 1. L'étude de modélisation a démontré l'importance de tenir compte des propriétés du plancher océanique pour obtenir des valeurs d'affaiblissement de propagation précises et donc, des valeurs de rayons réalistes en ce qui concerne la perte de l'ouïe et la perturbation de la vie marine.

Les mesures d'affaiblissement de propagation analysées au chapitre 1 ont également été analysées dans le but d'obtenir des mesures directes du mouvement des particules produites par un seul canon à air. Les données se sont avérées d'une valeur limitée puisque le canon à air ne s'est pas assez approché des capteurs pour générer des effets de mouvement des particules qui présentaient un intérêt. Une revue de la littérature et une analyse théorique, ont permis de déterminer qu'une batterie de canons à air doit être à moins de 50 m du plancher *océanique pour générer les ondes d'interface qui présentent de l'intérêt. Dans la plupart des cas, il est peu probable que des canons à air uniques produisent ces effets. Les leçons retenues de l'expérience de 2016 ont été appliquées aux mesures acoustiques de l'automne 2016 sur l'exposition des crabes à des bruits sismiques. Le rapport de ce projet (ESRF 2014-01S) comporte un rapport détaillé sur le mouvement des particules.*

Chapter 1. Svein Vaage Data Analysis

1.1. Introduction

Exposure to high-intensity sounds from geophysical survey sources, such as seismic airguns, has the potential harm or disturb marine organisms in some circumstances. Sound fields are usually described in terms of sound pressure, but pressure may not be the most relevant parameter for assessing effects on non-mammalian species. Acoustic particle motion, the motion of an infinitesimal portion of the medium relative to the medium as a whole, may be more closely related to injury in fish and invertebrates (Popper et al. 2014). Unlike pressure, which is a scalar quantity with magnitude only, particle motion (displacement, velocity, and acceleration) is a vector quantity that includes both magnitude and direction. It is known that all fish are capable of directly sensing the particle motion component of sound (Fay 1984), while relatively few fish also sense the pressure component (Popper et al. 2003). Animals such as crustaceans with statocyst-based hearing are also thought to sense only particle motion (Mooney et al. 2012). Particle motion is used by fish and invertebrates for various biological functions, and noise exposure can cause behavioural response and even physiological damage at high levels (McCauley et al. 2000, Popper et al. 2007, Sarà et al. 2007, Mueller-Blenkle et al. 2010, Fewtrell and McCauley 2012, Halvorsen et al. 2012). Increasing concern over the effects of anthropogenic sounds on these marine species requires more complete descriptions of the sound fields these animals are exposed to. Understanding and predicting particle motion is therefore required for assessing impacts of anthropogenic noise on fish and invertebrates.

In 2010, the Oil and Gas Producers Joint Industry Program on Sound and Marine Life (JIP) contracted PGS to conduct the Svein Vaage airgun study, which involved pressure and particle motion measurements of underwater sound waves emitted by single airguns (Lundsten 2010). PGS made extensive measurements of Sercel G-guns with volumes of 60, 150, 380, and 520 in^3 at a deep fjord in Norway that included particle motion sensors at ranges of 1 to 54 m from the airguns. JIP shared a copy of these data with JASCO and, to date, these data have not yet been analyzed for particle motion. Far from an acoustic source and acoustic boundaries, there is a constant relationship between pressure and particle velocity, such that knowing the pressure is sufficient to determine the sound field. Near a source or acoustic boundaries, the relationship between pressure and particle velocity is more complex and additional information about particle motion is required to fully characterize the sound field (Popper and Hawkins 2018). For example, the acoustic pressure vanishes at the sea surface, but the particle motion does not. Fish, being sensitive to particle motion, can still determine the direction towards a sound source when near the surface. The JIP particle motion data were obtained close to individual airguns in a deep-water environment and can be used to characterize the near-field motion of high-amplitude particle motion that is most likely to lead to adverse biological effects, such as auditory system injury.

The purpose of this chapter is to summarize the PGS particle motion measurements. These measurements recorded pressure and particle motion data from seismic airguns using both hydrophones and accelerometers from various instrument manufacturers. Initial analysis of M20 accelerometer (GeoSpectrum Technologies Inc.; GTI) data from PGS showed that the digitization gains used during the study and the phase and frequency response of the M20 sensor did not result in physically-realistic data. JASCO therefore sub-contracted GTI to calibrate the M20 data into physical units (see GTI calibration report, Appendix A). The calibrated data from GTI were then analyzed by JASCO to calculate acoustic particle motion at different offsets from the airguns. In Chapter 2, the calibrated particle motion data from this chapter are used to validate the predictions of an acoustic model that calculates the three-dimensional particle velocity field from seismic airgun arrays.

1.2. Data Analysis Methods

1.2.1. Data Collection

PGS collected pressure and particle motion data for 25 sequences of shots from single airguns. Under controlled conditions, the airgun data were collected from an experimental barge located in a Norwegian fjord. The barge was instrumented with an array of acoustic sensors, and it was used to test the sound emissions from a variety of seismic airguns. An array of sensors recorded multichannel acoustic data in the form of 4-second digital traces, with one shot recorded per trace. A total of 14 traces were recorded for each measurement sequence, during which time the geometry of the sources and sensors were held constant. For each sequence, 10 traces corresponded to repeated shots of the airgun and 4 traces corresponded to background noise recordings. PGS's acquisition system converted the data from voltage to physical units before digitally storing the data in a custom SEG-Y format. Particle motion (M20) sensors were moved between sequences to measure a variety of horizontal ranges and depths, whereas reference hydrophones (B&K 8105, nominal sensitivity −205 dB re 1 V/µPa) were held stationary.

Our review of the PGS logs indicate that, during initial sequences where M20 data were collected (sequences 188–204), gains on the data acquisition system were actively modified, but not fully documented. Thus, due to the incomplete experimental logs, the data from these sequences could not be used for the current study. During later sequences (282–296 and 298–307), the data acquisition system was operated with consistent gain settings. We therefore restricted our analysis to the calibrated measurements obtained during the latter sequences. Data from M20 sensors numbered 2–4 contained clear recordings of airgun sounds and are analyzed in this chapter. Table 1 lists the sequence numbers with the corresponding airgun volume and M20 coordinates, as recorded in the experimental logs (also shown in Figure 1). The water depth was 500 m, and the study location was 100–300 m from shore.

The latter sequences involved Sercel G-guns with 150 or 60 in^3 volume that were operated at 6 m depth and pressurized to 2000 psi. Six M20 sensors were deployed for these sequences; however, signals on sensors 1 and 5 exceeded the voltage range of the acquisition system (i.e., they were clipped), so data from those sensors could not be analyzed. Furthermore, reviewing the traces from sensor 6 showed that this instrument recorded no useful data (Figure 2 shows pressure data from M20 sensor 6 hydrophone compared to a reference B&K hydrophone). Thus, only data from sensors 2, 3, and 4 were found to be of sufficient quality to include in subsequent data analysis.

Table 1. Sequence numbers, airgun volumes, and sensor coordinates, as recorded in the experimental logs. X and Y are horizontal coordinates (i.e., in the plane parallel to the water surface) and Z is the vertical coordinate (i.e., distance from the water surface). X = 0 and Y = 0 correspond to the airgun's x and y location, and Z = 0 corresponds to the water surface.

Sequence	Airgun volume (in^3)	Sensor 2 (m)			Sensor 3 (m)			Sensor 4 (m)		
		X	Y	Z	X	Y	Z	X	Y	Z
282	150	0	−2	6	−1	54	8	0	−2	16
283	150	0	−3	6	−1	54	7	0	−3	16
284	150	0	−4	6	−1	54	6	0	−4	16
285	150	0	−5	6	−1	54	5	0	−5	16
286	150	0	−6	6	−1	54	4	0	−6	16
287	150	0	−7	6	−1	54	4	0	−7	16
288	150	0	−8	6	−1	54	4	0	−8	16
289	150	0	−9	6	−1	54	4	0	−9	16
290	150	−2	0	6	−1	54	5	−2	0	16
291	150	−3	0	6	−1	54	5	−3	0	16
292	150	−4	0	6	−1	54	5	−4	0	16
293	150	−5	0	6	−1	54	5	−5	0	16
294	150	−6	0	7	−1	54	5	−6	0	16
295	150	−7	0	7	−1	54	5	−7	0	16
296	150	−8	0	7	−1	54	5	−8	0	16
298	60	0	−1	6	−1	54	8	0	−1	16
299	60	0	−2	6	−1	54	7	0	−2	16
300	60	0	−3	6	−1	54	6	0	−3	16
301	60	0	−4	6	−1	54	5	0	−4	16
302	60	0	−5	6	−1	54	4	0	−5	16
303	60	0	−6	6	−1	54	4	0	−6	16
304	60	0	−7	6	−1	54	5	0	−7	16
305	60	0	−8	6	−1	54	6	0	−8	16
306	60	0	−9	6	−1	54	7	0	−9	16
307	60	−8	−11	6	−1	54	8	−8	−11	16

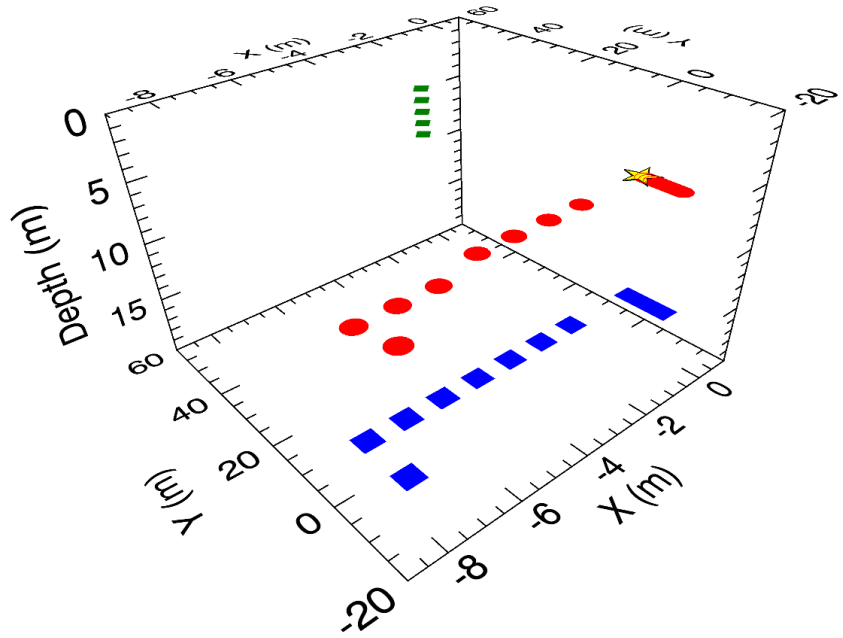

Figure 1. Measurement geometry for all sequences in Table 1. Red circles represent Sensor 2, green diamonds represent Sensor 3, Blue squares represent Sensor 4, and the airgun is represented by a yellow star.

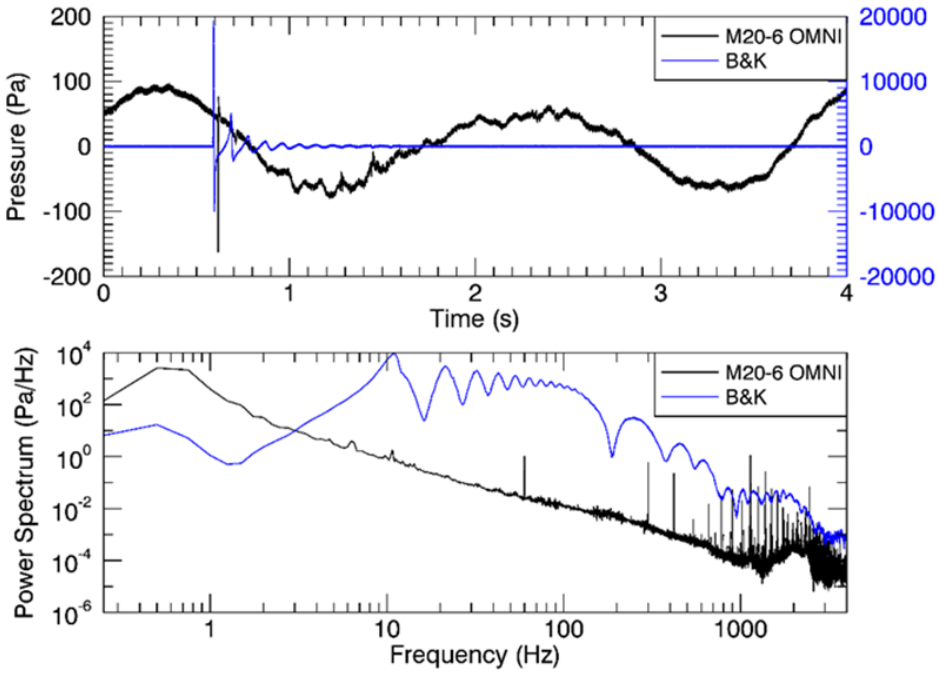

Figure 2. Example of (top) pressure traces and (bottom) power spectra for recordings of a 150 in^3 airgun made with M20 sensor 6 and a B&K reference hydrophone. The pressure traces are plotted on colour-coded vertical axes for display purposes. The B&K data clearly show the airgun signal, but data from M20 sensor 6 do not. Directional channels on this sensor did not contain airgun signals, so data from this sensor were not analyzed for this report.

1.2.2. Data Analysis Software

The airgun particle motion data from the JIP measurements were archived by PGS in a custom SEG-Y data format, which required specialized software to analyze. For this project, JASCO developed a flexible, extensible, GUI-based signal processing package (Figure 3) that included built-in support for reading and analyzing trace data in the specialized Svein Vaage SEG-Y format. JASCO's analysis software can apply sophisticated signal-processing algorithms to the particle motion data, including filtering, spectrum and cepstrum decomposition, and signal statistics. This custom software was used for reading, converting, and analyzing pressure and particle motion trace data from the Svein Vaage dataset. Additional custom data analysis scripts were created in the IDL rapid-development environment, which provides access to an extensive built-in library of signal processing algorithms.

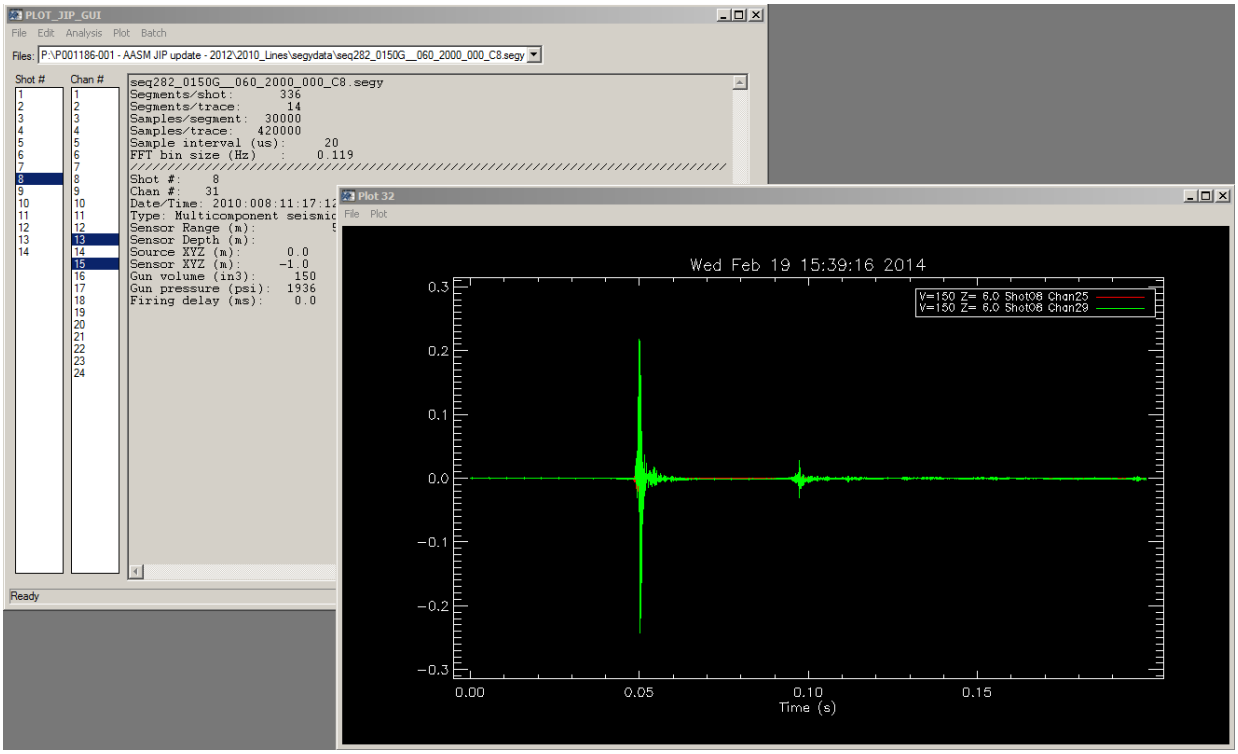

Figure 3. Screen capture of JASCO signal processing software used for reading and converting the custom Svein Vaage SEG-Y trace data.

1.2.3. Calibration

Data acquisition gains for the M20 sensors were included with the Svein Vaage field logs; however, they did not correctly account for the sensors' frequency-dependent magnitude and phase responses. At the time of the measurements (2010), the individual response curves for the M20 sensors were unknown; however, GTI calibrated the response of M20 sensor 3 in 2016. They calibrated the particle motion channels between 10 and 40 Hz using a shaker table, and the particle motion and pressure channels between 1 and 5 kHz in a test tank. JASCO therefore contracted GTI to correct the calibrations of the M20 pressure and particle motion data JASCO received from JIP (see GTI calibration report, Appendix A). JASCO provided GTI with the original data (in physical units) and the assumed sensitivity that was applied by PGS during the study to convert voltage into physical units. GTI converted the data into volts, using the assumed sensitivity and then applied the pressure and particle motion magnitude and phase response of M20 sensor 3 to data from all sensors (the magnitude and phase response of sensors 2 and

4 were unavailable, but assumed identical to those of sensor 3). GTI provided JASCO with calibrated pressure and particle velocity measurements in physical units.

Velocity data were then converted to acceleration for analysis; however, the magnitude of the acceleration data was not consistent with corresponding sound pressures measured on the calibrated M20 omnidirectional hydrophone (particle motion was at least 20 dB larger than expected, even at 54 m range from the source). We therefore assumed that an unknown frequency-independent gain had been applied to the directional sensor channels during the experiment. We estimated this gain by comparing particle acceleration spectra between the directional sensors and pressure measurements from the M20 omnidirectional hydrophones. For plane waves, particle acceleration can be shown to be equal to the time derivative of the impedance-scaled pressure:

$$|\mathbf{a}| = \frac{\partial}{\partial t}\left(\frac{p}{\rho_0 c}\right), \quad (1)$$

where $|\mathbf{a}|$ is the magnitude of acceleration, p is pressure, ρ_0 is the density of seawater, and c is the water sound speed.

The plane wave approximation of Equation 1 is expected to be valid at long ranges, where the curvature of the spherical waves generated by the airguns is small. Thus, this expression was used to estimate the missing gain factor in the M20 data by comparing the hydrophone and accelerometer measurements recorded on the most distant sensor (54 m range, Figure 4). The difference between spectral levels of the pressure-derived acceleration (i.e., right side of Equation 1) and directional sensor acceleration (i.e., left side of Equation 1) were computed for all traces of all sequences. Sequences 282–296 and 298–307 were found to have a constant (i.e., sequence- and trace-independent) spectral difference. We found that the spectral difference was approximately frequency-independent between 100 and 1000 Hz and the mean difference in this frequency range was −24.18 dB. We therefore concluded that directional sensor data for sequences 282–296 and 298–307 were missing a gain factor of 24.18 dB, which we then applied prior to subsequent processing.

While we do not expect the plane-wave assumption of Equation 1 to be valid at short range, we nonetheless computed a histogram of the spectral differences for all sensors (1 to 54 m range, Figure 5) to check whether the missing gain factor was consistent between sensors. As expected, the variances were larger when the comparison included all the sensors, but we found that the overall trend of the differences was the same. This indicates that that missing gain factor was likely the same between the three M20 sensors included in the comparison.

The spectral difference was frequency dependent at low frequencies (below ~50 Hz), which we believe was due to spurious low-frequency signals measured on the vertical channel (discussed further in Section 1.2.4). The M20 sensors were suspended from the surface by cables under tension, and were not neutrally buoyant, so we believe there were low-frequency resonances in the cables that introduced large-amplitude, low-frequency oscillations on the vertical channels. Figure 6 shows the spectral difference for the horizontal channels at frequencies up to 100 Hz, where the directional levels below 50 Hz exclude the vertical channel component. The spectral difference is only frequency-independent at lower frequencies when the vertical channel is excluded.

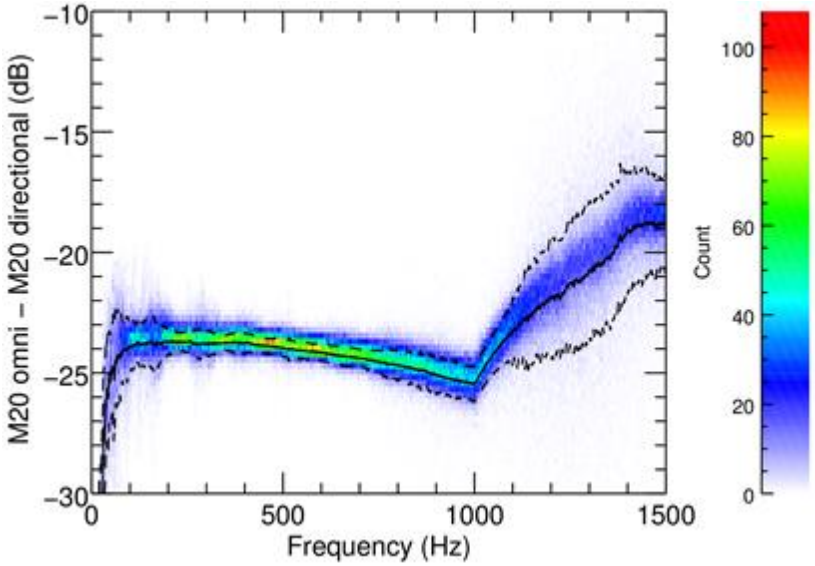

Figure 4. All traces and sensors at 54 m range in sequences 282–296 and 298–307: Histogram of the spectral differences between particle acceleration estimated from the M20 omnidirectional hydrophone and the M20 directional sensors. Solid line is the mean, and dashed lines are one standard deviation above and below the mean.

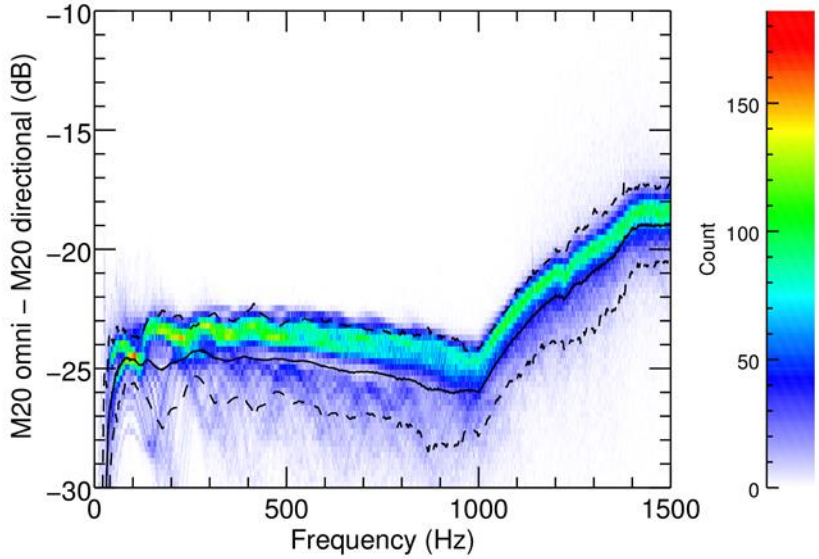

Figure 5. All traces in sequences 282–296 and 298–307: Histogram of the spectral differences between particle acceleration estimated from the M20 omnidirectional hydrophone and the M20 directional sensors. Solid line is the mean, and dashed lines are one standard deviation above and below the mean.

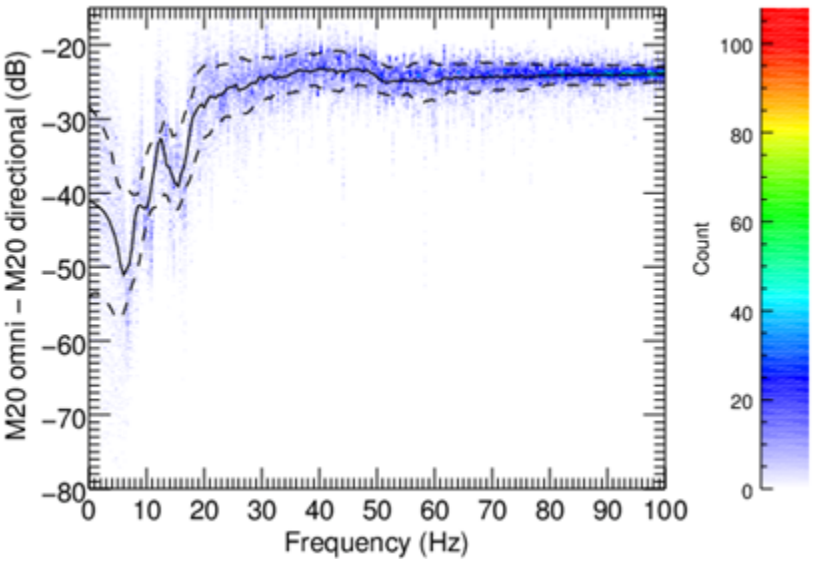

Figure 6. All traces and sensors at 54 m range in sequences 282–296 and 298–307: Histogram of the spectral differences between particle acceleration estimated from the M20 omnidirectional hydrophone and the M20 directional sensors (excluding the vertical channel data below 50 Hz). Solid line is the mean, and dashed lines are one standard deviation above and below the mean.

1.2.4. Filtering

Airguns produce high-amplitude sounds at low frequencies (below several hundred Hz), and the peak hearing sensitivity of most fish and sea turtles is below 1 kHz (Popper et al. 2014). Furthermore, the calibration in Section 1.2.2 shows an abrupt change in sensitivity between the M20 omni-derived and directional sensor acceleration at frequencies above 1 kHz which is due to sudden change in manufacturer supplied sensitivity (see Appendix A). For these reasons the data were low-pass filtered so that we only used data below 1 kHz for this analysis.

Review of the raw traces showed evidence of non-acoustic signals contaminating the acceleration data at low frequencies (below 30 Hz), particularly on the vertical channel. Figure 7 shows unfiltered acceleration traces in the vertical, radial, and azimuthal directions for a receiver at the airgun depth and at 4 m range. Persistent low-frequency oscillations can be seen in the vertical trace, which are most likely non-acoustic in origin. These vertical oscillations are believed to be caused be low-frequency resonances from the suspension of the negatively-buoyant M20 sensors. We therefore limited our analysis to frequencies above 30 Hz for the vertical channel and 10 Hz for the horizontal channels to avoid using potentially spurious low-frequency signals.

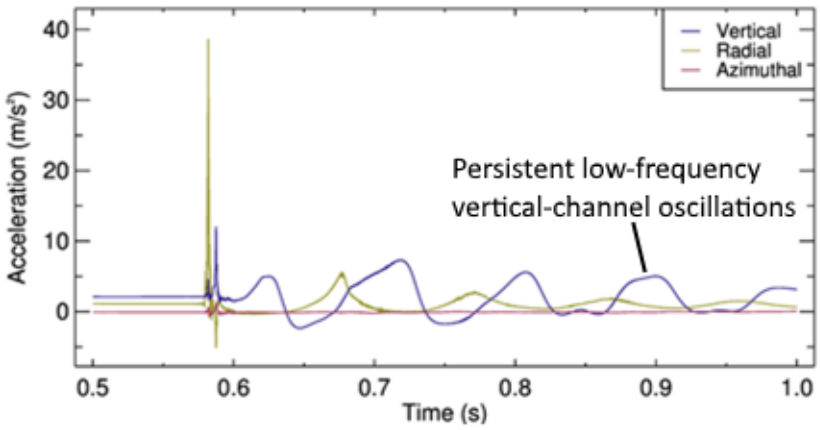

Figure 7. Sequence 292 at 4 m range: Unfiltered acceleration traces for 150 in^3 airgun data for a receiver at the airgun depth. Traces are offset vertically for display purposes.

1.2.5. Horizontal Directions

The M20 is a 4-channel sensor that consists of an omni-directional hydrophone and a 3-axis accelerometer. The accelerometers were oriented with one axis vertically (the upwards direction was positive) and the other axes oriented horizontally (denoted “sin” and “cos”). Compasses inside the M20 sensors would normally record the orientation of the sensors, but PGS disconnected them during the experiment to prevent electrical contamination of the acceleration channels (i.e., due to cross-talk between the digital and analog circuits). Thus, the azimuthal orientation of the horizontal axes was not recorded. During initial analysis, we found evidence that the horizontal orientation of the M20 sensor changed between sequences and, to a lesser degree, between some airgun firings in the same sequence. During processing, we applied a coordinate rotation to the trace data in the horizontal (X-Y) plane, using singular value decomposition, so that the radial direction corresponded to the axis of maximum particle motion and the azimuthal axis was perpendicular to the radial axis. The particle acceleration in the azimuthal direction had much lower amplitude than in the other directions, as expected, because the size of the airgun bubble is generally much smaller than the source-receiver distance (Landro 1992, MacGillivray 2006). The decomposition of the horizontal particle motion into the radial and azimuthal directions does not resolve the direction to the airgun (although it can be inferred at close range when radial motion is initially much larger away from the source than towards the source). This ambiguity has no effect on any of the particle velocity metrics in this report.

Inspection of pulse arrival times in the close-range data for M20 sensor 2 showed that the positions of this sensor were likely recorded incorrectly in the logs from PGS. Figure 8 shows pressure signals from M20 sensor 2 plotted side-by-side with signals from an AGH 7500C (nearfield) hydrophone (the signal amplitudes have been normalized to highlight differences in the peak arrival times). The AGH hydrophone was mounted on a 3-m-diameter ring, which was affixed to the source harness, so its range to the source (1.5 m) is known very accurately. In all sequences except 296, the time delays between the AGH signals and the M20 signals indicate that M20 sensor 2 was farther from the source than was recorded in the experimental logs (time delays for sequence 296 indicate the sensor was at 8.04 m slant range but the logs indicate the slant range was 8.06 m). For example, the signals for sequence 298 (where the M20 was closest to the source) show the airgun pulse arriving earlier on the AGH hydrophone than on the M20 sensor, despite the fact that the logs indicate the M20 was closer to the airgun (at 1.0 m range; ref. Table 1). The 1.3 ms time delay between the M20 and the nearfield hydrophone indicates that M20 sensor 2 was actually 2.4 m father from the source than was recorded in the logs during sequence 298. For sequence 306, the M20 signal is delayed by approximately 5.3 ms relative to the nearfield hydrophone, which indicates sensor 2 was only 0.3 m farther from the source than was recorded in the logs. The errors in the positions of M20 sensor 2 generally decrease with reported measurement range (see Section 1.3.1).

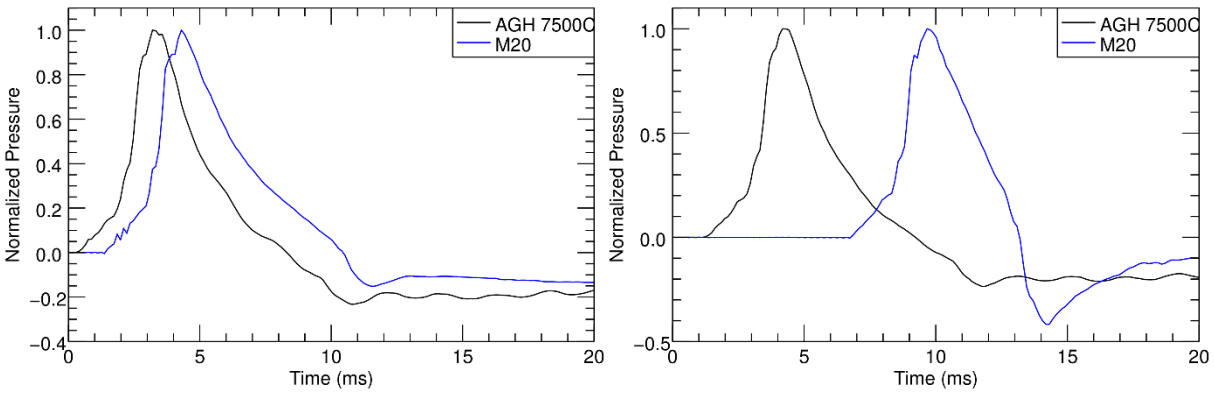

Figure 8. Normalized pressure signals recorded on the AGH 7500C (nearfield) hydrophone and M20 sensor 2 from sequences (left) 298 and (right) 306. The hydrophone signals were recorded simultaneously on the same time-synchronized data acquisition system. The AGH hydrophone was fixed at 1.5 m range and the logged range of the M20 was 1.0 and 9.0 m for sequences 298 and 306, respectively (ref. Table 1). The time delay of the M20 signal with respect to the AGH signal indicates that the actual ranges to the source were 3.4 and 9.3 m for sequences 298 and 306, respectively.

In subsequent sections of this chapter, plots and tables showing results of the data analysis have not been corrected for this range error unless specifically indicated.

1.2.6. Data Processing

Pressure and particle motion traces were obtained from the SEG-Y data files using JASCO's custom data analysis software (Section 1.2.2). Data were filtered (Section 1.2.4), and horizontal particle motion was decomposed into the radial and azimuthal directions (Section 1.2.5). Peak pressure and acceleration were calculated over a 1-second window containing the airgun signature. The same 1-second window was used to calculate rms acceleration spectra by taking the FFT of the time series. Acceleration spectra were summed over different frequency ranges and over different directions (e.g., horizontal, vertical, or total).

1.3. Data Analysis Results

1.3.1. Pressure versus Range

Figure 9 shows peak sound pressure versus slant range for all sequences from the 60 and 150 in^3 airgun that were measured on the three M20 sensors and two B&K hydrophones. The B&K hydrophones were positioned at 0 and 14.6 m horizontal range and 30 and 15 m depth, respectively.

Peak pressures measured on the B&K hydrophones appear ~4–5 dB higher than the peak pressures measured on the M20 hydrophones. The B&K hydrophones were at different locations than the M20 sensors, but the observed differences in the peak sound pressures could not be attributed to differences in the sound propagation at such short range. Thus, we suspect there may be an error with the pressure calibration or assumed data acquisition gain of the M20 omni channels. We believe the B&K hydrophones were more likely to provide reliable absolute pressure measurements, as their sensitivities were independently verified during the experiment by PGS using pistonphone calibrators.

Furthermore, the peak pressure levels measured on the M20 sensors at close range (1–17 m) follows 12.8×Log(range) and 14.5×Log(range) trends, which are inconsistent with the well-established 20×log(range) trend that should be measured at these distances (Ziolkowski et al. 1982). This inconsistency, along with the relative timing inconsistency between M20 sensor 2 and the nearfield hydrophones (ref. Section 1.2.5), suggests errors in the hydrophone locations recorded by PGS during the experiment. The plots also show the range-corrected M20 sensor 2 data from the nearfield hydrophone timing analysis, which are more consistent with the expected 20×log(range) trend.

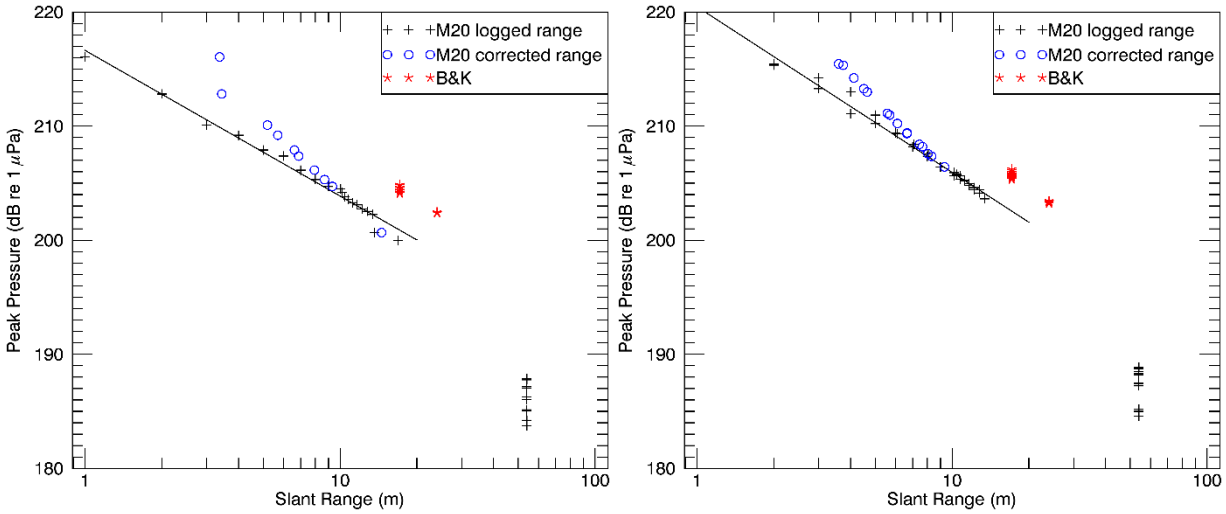

Figure 9. Peak pressure versus slant range for the (left) 60 in^3 and (right) 150 in^3 airguns. Peak levels are from unfiltered traces recorded on the omnidirectional hydrophone channel of three M20 sensors and two B&K hydrophones. Trendlines are shown for peak pressure levels measured on the M20 sensors at slant ranges less than 17 m. Peak pressure level decay trends are 12.8×Log(range) and 14.5×Log(range) for the 60 in^3 and 150 in^3 airguns, respectively. Range-corrected M20 sensor 2 data are shown with blue circles (ref. Section 1.2.5).

1.3.2. Acceleration Traces

Figures 10–14 show examples of acceleration in the vertical, radial, and azimuthal directions for the three M20 sensors for the 60 in^3 airgun data. For brevity, we only present data for two sequences where the receivers differed significantly in range (sequences 298 and 306). Table 2 lists the receiver ranges and depths for each figure.

Table 2. Receiver ranges and depths for the acceleration trace figures. The airgun depth was 6 m for all sequences.

Figure	Sequence	Horizontal range (m)	Depth (m)
10	298	1	6
11	306	9	6
12	298	1	16
13	306	9	16
14	306	54	7

The trace plots show that the source-receiver geometry largely influences the magnitude of the vertical and radial acceleration components (the azimuthal component is always relatively small). Radial acceleration is much larger than vertical acceleration when the receiver is at approximately the same depth as the airgun (Figures 10, 11, and 14), but the opposite is true for receivers at large depths relative to horizontal range (Figure 12).

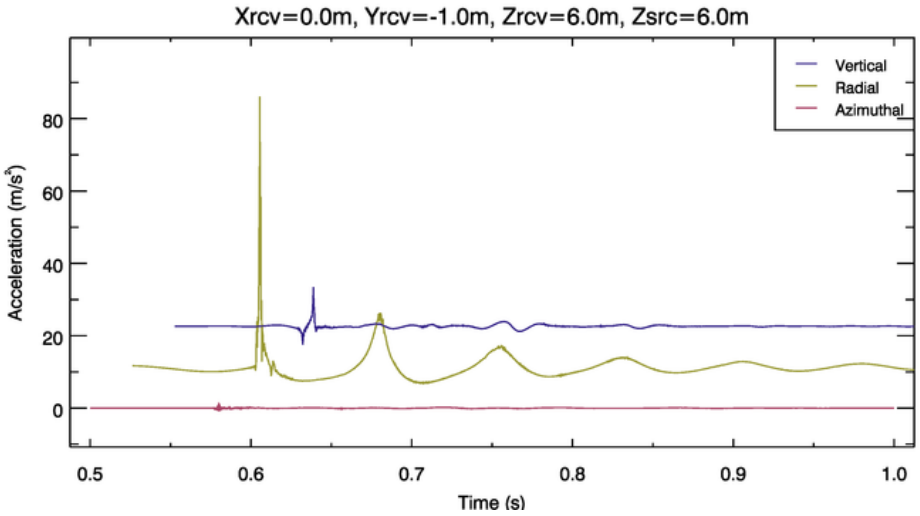

Figure 10. Sequence 298 at 1 m slant range: Acceleration traces for 60 in^3 airgun data for a receiver at the airgun depth. Traces are offset horizontally and vertically for display purposes. Band-pass filters of 30–1000 and 10–1000 Hz were used for the vertical and horizontal components, respectively.

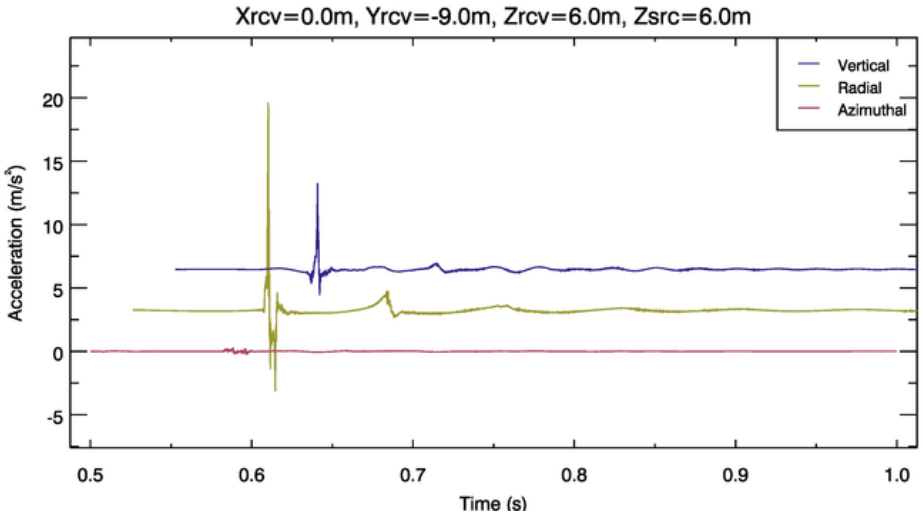

Figure 11. Sequence 306 at 9 m slant range: Acceleration traces for 60 in^3 airgun data for a receiver at the airgun depth. Traces are offset horizontally and vertically for display purposes. Band-pass filters of 30–1000 and 10–1000 Hz were used for the vertical and horizontal components, respectively.

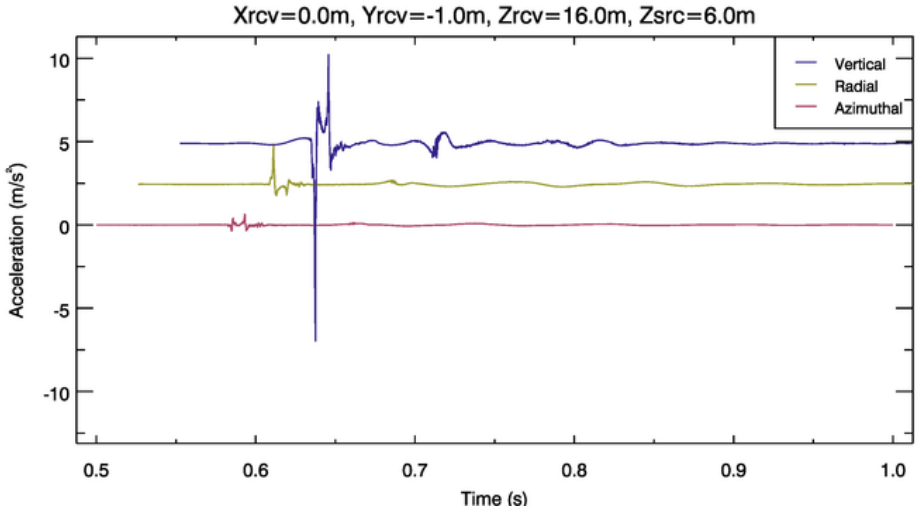

Figure 12. Sequence 298 at 10 m slant range: Acceleration traces for 60 in^3 airgun data for a receiver 10 m below the airgun depth. Traces are offset horizontally and vertically for display purposes. Band-pass filters of 30–1000 and 10–1000 Hz were used for the vertical and horizontal components, respectively.

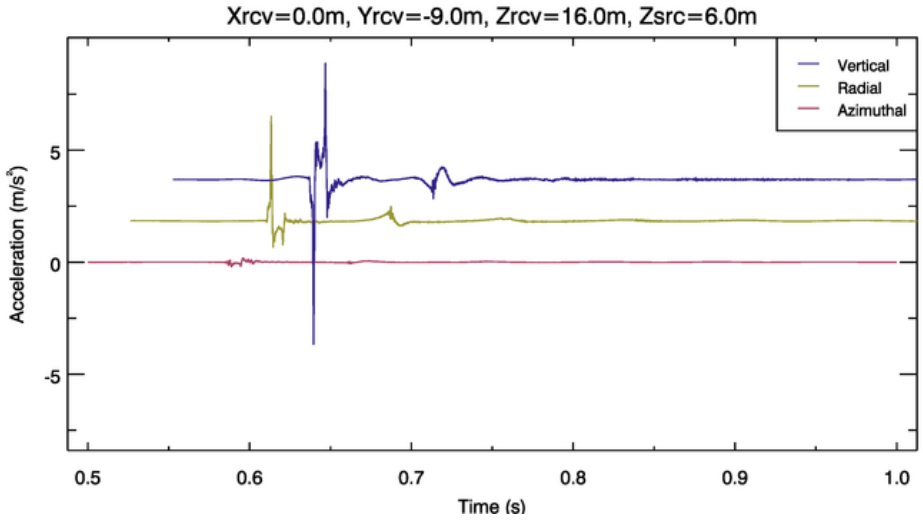

Figure 13. Sequence 306 at 13 m slant range: Acceleration traces for 60 in^3 airgun data for a receiver 10 m below the airgun depth. Traces are offset horizontally and vertically for display purposes. Band-pass filters of 30–1000 and 10–1000 Hz were used for the vertical and horizontal components, respectively.

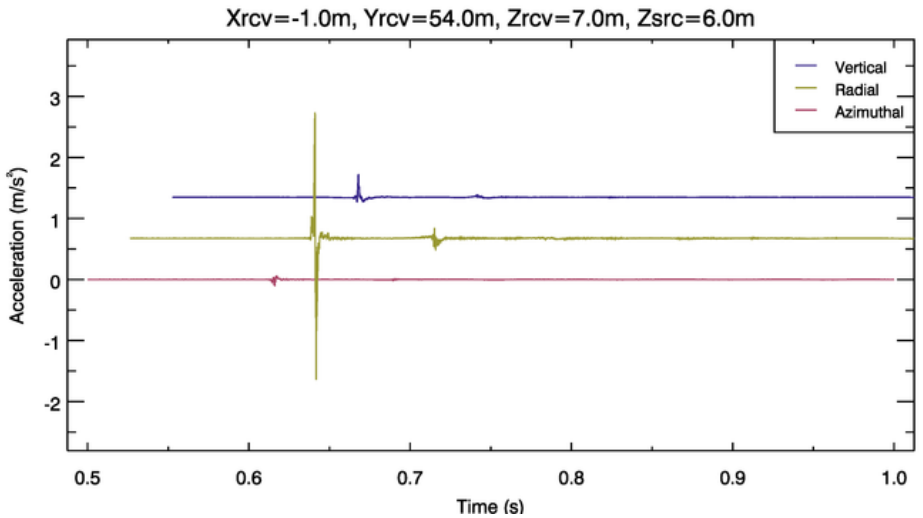

Figure 14. Sequence 306 at 54 m slant range: Acceleration traces for 60 in^3 airgun data for a receiver 1 m below the airgun depth. Traces are offset horizontally and vertically for display purposes. Band-pass filters of 30–1000 and 10–1000 Hz were used for the vertical and horizontal components, respectively.

1.3.3. Scatter Plots

This section contains scatter plots of acceleration and pressure for the receivers and sequences shown in Section 1.3.2. Plots show data from all 10 traces of each sequence containing airgun shots (i.e., traces 4–13). The airgun was fired at ~0.6 seconds into the 4-second recording. Each data sample is plotted in the scatter plots (time step of 0.1 ms). Acceleration traces (lower left panels) are offset vertically and horizontally for display purposes. Data were band-pass filtered between 10 and 1000 Hz (vertical acceleration data were band-pass filtered between 30 and 1000 Hz).

Particle acceleration traces in Figures 15 and 16 show acceleration and pressure measurements for a receiver at the airgun depth and at 1 and 9 m range, respectively. The vertical versus radial acceleration plots (upper-left panels) show large positive acceleration in the radial direction associated with the direct source-receiver path, followed by a smaller acceleration at different angles towards the surface that are associated with the surface-reflected path. The surface-reflected component has larger grazing angles for closer-range receivers, and the magnitude ratio between this component and the direct path increases with range. The surface-reflected component is greater towards the source and surface because pressure and particle motion are inverted (180° phase shift) upon reflection.

For deeper receivers (10 m below the airgun depth; Figures 17 and 18), the arrival angles between the direct and surface-reflected paths are more similar and the amplitude differences are not as large because the path length differences are smaller. At 54 m range (Figure 19), there is relatively little acceleration in the vertical direction and the direct and surface-reflected components have approximately the same amplitude and grazing angle.

The relationship between acceleration and pressure is shown on the right panels. The particle motion follows a nonlinear locus (i.e., path) in the vertical acceleration-pressure plane, due to acceleration and pressure being 90° out of phase.

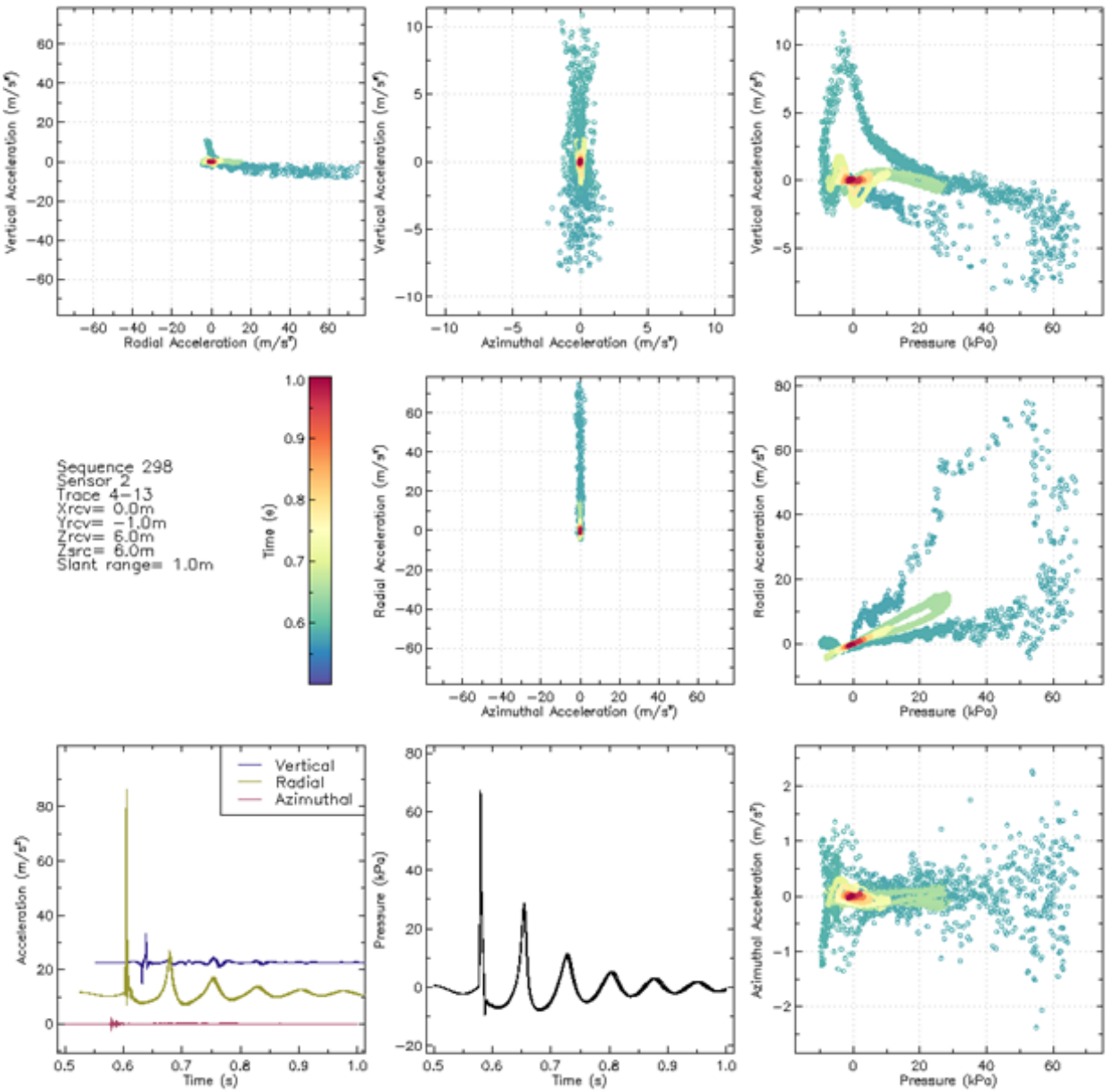

Figure 15. Receiver at the airgun depth and 1 m range: Particle motion and pressure scatter plots for 60 in^3 airgun data. Acceleration traces (lower left panel) are offset vertically and horizontally for display purposes. Data were band-pass filtered between 10 and 1000 Hz (vertical acceleration data were band-pass filtered between 30 and 1000 Hz).

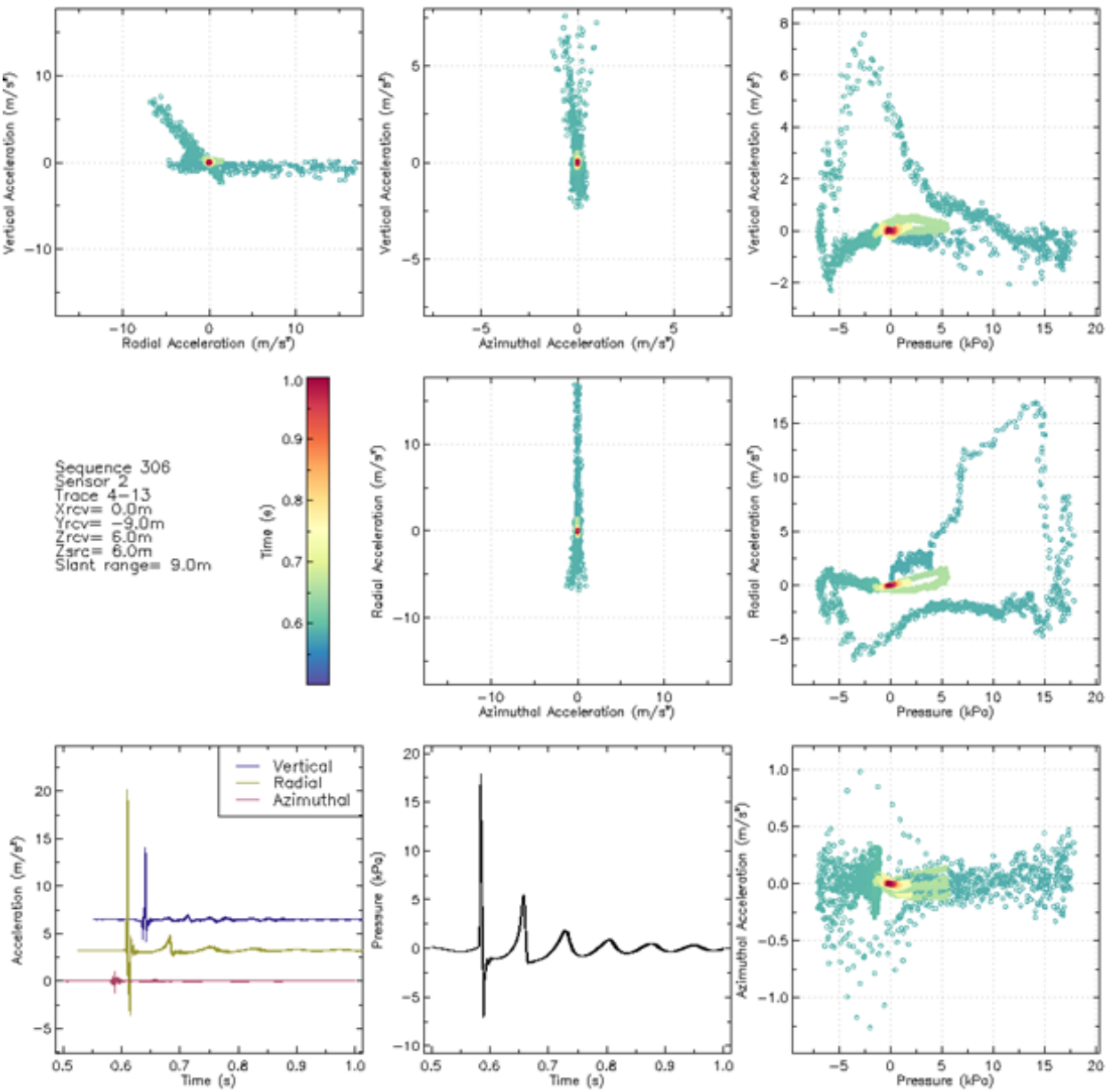

Figure 16. Receiver at the airgun depth and 9 m range: Particle motion and pressure scatter plots for 60 in^3 airgun data. Acceleration traces (lower left panel) are offset vertically and horizontally for display purposes. Data were band-pass filtered between 10 and 1000 Hz (vertical acceleration data were band-pass filtered between 30 and 1000 Hz).

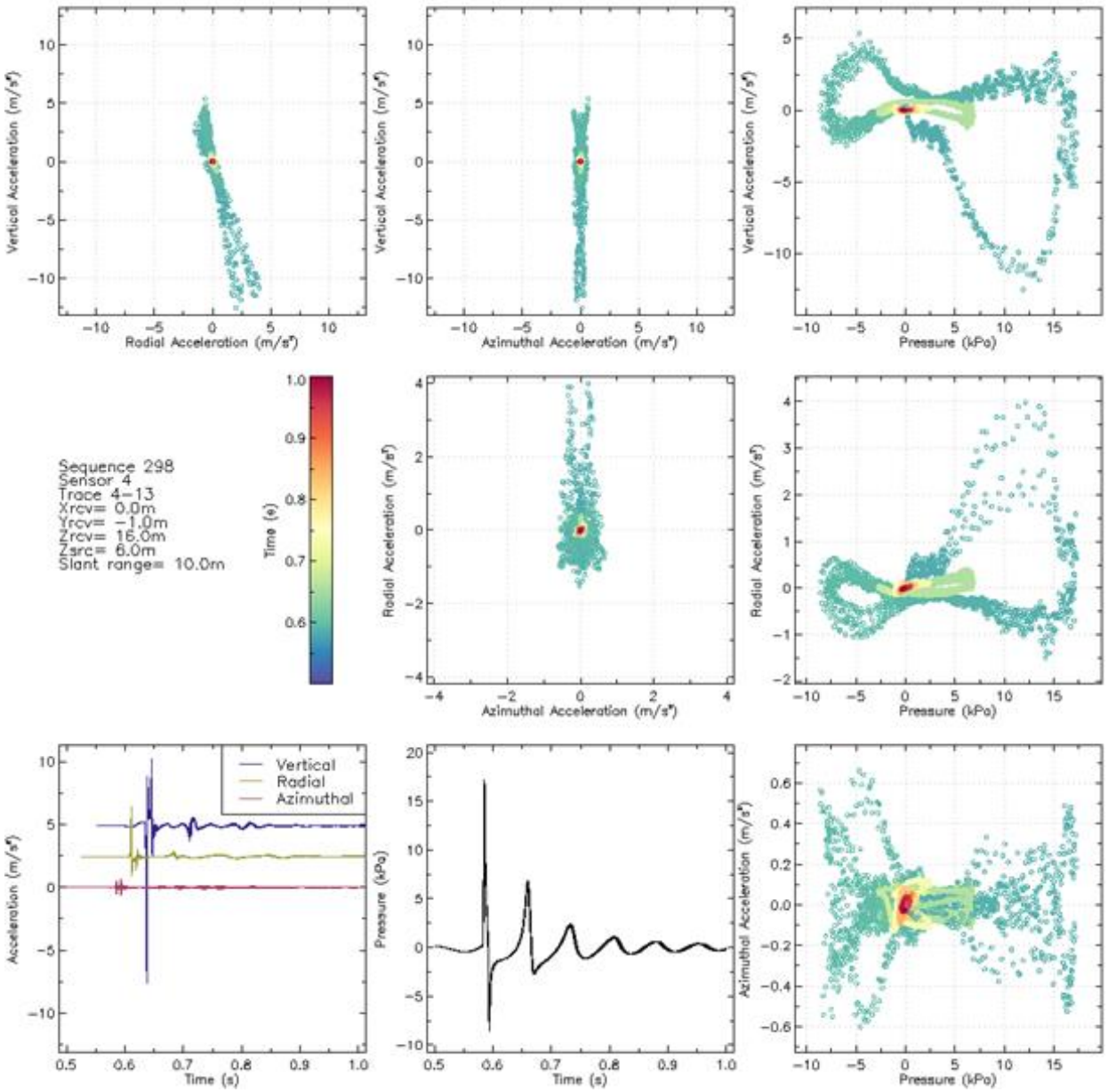

Figure 17. Receiver 10 m below airgun depth and 1 m range: Particle motion and pressure scatter plots for 60 in^3 airgun data. Acceleration traces (lower left panel) are offset vertically and horizontally for display purposes. Data were band-pass filtered between 10 and 1000 Hz (vertical acceleration data were band-pass filtered between 30 and 1000 Hz).

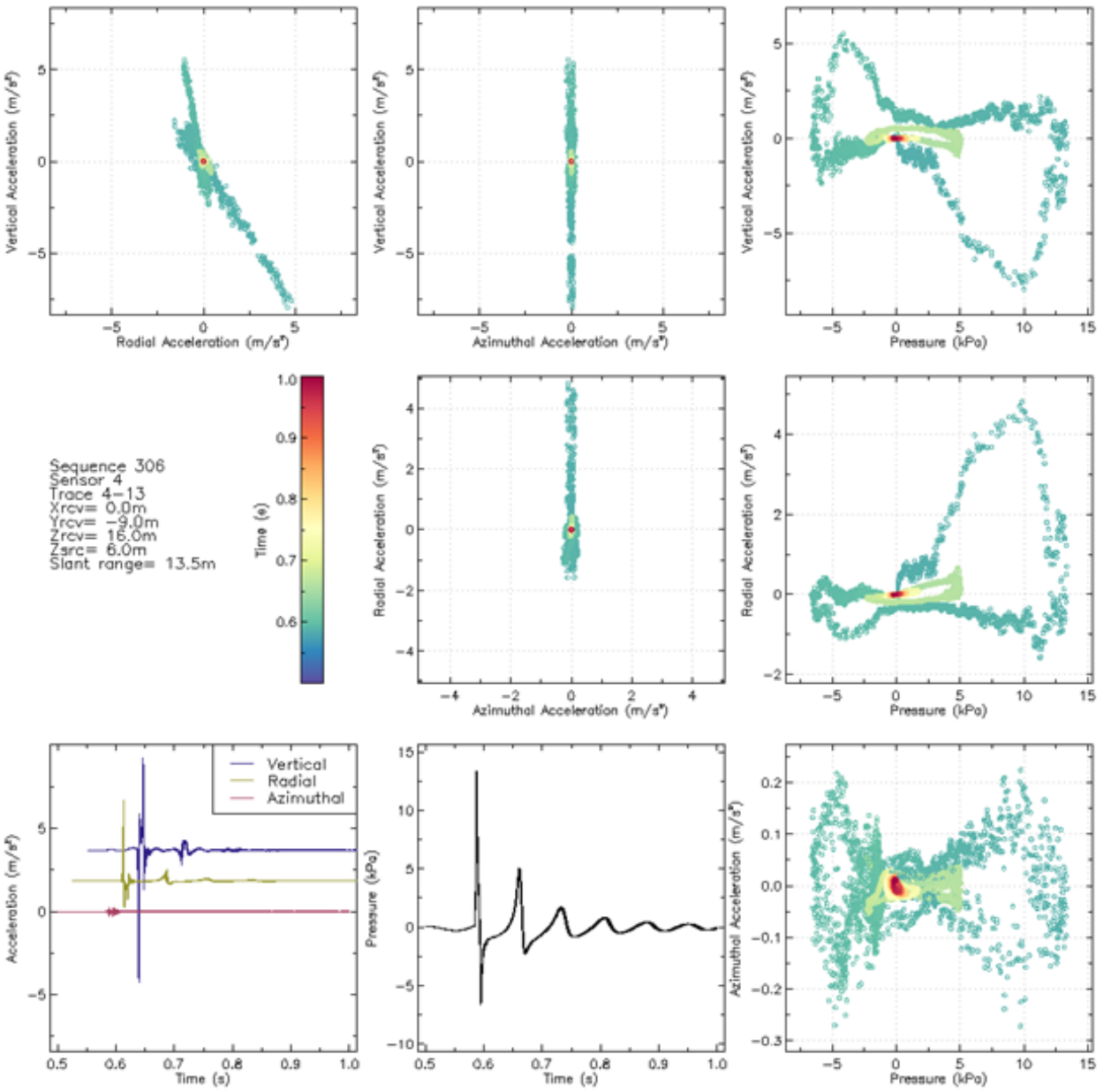

Figure 18. Receiver 10 m below airgun depth and 9 m range: Particle motion and pressure scatter plots for 60 in^3 airgun data. Acceleration traces (lower left panel) are offset vertically and horizontally for display purposes. Data were band-pass filtered between 10 and 1000 Hz (vertical acceleration data were band-pass filtered between 30 and 1000 Hz).

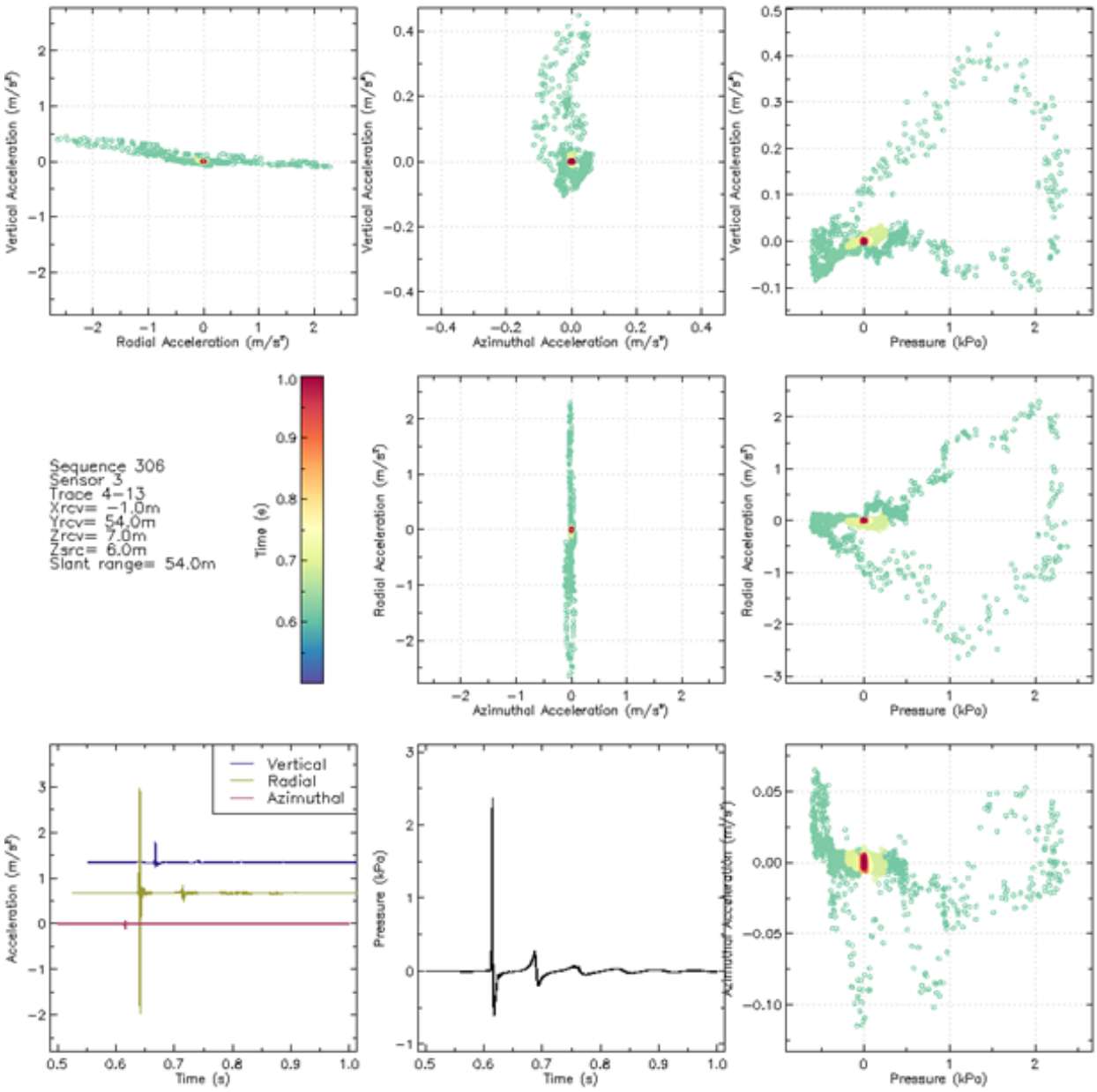

Figure 19. Receiver 1 m below airgun depth and 54 m range: Particle motion and pressure scatter plots for 60 in^3 airgun data. Acceleration traces (lower left panel) are offset vertically and horizontally for display purposes. Data were band-pass filtered between 10 and 1000 Hz (vertical acceleration data were band-pass filtered between 30 and 1000 Hz).

1.3.4. Acceleration versus Range

Figures 20, 21, and 22 show peak, broadband rms, and band-limited rms acceleration, respectively, versus slant range for all sequences of the 60 and 150 in^3 airgun measurements. These data are also presented in tables in Appendix B.

Particle acceleration was qualitatively similar for measurements of the 60 and 150 in^3 airguns; however, the rms acceleration for the 150 in^3 airgun was, on average, 26% larger than that of the 60 in^3 airgun (Figures 20 and 21). Low frequencies (below 100 Hz; Figure 22) dominated broadband acceleration at close range, but they did not propagate as well as frequencies above 100 Hz. At 54 m range, acceleration in the 10–300 and 300–1000 Hz bands were several times larger than acceleration in the 10–30 and 30–100 Hz bands. The change in the trend of 10–30 Hz levels at 1–10 versus 10–17 m range (Figure 22) is due to the deeper receiver depth for the longer-range data.

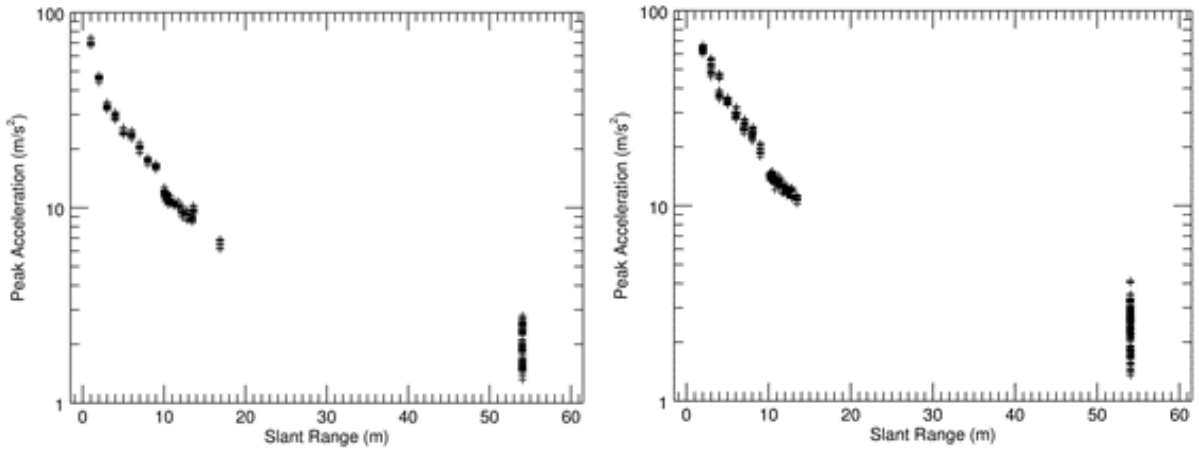

Figure 20. Peak acceleration as a function of slant range for the (left) 60 in^3 and (right) 150 in^3 airguns. Peak acceleration was calculated from unfiltered data.

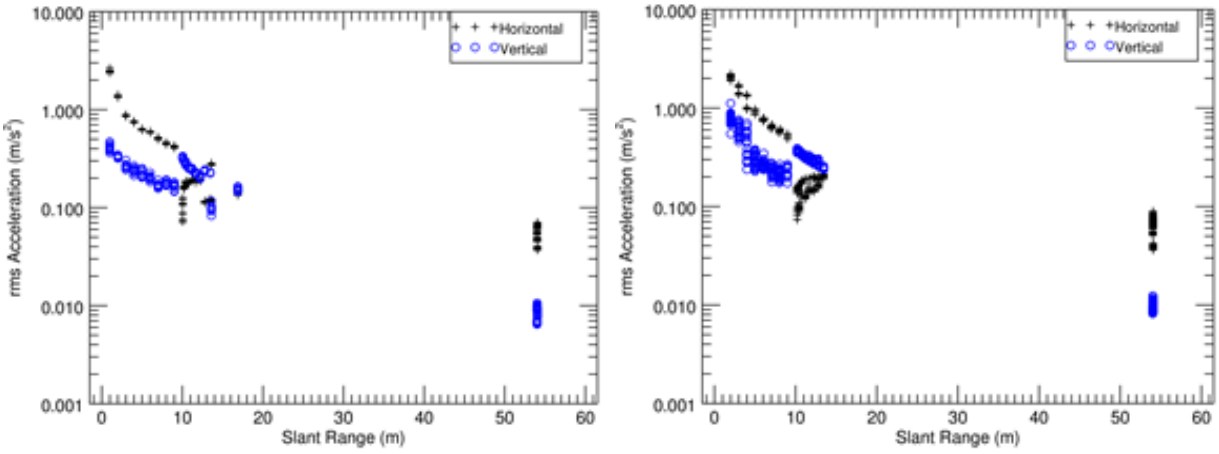

Figure 21. Broadband rms acceleration as a function of slant range for the (left) 60 in^3 and (right) 150 in^3 airguns. Horizontal data are filtered between 10 and 1000 Hz, Vertical data are filtered between 30 and 1000 Hz.

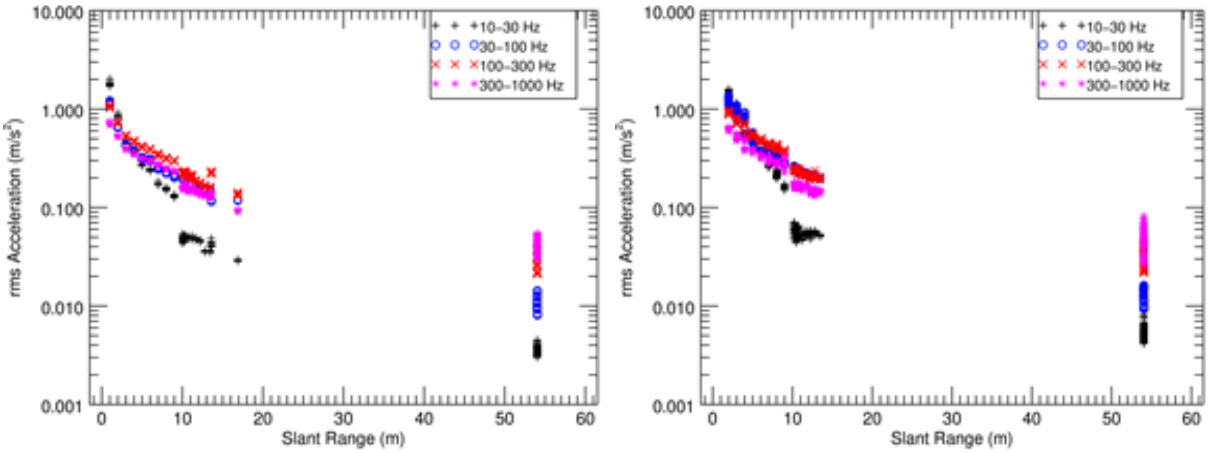

Figure 22. Band-limited rms acceleration as a function of slant range for the (left) 60 in^3 and (right) 150 in^3 airguns. Acceleration in the 10–30 Hz band includes the horizontal direction only.

1.3.5. Spectra

This section contains unfiltered acceleration spectra in the horizontal and vertical directions, as well as for the total acceleration magnitude. Acceleration spectra show that the 150 in^3 airgun has spectral peaks at lower frequencies than those of the 60 in^3 airgun spectra, which is due to the longer bubble pulse period from the larger airgun. The source-receiver geometry explains the relative differences between horizontal and vertical acceleration spectra (which is more clearly seen in Section 1.3.3). Low frequencies appear to attenuate more rapidly with range than high frequencies.

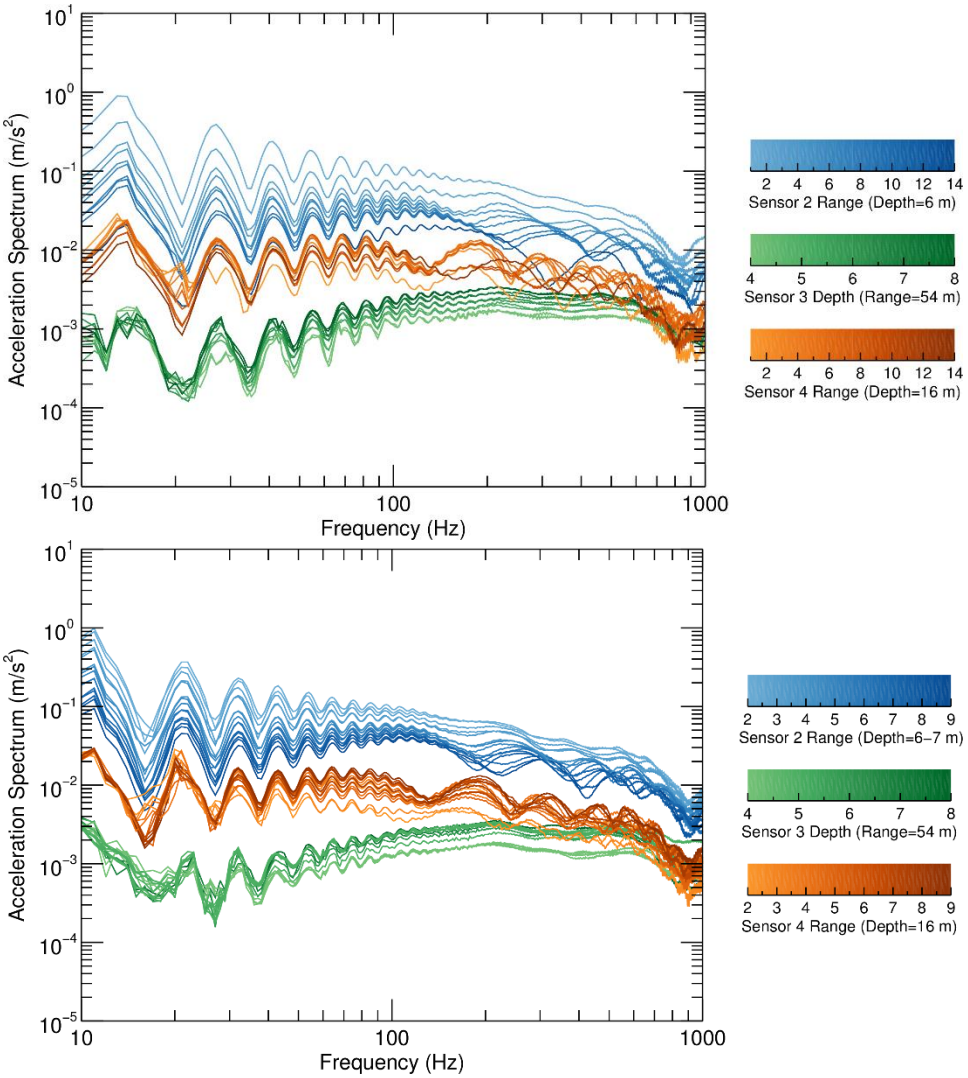

Figure 23. Horizontal acceleration spectra for the (top) 60 in^3 and (bottom) 150 in^3 airguns.

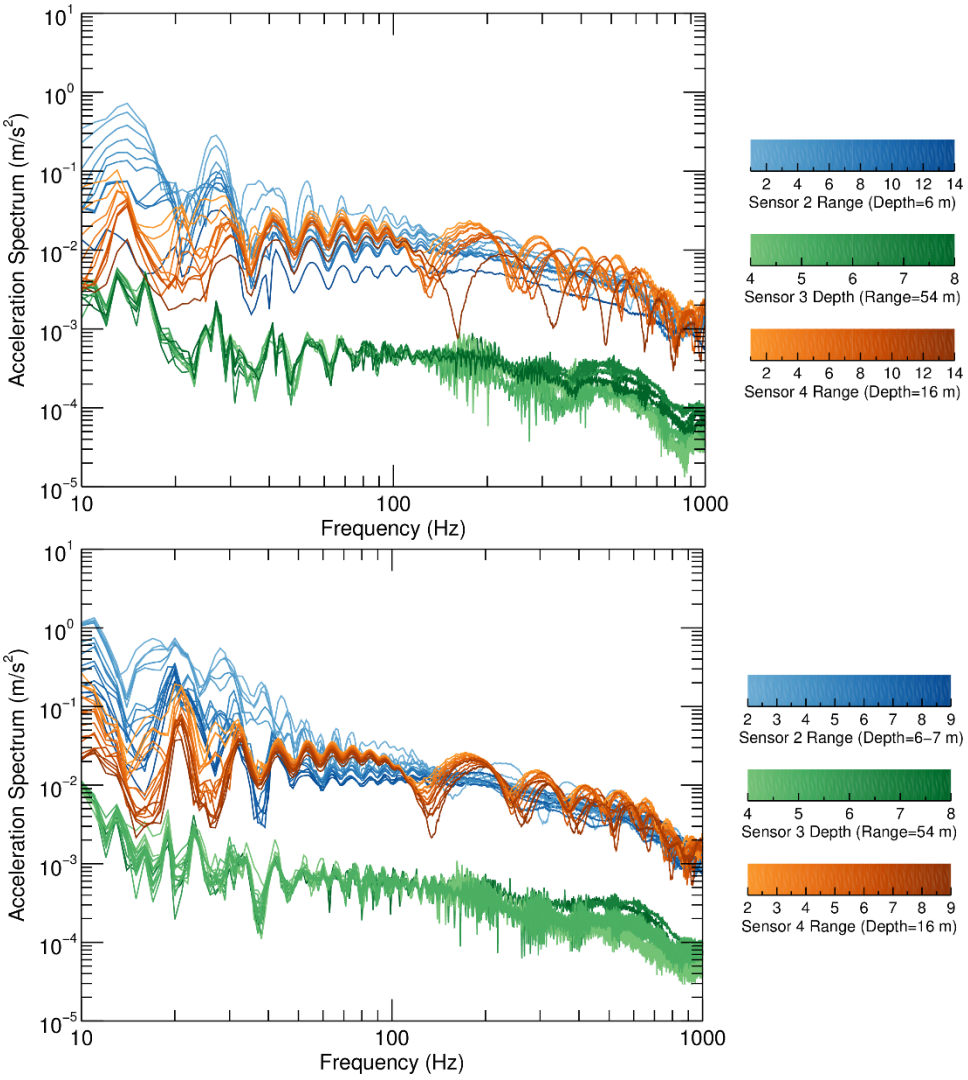

Figure 24. Vertical acceleration spectra for the (top) 60 in^3 and (bottom) 150 in^3 airguns.

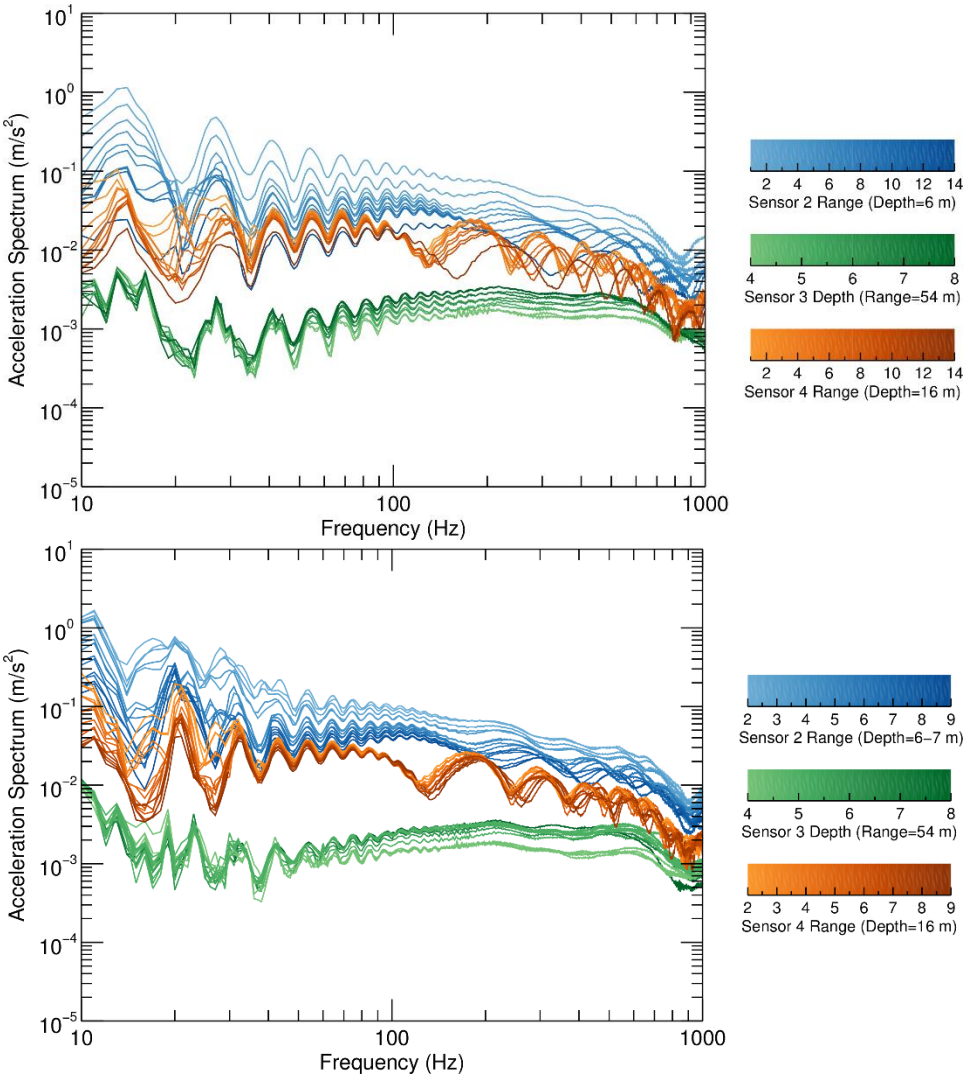

Figure 25. Total acceleration spectra for the (top) 60 in^3 and (bottom) 150 in^3 airguns.

1.4. Data Analysis Discussion

The M20 hydrophones were assumed to have a nominal standard pressure sensitivity of −220.8 dB re 1 V/µPa and flat frequency response below 1 kHz (see Section 1.2.2 and Appendix A). This sensitivity was provided by GTI, who extrapolated the sensitivity from a tank calibration of M20 sensor 3 at 1 kHz (GTI performed a tank calibration at frequencies between 1 and 5 kHz, but the trend of the sensitivity was not used in the extrapolation to lower frequencies). The calibrations of the M20 omnidirectional hydrophone channels were not verified in the field, to the best of our knowledge. This means that if there was an error in the assumed nominal sensitivity of the M20 hydrophones, the particle acceleration data will be biased since all particle motion data were calibrated relative to the pressure data from sensor 3 (see Section 1.2.3). The particle motion calibration (Figure 4) showed that there was a 1–2 dB variation in levels between 100 and 1000 Hz, which suggests the M20 directional sensor and/or hydrophone frequency response differs from the nominal values in Appendix A by a similar amount in that frequency range.

Peak sound pressures recorded (see Section 1.3.1) on the M20 sensors appear to be systematically lower than sound pressures recorded on the pistonphone-calibrated B&K hydrophones. Furthermore, the relative timing between the AGH (nearfield) signals and M20 signals, indicates there were errors in the logged source-receiver ranges for sensor 2 (i.e., the recorded range of this sensor was generally less than the actual range). Thus, we believe that the M20-based particle motion results are biased, and that accelerations recorded on these sensors are lower than the actual accelerations generated by the airguns by 5.0 dB. We calculated the 5.0 dB error in the M20 calibrations by taking the difference between the trend of the M20 pressure measurements and the trend of the B&K reference measurements, after correcting for the observed errors in the slant range to M20 sensor 2 (see Figure 9).

1.5. Data Analysis Summary

We analyzed pressure and accelerometer data collected by PGS in 2010 during the Svein Vaage airgun study to calculate acoustic particle motion at short ranges (<60 m) from single airguns. Our initial analysis of the M20 data indicated that acceleration measurements from these sensors were an order of magnitude greater than what would be physically expected, based on the corresponding pressure measurements. This disagreement indicated that there was likely an unknown digitization gain applied to the M20 data by PGS during data acquisition. Therefore, we applied a scaling factor to correct the calibration of the M20 particle acceleration channels, based on far-field comparisons with the M20 pressure channels, to account for the unknown digitization gain. We then used the corrected accelerometer data to calculate particle motion generated by the airguns in the horizontal (radial and azimuthal) and vertical directions at distances from 1–54 m from the source. Measurements on the horizontal channels covered the frequency range of 10–1000 Hz, but spurious low-frequency signals on the vertical channels limited their useful range to 30–1000 Hz.

To check the calibrations of the M20 hydrophone channels, we compared measurements from the M20 sensors to reference pressure data collected using calibrated B&K omnidirectional hydrophones. The peak pressure measurements were, on average, 5.0 dB lower on the M20 sensors when compared to the B&K reference hydrophones. This indicates there was likely an error in the pressure calibrations of the M20 sensors applied in the field by PGS. Possible biases in the calibrations of the M20 sensors will need to be accounted for when using these data in future. Measurements from this chapter are compared to predictions of an acoustic model that calculates near-field particle motion from airguns in Chapter 2. Measurements presented in Chapter 2 include corrections to account for the −5.0 dB error in the M20 calibrations, and errors in the logged ranges to M20 sensor 2.

Chapter 2. Model Validation

2.1. Introduction

Marine geophysical surveying, using seismic airguns, generates high levels of underwater sound pressure and particle motion, and thus has the potential to negatively affect marine organisms. In Canada, before seismic surveys are carried out near habitat areas of sensitive species, regulatory bodies (e.g., Fisheries and Oceans Canada) generally require pre-survey assessments of potential acoustic impacts before survey permits are granted. Such assessments generally depend on model-based estimates of airgun noise emissions to determine the spatial extent of potential impacts. Current state-of-the-art methods for modelling sound pressures from seismic airguns are well developed and have been extensively validated (MacGillivray 2006, Matthews and MacGillivray 2013, Racca et al. 2015). However, methods for modelling acoustic particle motion from seismic airguns are not as well developed; comparisons of particle motion predictions from several different models, presented at the recent International Airgun Modelling Workshop in Dublin, Ireland, showed that the different models gave very different predictions when modelling the same array (Ainslie et al. 2016). Thus, there is a need to ground-truth existing models of particle motion from seismic airguns against real field data.

Acoustic particle motion, the motion of an infinitesimal portion of the medium relative to the medium as a whole, may be more closely related to injury in fish and invertebrates (Popper et al. 2014). Unlike pressure, which is a scalar quantity with magnitude only, particle motion (displacement, velocity, and acceleration) is a vector quantity that includes both magnitude and direction. It is known that all fish are capable of directly sensing the particle motion component of sound (Fay 1984), while relatively few fish also sense the pressure component (Popper et al. 2003). Animals such as crustaceans with statocyst-based hearing are also thought to sense only particle motion (Mooney et al. 2012). Particle motion is used by fish and invertebrates for various biological functions, and noise exposure can cause behavioural response and even physiological damage at high levels (McCauley et al. 2000, Popper et al. 2007, Sarà et al. 2007, Mueller-Blenkle et al. 2010, Fewtrell and McCauley 2012, Halvorsen et al. 2012). Increasing concern over the effects of anthropogenic sounds on these marine species requires more complete descriptions of the sound fields these animals are exposed to. Modelling of predicting particle motion is therefore required for assessing impacts of anthropogenic noise on fish and invertebrates

In 2010, the Oil and Gas Producers Joint Industry Program (JIP) on Sound and Marine Life contracted PGS to conduct the Svein Vaage airgun study (Mattsson and Jenkerson 2008). The study involved measuring the pressure and particle motion from Sercel G-guns with volumes of 60, 150, 380, and 520 in^3 at a deep fjord in Norway. The particle motion measurements were recorded using M20 sensors (GeoSpectrum Technologies Inc.; GTI), which were composed of a single omnidirectional pressure sensor (hydrophone) and a 3-axis accelerometer. Pressure and particle motion measurements from the 60 and 150 in^3 airgun were analyzed in Chapter 1[1]. Pressure and particle motion data were presented at different ranges and depths, over the 10–1000 Hz frequency range.

The goal of this chapter is to validate modelled particle motion predictions from JASCO's Airgun Array Source Model (AASM). This validation was performed by comparing modelled pressure and particle acceleration data from AASM with calibrated airgun data from Chapter 1. This chapter presents the modelled pressure and particle acceleration data for the 60 and 150 in^3 airguns measured during the Svein Vaage study.

[1] The M20 particle motion measurements for the 380 in^3 and 520 in^3 airguns were found to have significant calibration issues, so data for these sources could not be used in the model validation. See Chapter 1 for details.

2.2. Model Validation Methods

2.2.1. Airgun Array Source Model (AASM)

Airgun source waveforms were predicted with JASCO's Airgun Array Source Model (AASM; MacGillivray 2006, MacGillivray in press). AASM is based on a physical model of the oscillation and radiation of airgun bubbles, as originally described by Ziolkowski (1970). The model solves a set of parallel differential equations, corresponding to the coupled equations of motion for an array of oscillating airgun bubbles. Physical effects accounted for in the simulation include pressure interactions between airguns, port throttling, bubble damping, and generator-injector (GI) gun behaviour discussed by Dragoset (1984), Laws et al. (1990), and Landro (1992).

The model includes five physical parameters, controlling effects such as turbulent damping of the bubble of airflow through the gun ports, that are constrained by fitting the model waveforms to experimental data. A global optimization algorithm tunes the parameters to a library of airgun source pressure signatures. Normally, the free parameters are tuned to a large library of high quality seismic source signature data obtained from the JIP on Sound and Marine Life (Mattsson and Jenkerson 2008). This allows AASM to model a large variety of airgun types and volumes. To better match the measurements for this study, we tuned AASM specifically to the G-Gun 60 and 150 in^3 airgun pressure signatures from sequences analyzed in Chapter 1. These signatures included those recorded using the B&K 8015 corner and centre array hydrophones. Pressure data from the M20 sensors were not used for tuning AASM, so as not to influence the model validation comparisons presented in this chapter. Likewise, particle acceleration data were not used in the tuning of AASM, since the purpose of this investigation was to validate particle motion predictions of the model.

AASM calculates the source waveform (i.e., notional pressure signature) for an airgun based on its volume, depth, and firing pressure, and includes interaction effects from the surface reflection. The source waveform is the product of the far-field sound pressure signature generated by the airgun and the source-receiver distance (this is equal to the sound pressure that would exist at a distance of 1 m from a hypothetical point monopole source; ISO 2017).

In addition to pressure, AASM also predicts the particle velocity potential, which can be used to compute the particle velocity by taking the gradient of the potential:

$$\vec{v} = \nabla\phi(r,t)\ , \tag{2}$$

where Φ is the velocity potential, r is range, t is time, and $\vec{v}$ is the particle velocity vector. Since the particle motion measurements were made in a deep fjord, the received signals do not contain seabed-reflected components and can be modelled with a computationally-efficient image-source model that accounts for the only two significant paths: the direct and surface-reflected paths. Particle velocity is then converted to acceleration by time differentiation so it can be compared to acceleration measurements.

2.2.2. VSTACK Sound Propagation Model

To verify the particle acceleration predictions from the image-source model, we modified JASCO's VSTACK sound propagation model to predict three-dimensional (3-D) particle motion and compared the VSTACK predictions to the image-source predictions. VSTACK uses the wavenumber integration approach to solve the exact acoustic wave equation for arbitrarily layered range-independent acoustic environments. Sound propagation is computed by decomposing the outgoing pressure field into a continuum of outward-propagating plane cylindrical waves. VSTACK solves the wave equation in the frequency domain and uses Fourier synthesis to compute synthetic pressure waveforms versus depth and range by convolving the source waveforms with the impulse response of the waveguide.

In a fluid medium, particle velocity is related to pressure by Euler's equation (Jensen et al. 1994):

$$\vec{v} = \frac{-1}{\rho} \int \nabla p dt, \tag{3}$$

where ρ is water density, p is pressure, t is time, and $\vec{v}$ is particle velocity. Since the wavenumber integration kernel is a product of analytic expressions in terms of range and depth, VSTACK computes particle velocity by taking the spatial gradient of the pressure field analytically and integrating over time in the frequency domain by multiplying by $(i2\pi f)^{-1}$, where f is frequency. VSTACK results are valid over the full angular range of the wave equation, so it is suitable for near- and far-field modelling. The model produces time-domain waveforms of pressure or 3-D particle velocity that can be post-processed to yield estimates of pressure or velocity metrics. VSTACK particle velocity results were converted to acceleration by time differentiation for comparison with the image-source model. Modelled particle acceleration agreed with the two models for a homogeneous water halfspace environment, which was suitable for comparing to the Svein Vaage measurements.

Modelled particle acceleration was compared to the Svein Vaage measurements analyzed in Chapter 1. Modelled data were filtered in the same way as for measured data (i.e., between 10 and 1000 Hz and into narrower frequency bands) and processed for the peak and rms acceleration over different directions (e.g., horizontal, vertical, and total).

2.2.3. Corrections Applied to M20 Data

Chapter 1 showed that the peak pressure measurements on the M20 sensors were, on average, 5.0 dB lower than on the B&K reference hydrophones. The M20 acceleration channels were, therefore, also biased 5.0 dB too low, since they were calibrated relative to the M20 pressure sensitivity. In this chapter, we have increased the pressure and particle acceleration measurements from all M20 sensors by 5.0 dB to account for this systematic calibration error.

Furthermore, analysis of pulse arrival times between those recorded on nearfield-hydrophones (at 1.5 m range) and M20 #2 showed there were errors in the logged positions of this sensor. Analysis of the pulse arrival times showed that the slant range for M20 #2 was too low by as much as 2.4 m. We have corrected for the position errors of M20 #2 in this chapter by assuming the errors in slant range are due to errors in the horizontal range (i.e., we assume the logged receiver depth was correct). Table 3 lists the sequence numbers with the corresponding airgun volume and corrected M20 coordinates. The coordinate correction only applied to M20 #2; coordinates for M20s #3 and #4 were assumed to be identical to those recorded in the experimental logs and presented in Chapter 1.

Table 3. Sequence numbers, airgun volumes, and corrected M20 coordinates. X and Y are horizontal coordinates (i.e., in the plane parallel to the water surface) and Z is the vertical coordinate (i.e., distance from the water surface). X = 0 and Y = 0 correspond to the airgun's x and y location, and Z = 0 corresponds to the water surface.

Sequence	Airgun volume (in³)	Sensor #2 (m)			Sensor #3 (m)			Sensor #4 (m)		
		X	Y	Z	X	Y	Z	X	Y	Z
282	150	0	−3.59	6	−1	54	8	0	−2	16
283	150	0	−4.12	6	−1	54	7	0	−3	16
284	150	0	−4.64	6	−1	54	6	0	−4	16
285	150	0	−5.69	6	−1	54	5	0	−5	16
286	150	0	−6.66	6	−1	54	4	0	−6	16
287	150	0	−7.65	6	−1	54	4	0	−7	16
288	150	0	−8.31	6	−1	54	4	0	−8	16
289	150	0	−9.34	6	−1	54	4	0	−9	16
290	150	−3.74	0	6	−1	54	5	−2	0	16
291	150	−4.51	0	6	−1	54	5	−3	0	16
292	150	−5.57	0	6	−1	54	5	−4	0	16
293	150	−6.10	0	6	−1	54	5	−5	0	16
294	150	−6.57	0	7	−1	54	5	−6	0	16
295	150	−7.37	0	7	−1	54	5	−7	0	16
296	150	−7.97	0	7	−1	54	5	−8	0	16
298	60	0	−3.37	6	−1	54	8	0	−1	16
299	60	0	−3.43	6	−1	54	7	0	−2	16
300	60	0	−5.19	6	−1	54	6	0	−3	16
301	60	0	−5.70	6	−1	54	5	0	−4	16
302	60	0	−6.62	6	−1	54	4	0	−5	16
303	60	0	−6.88	6	−1	54	4	0	−6	16
304	60	0	−7.93	6	−1	54	5	0	−7	16
305	60	0	−8.69	6	−1	54	6	0	−8	16
306	60	0	−9.33	6	−1	54	7	0	−9	16
307	60	−8	−12.14	6	−1	54	8	−8	−11	16

2.3. Model Validation Results

Sections 2.3.1 and 2.3.2 present comparisons of modelled and measured sound pressure data from the omnidirectional hydrophone channel of the M20 sensors, and two B&K hydrophones. Comparisons are made in terms of peak and band-limited rms sound pressure versus range (Section 2.3.1), and for pressure waveforms and power spectral density (PSD) (Section 2.3.2).

Section 2.3.3 presents comparisons of measured and modelled particle acceleration versus range. Appendix C contains tables of the data. Section 2.3.4 presents comparisons of measured and modelled acceleration waveforms and spectra.

2.3.1. Peak and rms Pressure Versus Range

Figures 26–31 show comparisons of measured and modelled sound pressures (peak and rms) versus slant range from the two different volumes of airguns. Below 300 Hz, the modelled sound pressures show excellent agreement with the hydrophone measurements at all ranges. Above 300 Hz, the model slightly overestimates the measurements but still accurately reproduces the trend of the data. The agreement with the B&K hydrophone measurements (red symbols) is to be expected, since these were used for tuning the physical bubble parameters in AASM. The M20 pressure measurements were not used for tuning the model, so the agreement with these data indicates that the model is able to accurately predict the decay of sound pressures with distance from the source.

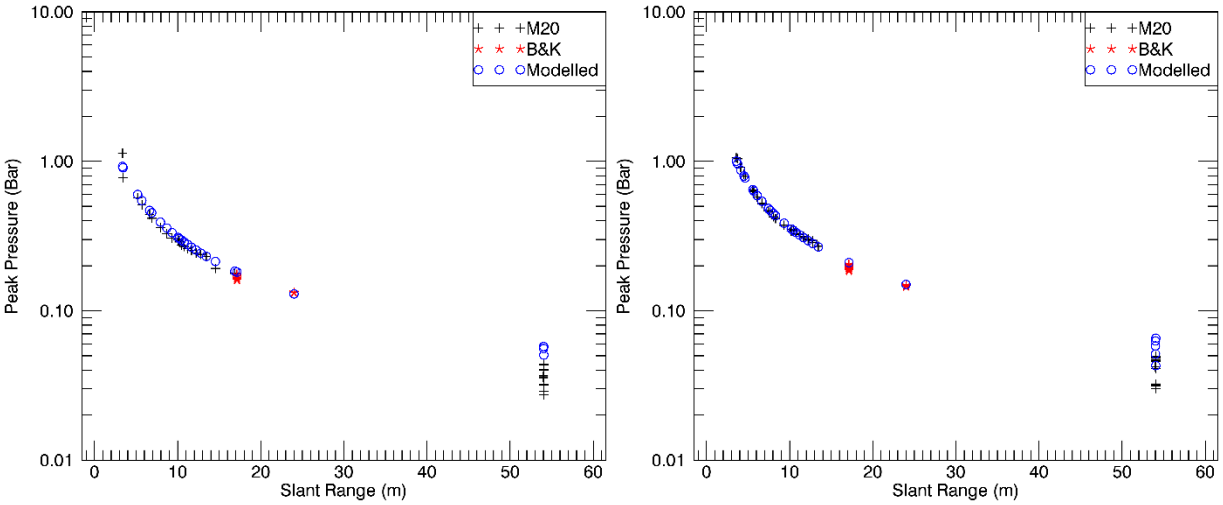

Figure 26. Peak pressure versus slant range for the (left) 60 in^3 and (right) 150 in^3 airguns. Peak pressures were calculated from unfiltered measured and modelled pressure waveforms.

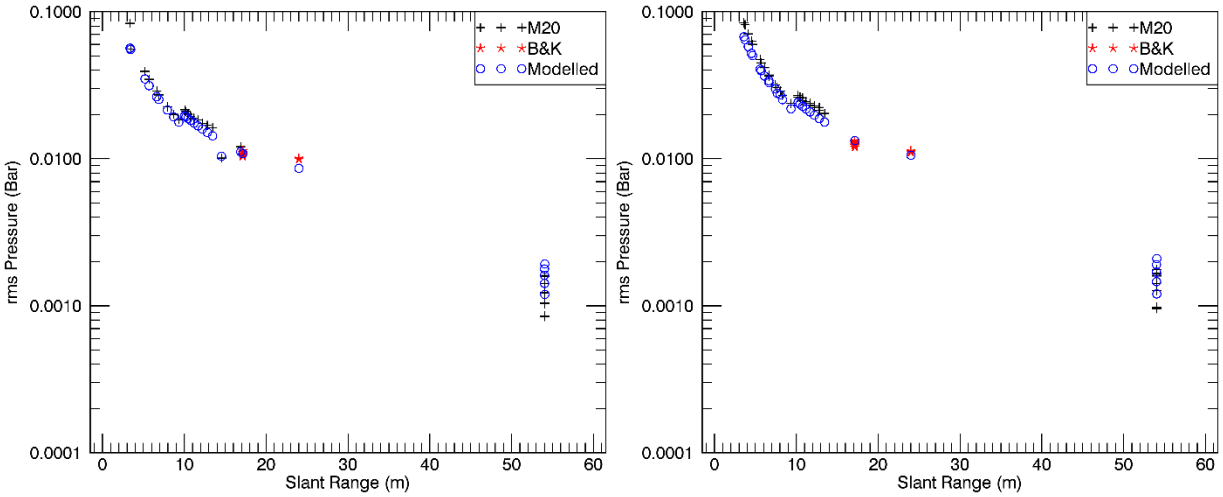

Figure 27. Broadband rms pressure versus slant range for the (left) 60 in^3 and (right) 150 in^3 airguns. Pressure waveforms were filtered between 10 and 1000 Hz.

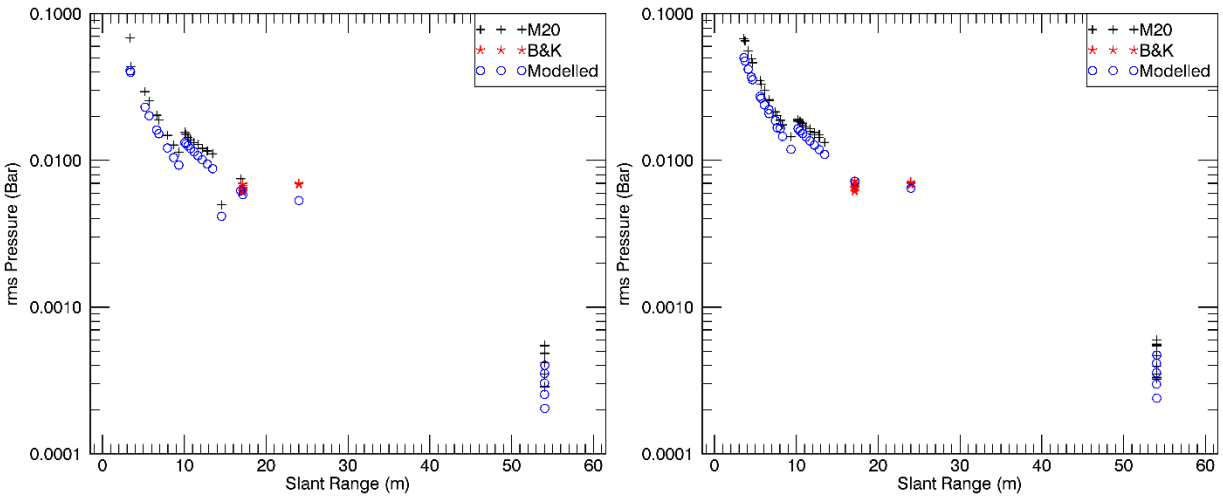

Figure 28. Band-limited (10–30 Hz) rms pressure versus slant range for the (left) 60 in^3 and (right) 150 in^3 airguns.

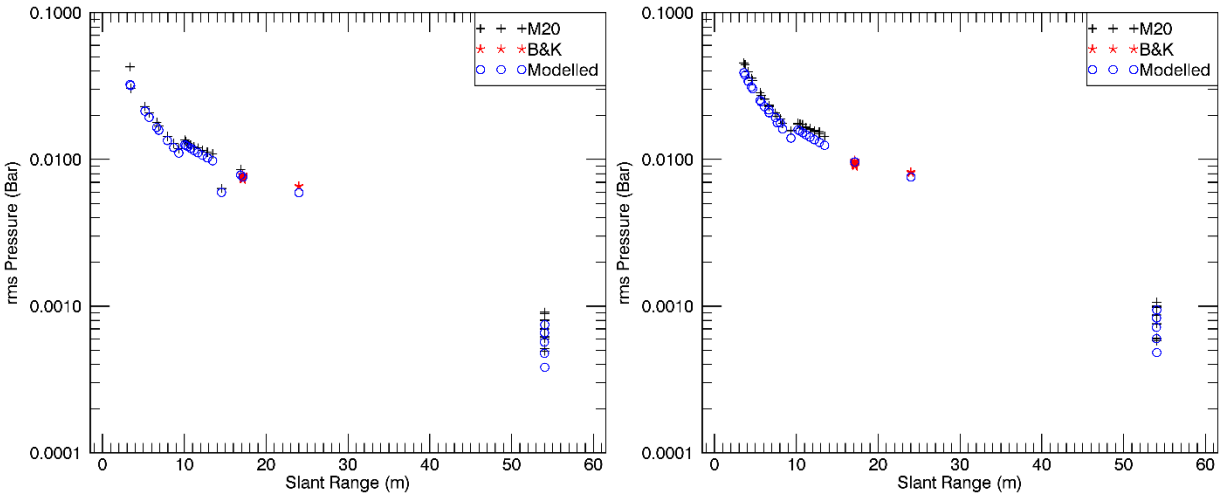

Figure 29. Band-limited (30–100 Hz) rms pressure versus slant range for the (left) 60 in^3 and (right) 150 in^3 airguns.

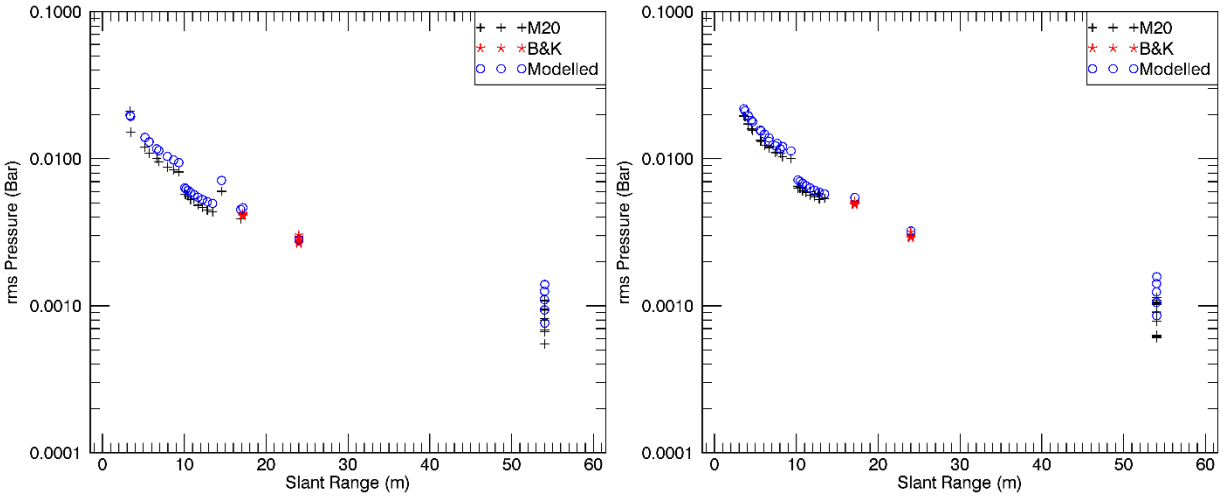

Figure 30. Band-limited (100–300 Hz) rms pressure versus slant range for the (left) 60 in^3 and (right) 150 in^3 airguns.

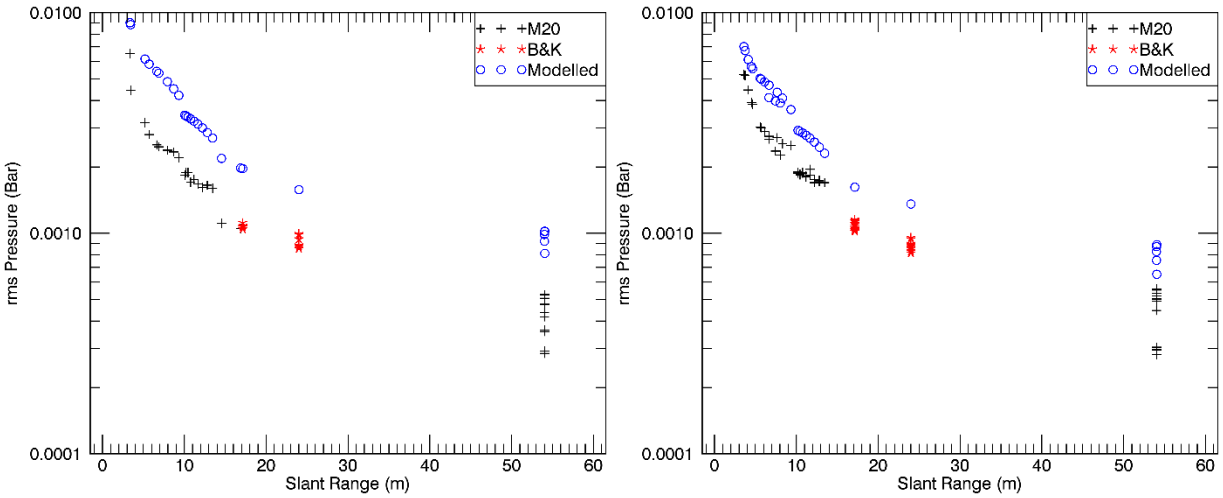

Figure 31. Band-limited (300–1000 Hz) rms pressure versus slant range for the (left) 60 in^3 and (right) 150 in^3 airguns.

2.3.2. Pressure Waveforms and Spectra

Figures 32–38 show comparisons of measured and modelled pressure waveforms at selected distances from the two different volumes of airguns. These plots show that the model is able to accurately reproduce both the time-dependent pressure waveforms and the frequency-dependent power spectra of the airguns. As shown in the previous section, while the agreement between model and measurements is very good at low frequencies, the model appears to slightly overestimate measured sound pressures at higher frequencies.

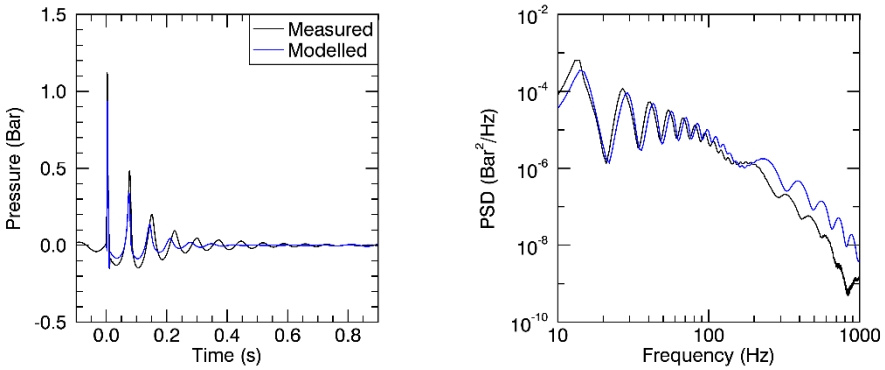

Figure 32. Modelled and measured pressure (left) waveforms and (right) power spectral density for a 60 in^3 airgun at 6 m depth and a receiver at 6 m depth and 3.4 m horizontal range (corresponding to sequence 298). Measured data are from M20 #2. Waveforms are band-pass filtered between 10 and 1000 Hz.

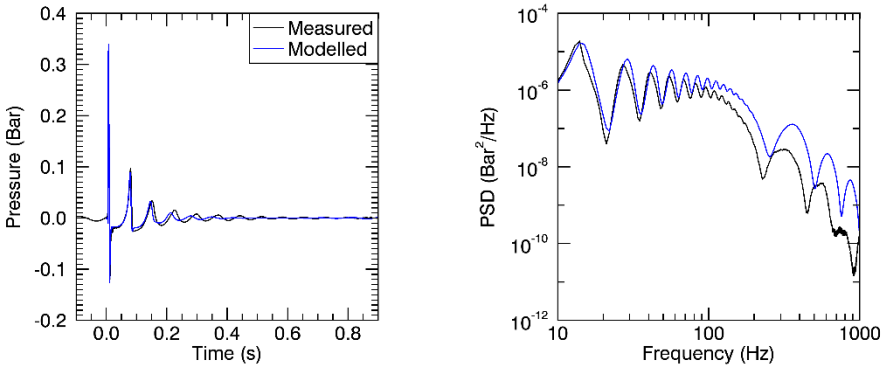

Figure 33. Modelled and measured pressure (left) waveforms and (right) power spectral density for a 60 in^3 airgun at 6 m depth and a receiver at 6 m depth and 9.3 m horizontal range (corresponding to sequence 306). Measured data are from M20 #2. Waveforms are band-pass filtered between 10 and 1000 Hz.

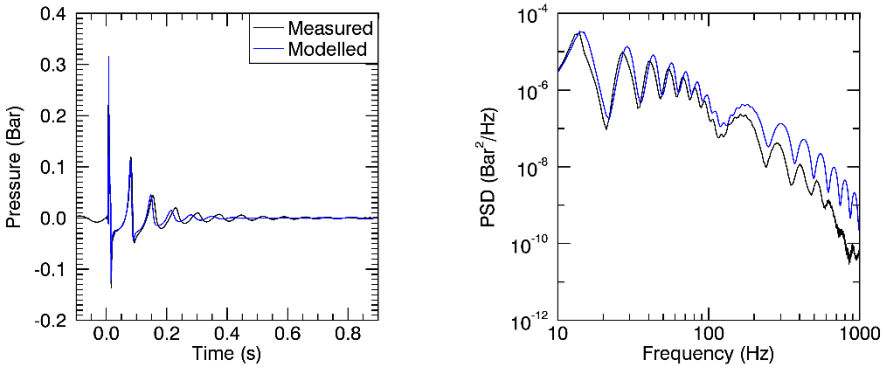

Figure 34. Modelled and measured pressure (left) waveforms and (right) power spectral density for a 60 in^3 airgun at 6 m depth and a receiver at 16 m depth and 1 m horizontal range (corresponding to sequence 298). Measured data are from M20 #4. Waveforms are band-pass filtered between 10 and 1000 Hz.

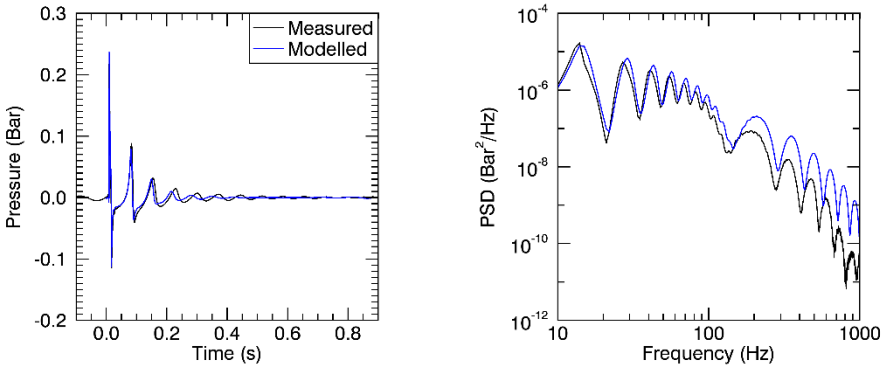

Figure 35. Modelled and measured pressure (left) waveforms and (right) power spectral density for a 60 in^3 airgun at 6 m depth and a receiver at 16 m depth and 9 m horizontal range (corresponding to sequence 306). Measured data are from M20 #4. Waveforms are band-pass filtered between 10 and 1000 Hz.

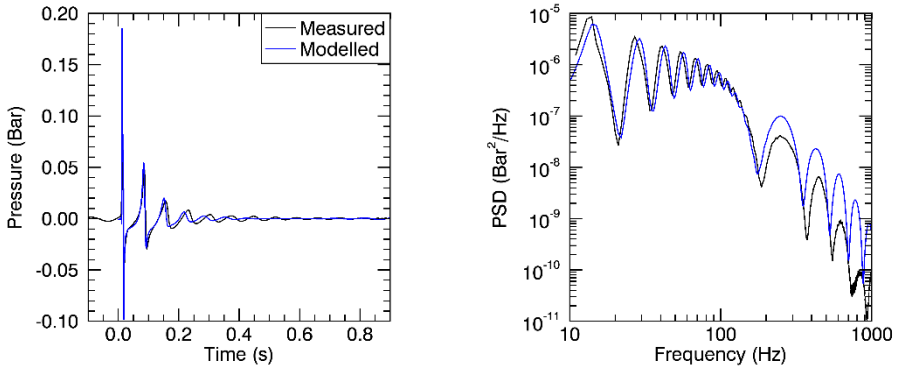

Figure 36. Modelled and measured pressure (left) waveforms and (right) power spectral density for a 60 in^3 airgun at 6 m depth and a receiver at 15 m depth and 14.6 m horizontal range (corresponding to sequence 298). Measured data are from a B&K hydrophone. Waveforms are band-pass filtered between 10 and 1000 Hz.

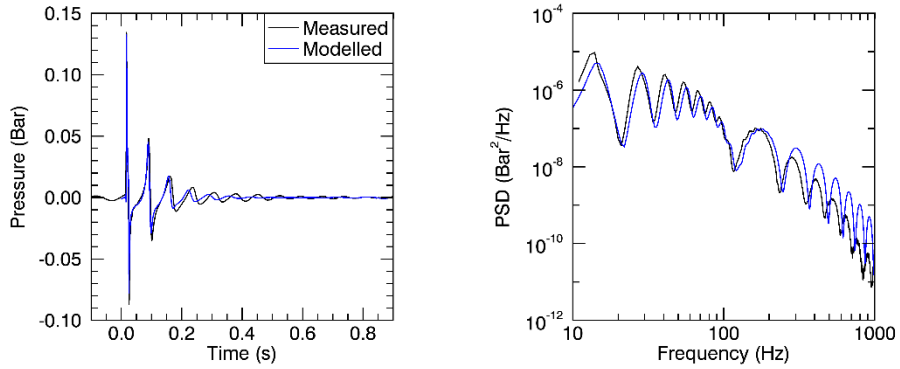

Figure 37. Modelled and measured pressure (left) waveforms and (right) power spectral density for a 60 in^3 airgun at 6 m depth and a receiver at 30 m depth and 0 m horizontal range (corresponding to sequence 298). Measured data are from a B&K hydrophone. Waveforms are band-pass filtered between 10 and 1000 Hz.

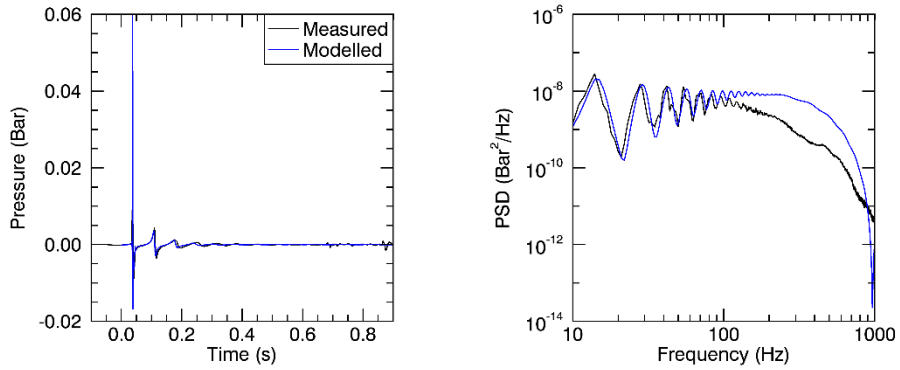

Figure 38. Modelled and measured pressure (left) waveforms and (right) power spectral density for a 60 in^3 airgun at 6 m depth and a receiver at 7 m depth and 54 m horizontal range (corresponding to sequence 306). Measured data are from M20 #3. Waveforms are band-pass filtered between 10 and 1000 Hz.

2.3.3. Acceleration Versus Range

Figures 39–45 show comparisons of measured and modelled particle acceleration (peak and rms) versus range from the two different volumes of airguns. In general, modelled particle acceleration was in good agreement with the measurements. Modelled peak and rms acceleration magnitude both followed the same range trend as the measurements, although the acceleration was slightly overestimated at larger ranges for the smaller 60 in^3 airgun. In general, the horizontal component of the acceleration was more accurately predicted than the vertical acceleration. This is likely because measurements on the vertical channels of the M20 sensors were affected by the vertical tension in the cable that was used to suspend these sensors from the sea surface (see Section 2.4).

The band level comparisons showed that the model was in good agreement with measurements between 10 and 300 Hz, although the model overestimated the particle motion below 30 Hz at 54 m range. As with the pressure measurements, the model overestimated the particle acceleration above 300 Hz but otherwise followed the trend of the data.

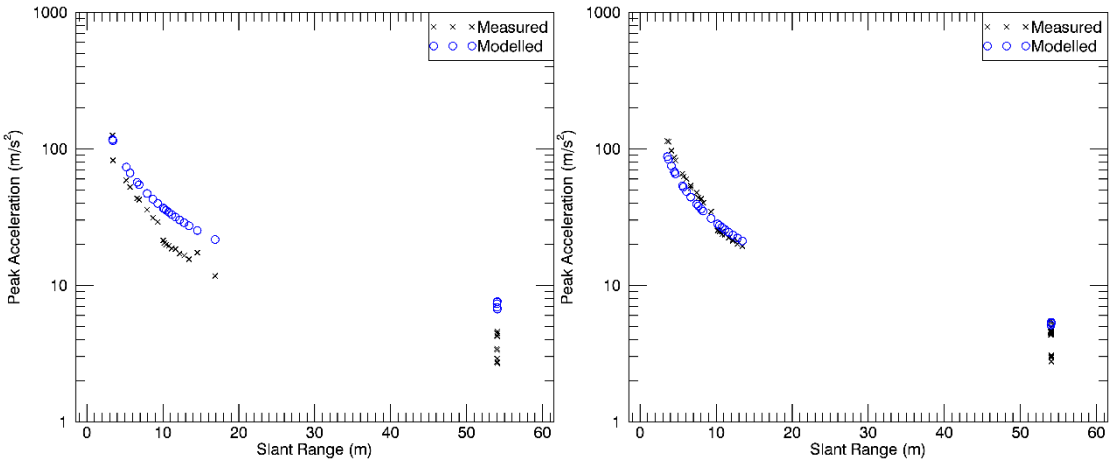

Figure 39. Peak acceleration magnitude versus slant range for the (left) 60 in^3 and (right) 150 in^3 airguns. Peak acceleration was calculated from unfiltered measured and modelled data.

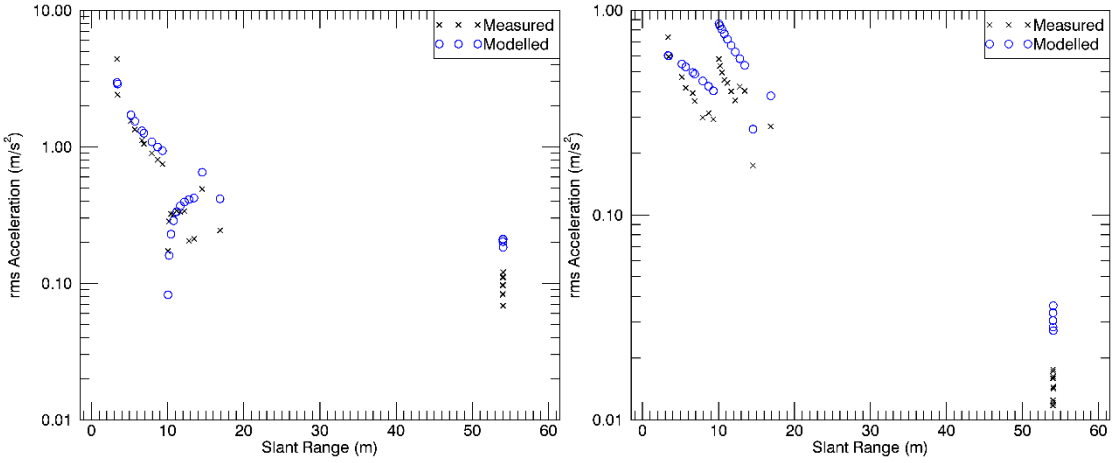

Figure 40. Broadband rms acceleration versus slant range for the 60 in^3 airgun in the (left) horizontal and (right) vertical directions. Horizontal data are filtered between 10 and 1000 Hz; vertical data are filtered between 30 and 1000 Hz.

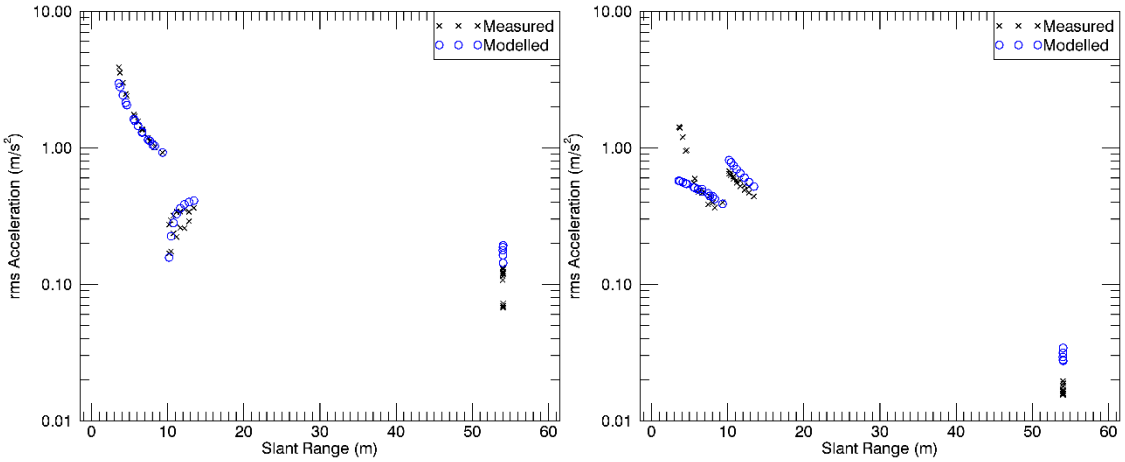

Figure 41. Broadband rms acceleration versus slant range for the 150 in^3 airgun in the (left) horizontal and (right) vertical directions. Horizontal data are filtered between 10 and 1000 Hz; vertical data are filtered between 30 and 1000 Hz.

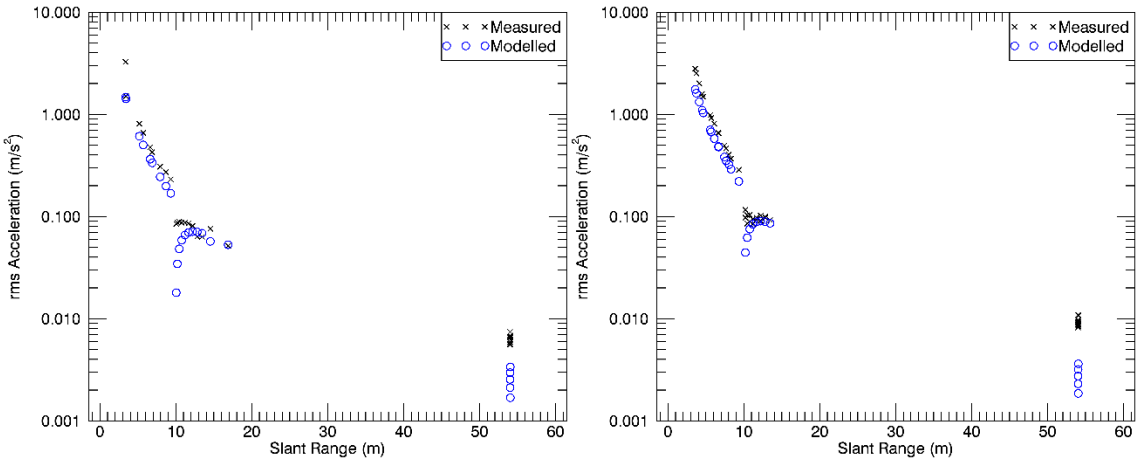

Figure 42. Band-limited (10–30 Hz) rms acceleration in the horizontal direction versus slant range for the (left) 60 in^3 and (right) 150 in^3 airguns.

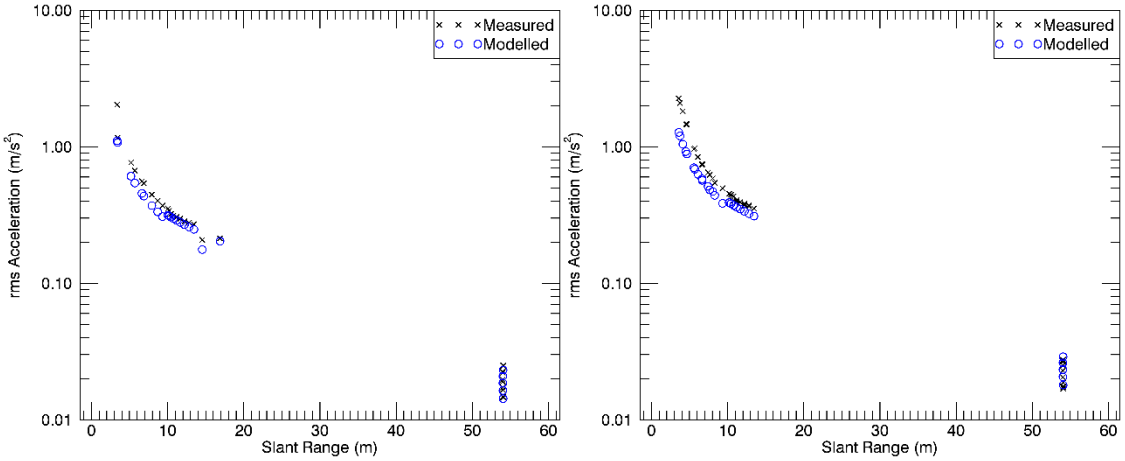

Figure 43. Band-limited (30–100 Hz) rms acceleration magnitude versus slant range for the (left) 60 in^3 and (right) 150 in^3 airguns.

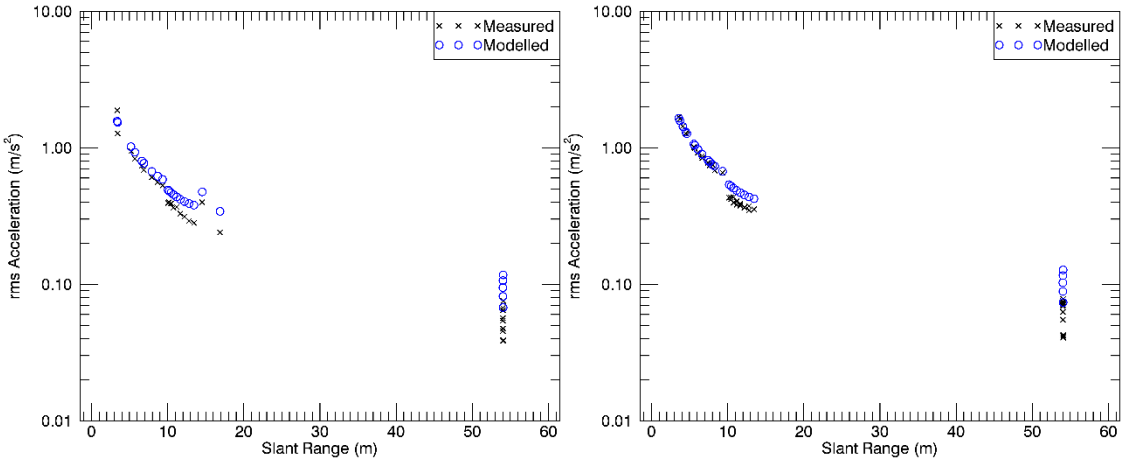

Figure 44. Band-limited (100–300 Hz) rms acceleration magnitude versus slant range for the (left) 60 in^3 and (right) 150 in^3 airguns.

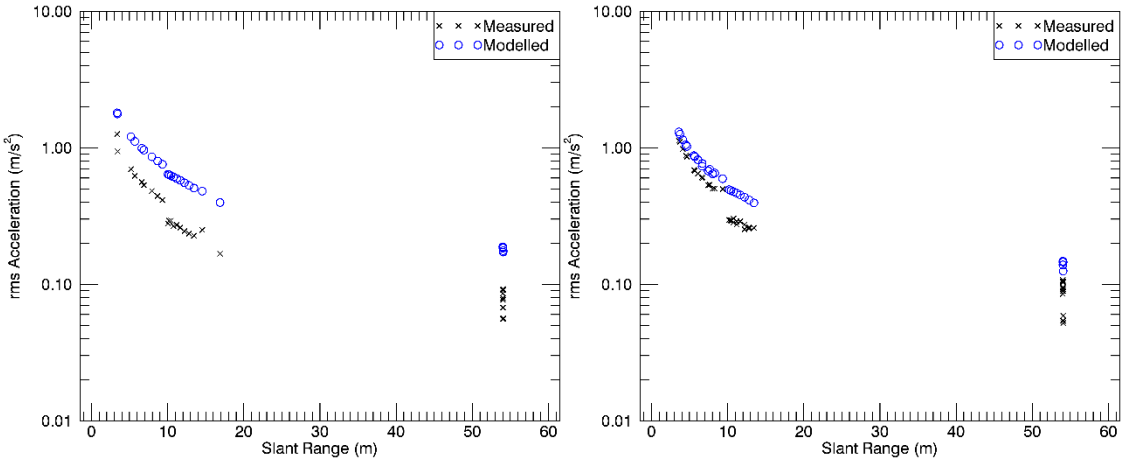

Figure 45. Band-limited (300–1000 Hz) rms acceleration magnitude versus slant range for the (left) 60 in^3 and (right) 150 in^3 airguns.

2.3.4. Acceleration Waveforms and Spectra

Figures 46–53 show comparisons of measured and modelled acceleration waveforms at selected distances from the two different volumes of airguns. Note that the vertical particle motion measurements have been high-pass filtered above 30 Hz to remove non-acoustic oscillations that are believed to originate from vibrations in the cables that were used to suspend the M20 sensors from the sea-surface (see Discussion). These plots show that the model accurately reproduced the horizontal particle acceleration waveforms and spectra at low frequencies (≤300 Hz), on all sensors. The model also accurately reproduced the vertical particle acceleration waveforms and spectra, except in some instances where cable vibrations were believed to have contaminated the data (e.g., Figures 46 and 49). Above 300 Hz, the model appeared to slightly overestimate the particle acceleration, particularly on M20 #3. It is unknown if the higher mismatch on M20 #3 was related to the placement of this sensor (at 54 m range, the longest measurement distance), or due to a difference in its calibration.

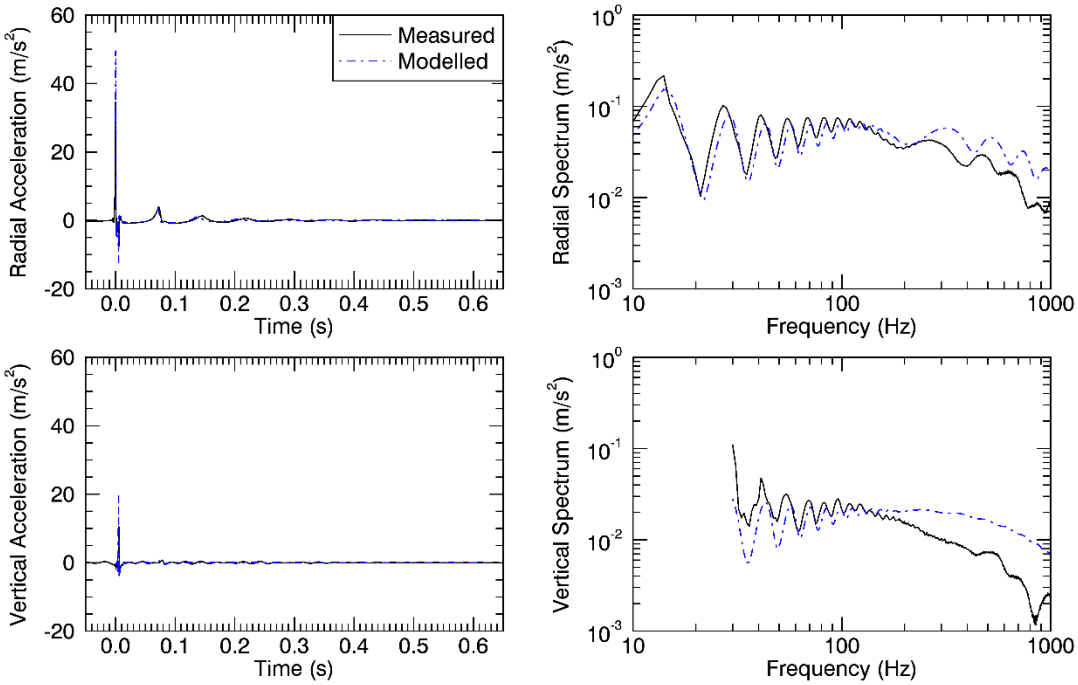

Figure 46. Modelled and measured acceleration (left) waveforms and (right) power spectra for a 60 in^3 airgun at 6 m depth and a receiver at 6 m depth and 6.9 m horizontal range (corresponding to sequence 303). Top and bottom panels are for the radial and vertical directions, respectively. Band-pass filters of 10–1000 Hz and 30–1000 Hz were used for the radial and vertical waveforms, respectively. Measured data are from M20 #2.

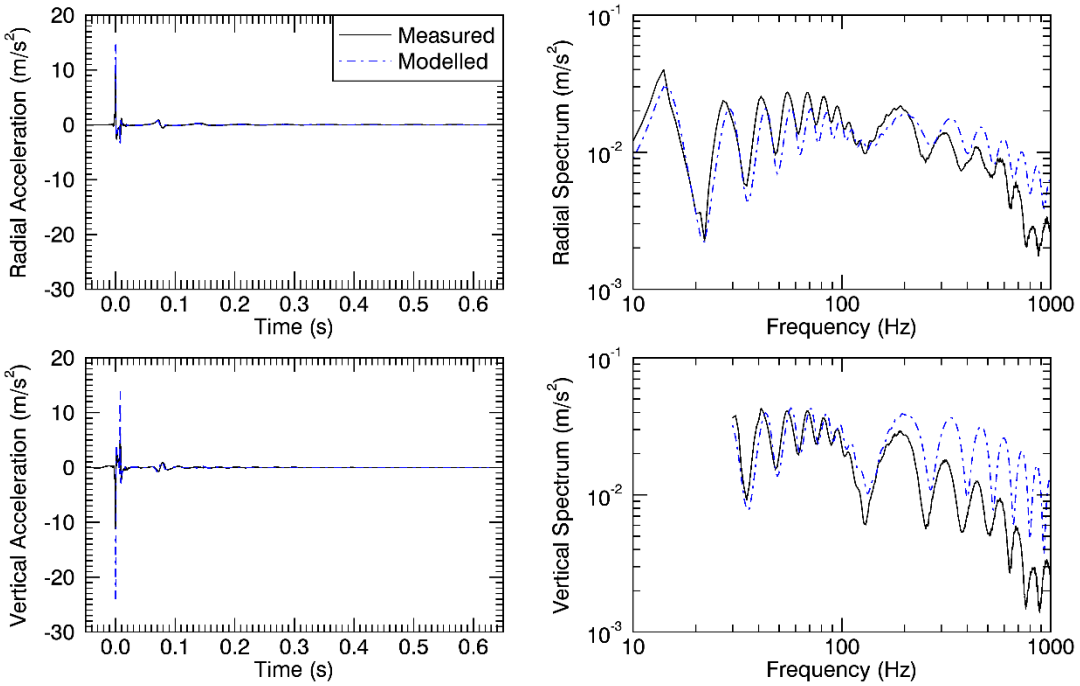

Figure 47. Modelled and measured acceleration (left) waveforms and (right) power spectra for a 60 in^3 airgun at 6 m depth and a receiver at 16 m depth and 6.0 m horizontal range (corresponding to sequence 303). Top and bottom panels are for the radial and vertical directions, respectively. Band-pass filters of 10–1000 Hz and 30–1000 Hz were used for the radial and vertical waveforms, respectively. Measured data are from M20 #4.

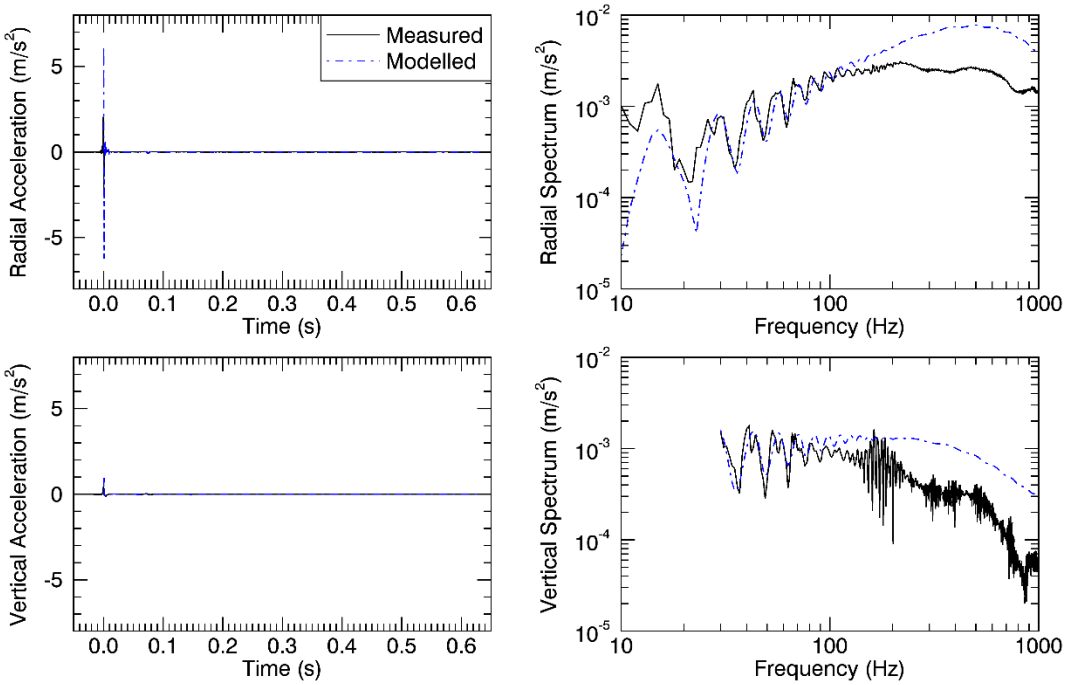

Figure 48. Modelled and measured acceleration (left) waveforms and (right) power spectra for a 60 in^3 airgun at 6 m depth and a receiver at 4 m depth and 54 m horizontal range (corresponding to sequence 303). Top and bottom panels are for the radial and vertical directions, respectively. Band-pass filters of 10–1000 Hz and 30–1000 Hz were used for the radial and vertical waveforms, respectively. Measured data are from M20 #3.

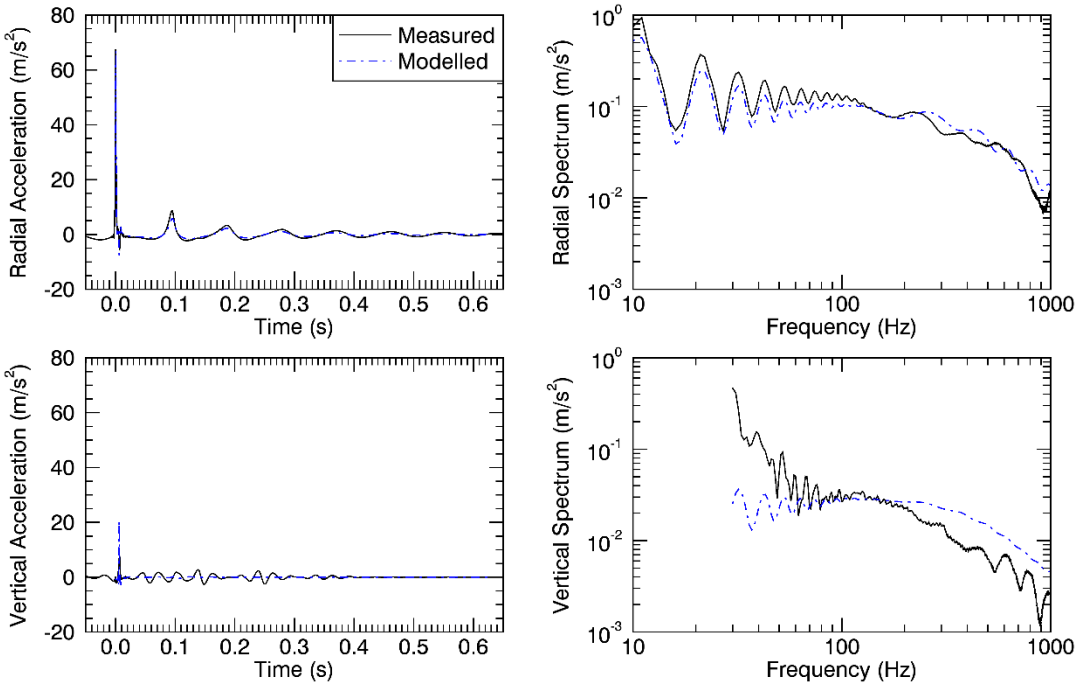

Figure 49. Modelled and measured acceleration (left) waveforms and (right) power spectra for a 150 in^3 airgun at 6 m depth and a receiver at 6 m depth and 4.6 m horizontal range (corresponding to sequence 284). Top and bottom panels are for the radial and vertical directions, respectively. Band-pass filters of 10–1000 Hz and 30–1000 Hz were used for the radial and vertical waveforms, respectively. Measured data are from M20 #2.

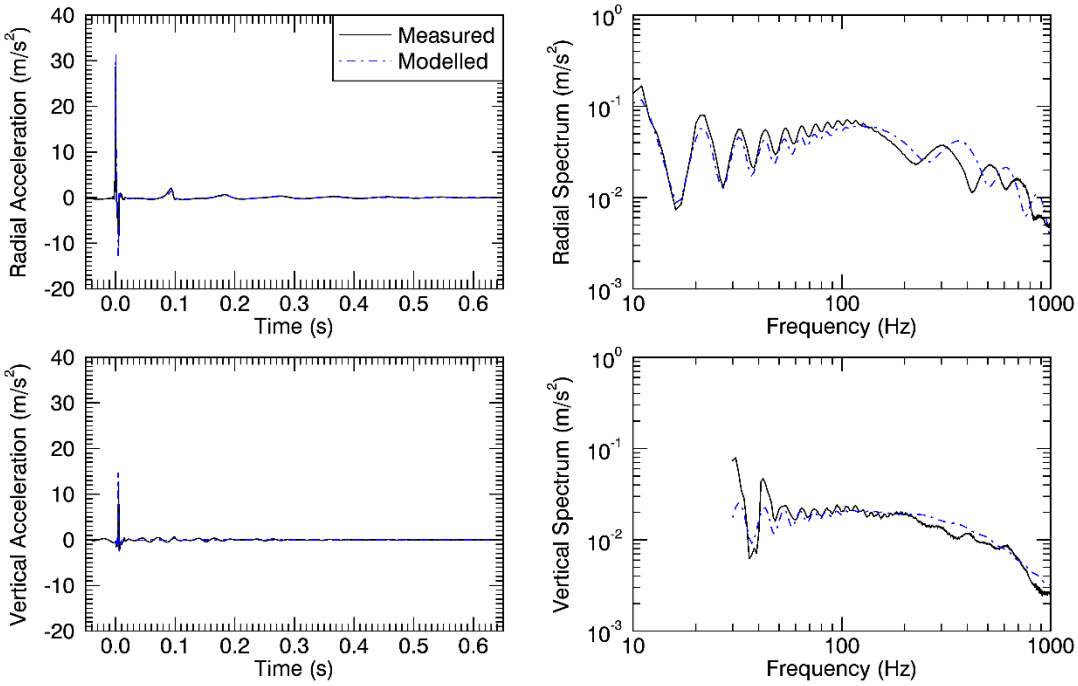

Figure 50. Modelled and measured acceleration (left) waveforms and (right) power spectra for a 150 in^3 airgun at 6 m depth and a receiver at 6 m depth and 9.3 m horizontal range (corresponding to sequence 289). Top and bottom panels are for the radial and vertical directions, respectively. Band-pass filters of 10–1000 Hz and 30–1000 Hz were used for the radial and vertical waveforms, respectively. Measured data are from M20 #2.

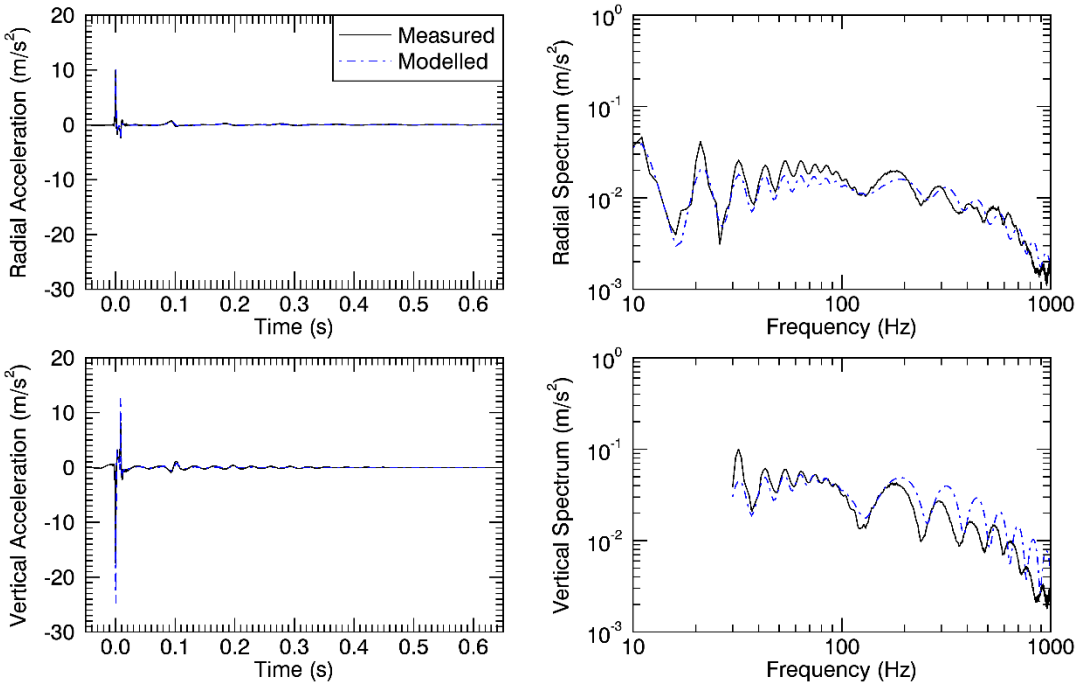

Figure 51. Modelled and measured acceleration (left) waveforms and (right) power spectra for a 150 in^3 airgun at 6 m depth and a receiver at 16 m depth and 4.0 m horizontal range (corresponding to sequence 284). Top and bottom panels are for the radial and vertical directions, respectively. Band-pass filters of 10–1000 Hz and 30–1000 Hz were used for the radial and vertical waveforms, respectively. Measured data are from M20 #4.

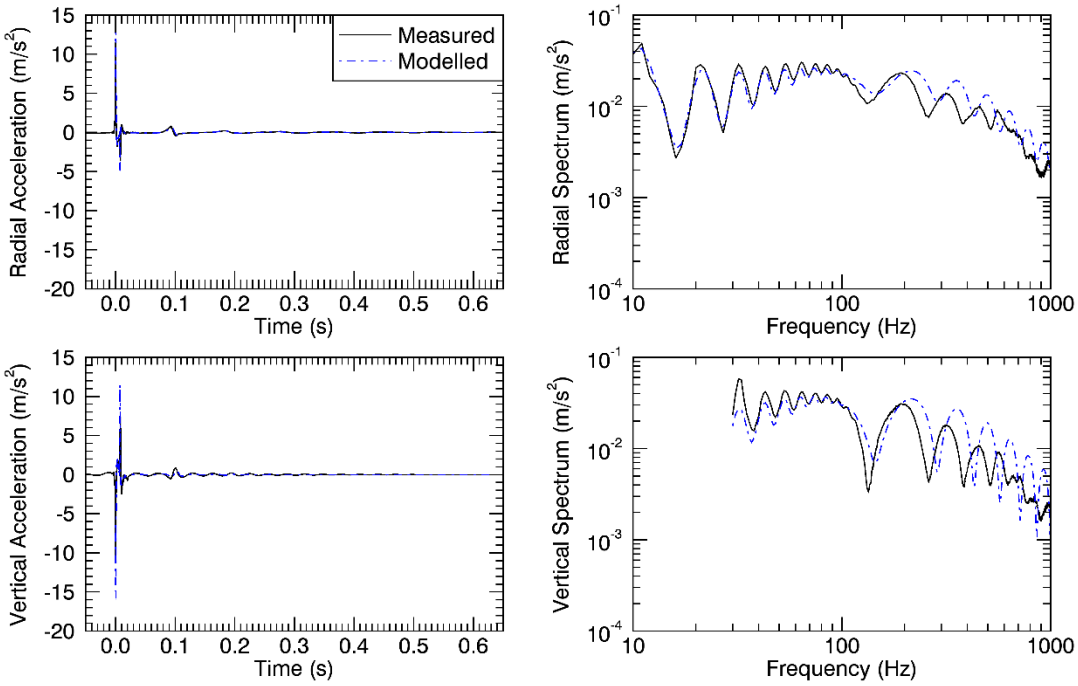

Figure 52. Modelled and measured acceleration (left) waveforms and (right) power spectra for a 150 in^3 airgun at 6 m depth and a receiver at 16 m depth and 9.0 m horizontal range (corresponding to sequence 289). Top and bottom panels are for the radial and vertical directions, respectively. Band-pass filters of 10–1000 Hz and 30–1000 Hz were used for the radial and vertical waveforms, respectively. Measured data are from M20 #4.

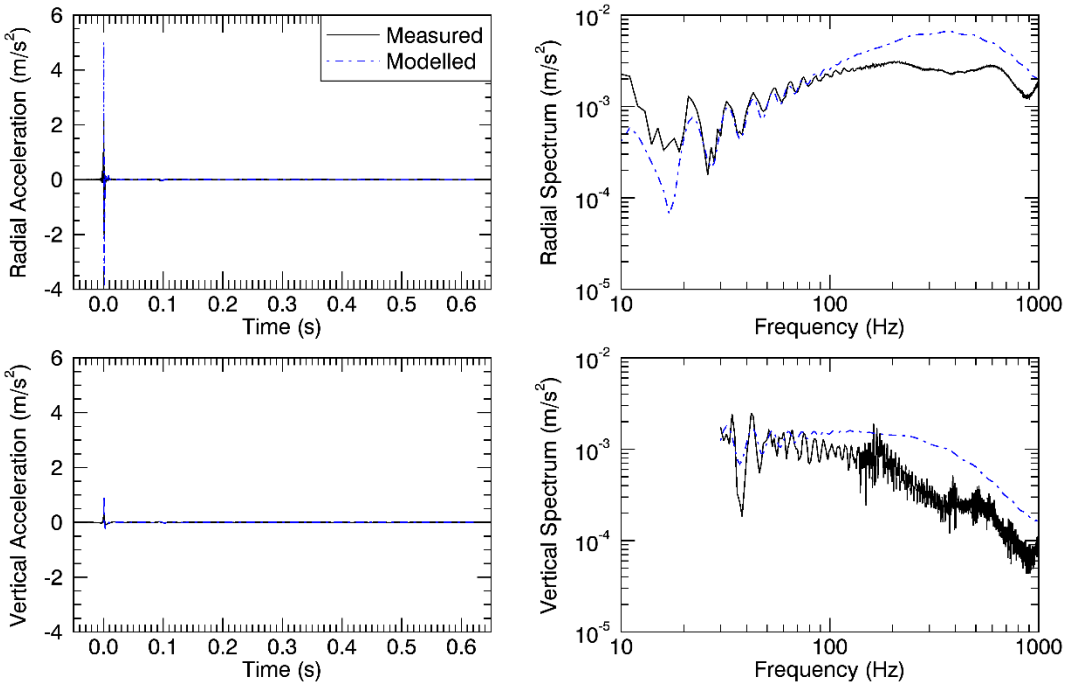

Figure 53. Modelled and measured acceleration (left) waveforms and (right) power spectra for a 150 in^3 airgun at 6 m depth and a receiver at 4 m depth and 54 m horizontal range (corresponding to sequence 289). Top and bottom panels are for the radial and vertical directions, respectively. Band-pass filters of 10–1000 Hz and 30–1000 Hz were used for the radial and vertical waveforms, respectively. Measured data are from M20 #3.

2.4. Discussion

2.4.1. Model Validation

The AASM predictions were in good agreement with pressure and particle motion measurements below 300 Hz, but the model slightly overestimated the measurements in the 300–1000 Hz frequency range. We believe this is because AASM is tuned to match the pressure waveforms, which are dominated by low-frequency sound energy. Most of the high-frequency sound energy is contained the initial peak of the airgun signature (during the initial release of air from the gun chamber), which is very brief in time and, therefore, has less influence in the model tuning procedure. Therefore, the high-frequency predictions may be improved in future by incorporating a tuning procedure that includes the spectral mismatch in addition to the waveform mismatch.

Despite the mismatch at higher frequencies, the model produces pressure and particle motion waveforms that are in good agreement with the measurements. The bubble pulse period and amplitude decay rate, and the spectral frequency oscillation are accurately replicated (e.g., Figure 37). The frequencies of spectral nulls occasionally differed between measurements and the model (e.g., Figure 33 at 200–1000 Hz). In this frequency range, the spectral nulls are caused by interference of the direct signal with its surface reflection and so the frequencies of the nulls are directly related to the source-receiver geometry. Thus, differences in the null frequencies in the spectra are likely due to an error in the logged receiver or source depth.

Higher frequency energy is typically overestimated by the model (e.g., Figure 38; 100–1000 Hz), but it has relatively low amplitude, so broadband levels were unaffected (Figures 27, 40, and 41). One possible reason for this mismatch is that these frequencies may experience losses associated with surface scattering that are not accounted for in the propagation model used for this study. The propagation model used in the model validation procedure assumed a perfectly reflecting sea surface, and neglected scattering losses due to sea surface roughness. Neglecting sea surface roughness, if present, would have particularly affected the long-range hydrophone data from M20 #3 since the surface reflections are predicted to have the highest relative magnitude at longer range and near the sea surface.

The validation comparisons for particle acceleration showed that the model was better able to reproduce the M20 measurements in the horizontal direction than in the vertical direction. We believe this was due to an issue with the way the M20 sensors were deployed during the experiment, rather than an issue with the model. During the Svein Vaage measurements, the M20 sensors were suspended from cables attached to buoyant floats at the sea surface (Figure 51). Because the M20 sensors are negatively buoyant, this arrangement created tension in the cables that was aligned with the vertical accelerometer channels. Since accelerometers measure force directly (force is proportional to acceleration), the cable tension induced an asymmetric, non-acoustic signal on the vertical channels of the M20 sensors. The influence of the cable tension was greatest at frequencies below 30 Hz (which were filtered from the validation comparisons), but in some instances the influence clearly extended to higher frequencies as well. In future, if M20 (or other negatively-buoyant) sensors are used for measuring particle motion from seismic sources, special care must be taken to design a suspension system that does not affect the measurements. For example, the suspension should be designed to exert only symmetrical forces on the accelerometer, and the suspension must have a resonant frequency that is well below the frequency range under measurement.

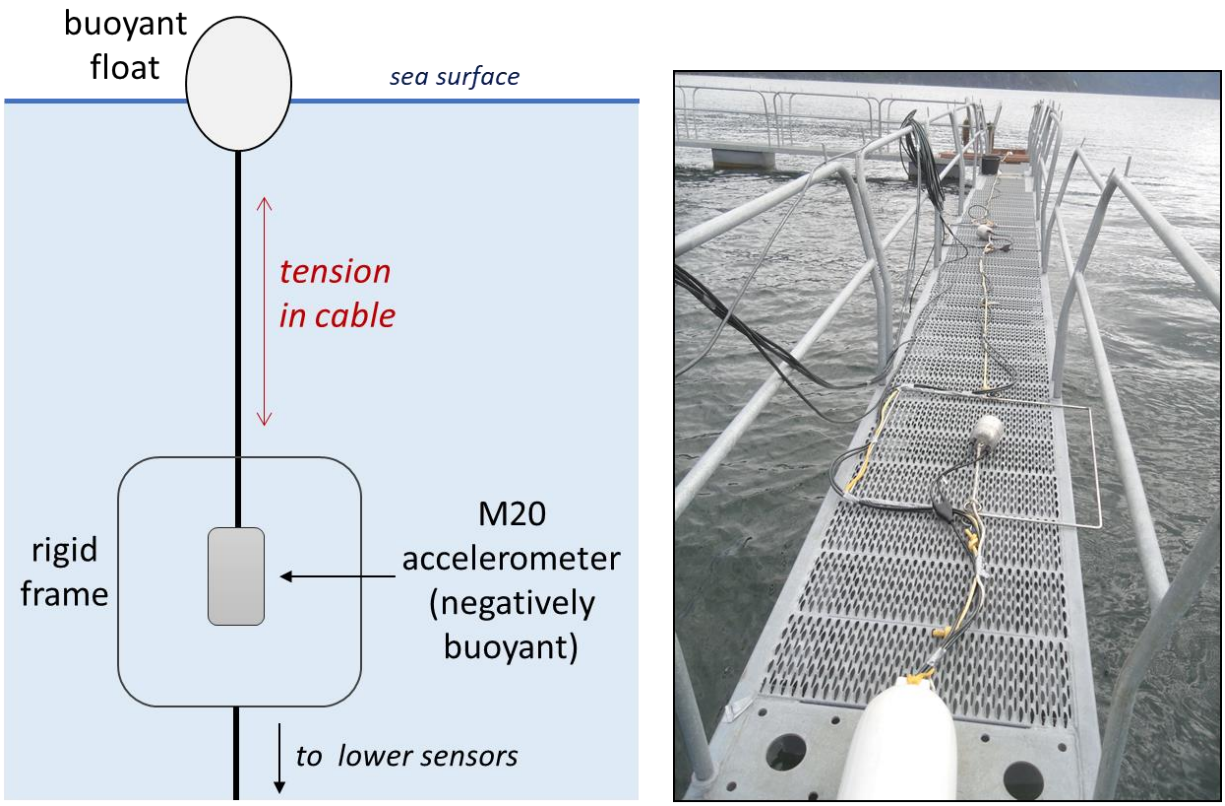

Figure 54. (Left) Side-view diagram showing how M20 sensors were suspended from the sea-surface during deployment. (Right) M20 sensors on barge gangway prior to deployment (reproduced from Lundsten 2010).

We also note there was considerable uncertainty in the calibration of the M20 sensors that were used in the Svein Vaage airgun study. Manufacturer's calibration records were only available for one of the sensors deployed at the measurement site (M20 #3), and that calibration was performed several years after the original measurements (Appendix A). Furthermore, the lowest frequency of the pressure calibration was 1 kHz, below which the sensitivity of the M20 sensor was assumed frequency independent. Thus, out of necessity, the post-trial calibration of M20 #3 was assumed representative of the sensitivity of the other M20 sensors used in the measurements. In addition, we identified a 5.0 dB negative bias in the sensitivity of the M20 pressure sensors that had to be corrected for to obtain results consistent with the calibrated B&K hydrophones. Future studies should use calibrated sensors over the full frequency range of the source spectra for both pressure and particle motion and record accurate source-receiver geometry. Furthermore, all sensors should be subjected to cross-calibration (i.e., where the same acoustic signal is recorded on multiple different sensors, simultaneously), during the experiment, to ensure the consistency of the assumed instrument sensitivities.

2.4.2. Applicability to Environmental Impact Assessments

Particle motion is detectable by all fish and likely all invertebrates, so environmental impact assessments should consider the effects of particle motion on these animals. However, there are currently no corresponding injury criteria, which makes it difficult to quantitatively assess impacts and recommend guidelines for when particle motion modelling and measurements should occur. Particle motion in the far field and away from acoustic boundaries has a simple relationship with pressure, so particle motion modelling and measurements are less important at these locations than when in the near field or close to acoustic boundaries. The near-field distance is dependent on the source and is greater for distributed sources (e.g., airgun arrays) and for sources with substantial low-frequency energy. The seafloor can be a particularly important boundary in shallow water because interface waves (e.g., Scholte waves) can be excited by incident sound waves, particularly when volume or interface scattering is substantial (Paffenholz et al. 2006). Interface waves propagate well along the seafloor and can lead to large-amplitude vertical particle motion that is larger than what pressure alone would indicate. Particle motion should, therefore, be modelled and measured in the near field of the source and at boundaries, such as the water surface or at the seafloor where bottom-dwelling fish and invertebrates live.

2.5. Conclusions

This chapter validated acoustic particle motion predictions from JASCO's Airgun Array Source Model (AASM) using a large collection of accelerometer measurements from the 2010 Svein Vaage single gun experiment (Mattsson and Jenkerson 2008). These particle motion measurements were performed using M20 sensors (GTI), which combine a single omnidirectional pressure sensor (hydrophone) with a 3-axis accelerometer. To perform the validation analysis, it was first necessary to address several calibration issues identified in the original measurements (Chapter 1). After these issues were addressed, comparisons of modelled and measured data showed that the model accurately predicted particle motion from single airguns, with the best agreement between model and data at frequencies below 300 Hz, where the airguns generate most of their acoustic energy. The model was found to slightly overestimate the measurements at higher frequencies, between 300 and 1000 Hz. The mismatch at higher frequencies was likely due to two factors: (1) the greater weighting given to low frequencies in the model tuning procedure, and (2) excess propagation loss, due to sea surface roughness, not accounted for by the propagation model. Both these aspects of the particle motion model may be improved upon in future, as a result of this investigation. Nonetheless, the validation comparisons demonstrated that AASM may be used for accurately modelling exposures of marine organisms to acoustic particle motion from seismic airguns at short range. This is particularly important for fish and invertebrates, which have hearing organs that are sensitive to acoustic particle motion, rather than pressure.

Literature Cited

[ISO] International Organization for Standardization. 2017. *ISO/DIS 18405.2:2017. Underwater acoustics—Terminology*. Geneva. https://www.iso.org/standard/62406.html.

[NMFS] National Marine Fisheries Service. 2018. *2018 Revision to: Technical Guidance for Assessing the Effects of Anthropogenic Sound on Marine Mammal Hearing (Version 2.0): Underwater Thresholds for Onset of Permanent and Temporary Threshold Shifts*. U.S. Department of Commerce, NOAA. NOAA Technical Memorandum NMFS-OPR-59. 167 pp. https://www.fisheries.noaa.gov/webdam/download/75962998.

Ainslie, M.A., M.B. Halvorsen, R.P.A. Dekeling, R.M. Laws, A.J. Duncan, A.S. Frankel, K.D. Heaney, E.T. Küsel, A.O. MacGillivray, et al. 2016. Verification of airgun sound field models for environmental impact assessment. *Proceedings of Meetings on Acoustics* 27(1): 070018. https://doi.org/10.1121/2.0000339

ANSI S1.1-1994. R2004. *American National Standard Acoustical Terminology*. American National Standards Institute, New York.

Delarue, J., K.A. Kowarski, E.E. Maxner, J.T. MacDonnell, and S.B. Martin. 2018. *Acoustic Monitoring Along Canada's East Coast: August 2015 to July 2017*. Document Number 01279, Environmental Studies Research Funds Report Number 215, Version 1.0. Technical report by JASCO Applied Sciences for Environmental Studies Research Fund, Dartmouth, NS, Canada. 120 pp + appendices.

Deveau, T.J., J. Delarue, S.B. Martin, and K. Lucke. 2018. *Transmission Loss Modelling of Seismic Airgun Sounds: Predicted Received Levels, with Frequency Weighting, off Atlantic Canada*. Document Number 01620, Environmental Studies Research Funds Report Number 217, Version 2.0. Technical report by JASCO Applied Sciences for Environmental Studies Research Fund, Dartmouth, NS, Canada. 43 pp + appendices.

Dragoset, W.H. 1984. A comprehensive method for evaluating the design of airguns and airgun arrays. *Proceedings, 16th Annual Offshore Technology Conference* Volume 3, 7-9 May 1984. OTC 4747, Houston, TX, USA. pp 75–84.

Fay, R.R. 1984. The goldfish ear codes the axis of acoustic particle motion in three dimensions. *Science* 225(4665): 951-954. http://science.sciencemag.org/content/225/4665/951.long.

Fewtrell, J.L. and R.D. McCauley. 2012. Impact of air gun noise on the behaviour of marine fish and squid. *Marine Pollution Bulletin* 64(5): 984-993. http://dx.doi.org/10.1016/j.marpolbul.2012.02.009.

Halvorsen, M.B., B.M. Casper, C.M. Woodley, T.J. Carlson, and A.N. Popper. 2012. Threshold for onset of injury in Chinook salmon from exposure to impulsive pile driving sounds. *PLoS ONE* 7(6): e38968. https://doi.org/10.1371/journal.pone.0038968.

Jensen, F.B., W.A. Kuperman, M.B. Porter, and H. Schmidt. 1994. *Computational Ocean Acoustics*. 1st edition. Modern Acoustics and Signal Processing. AIP Press, New York. 612 pp.

Landro, M. 1992. Modeling of GI gun signatures. *Geophysical Prospecting* 40: 721–747. https://doi.org/10.1111/j.1365-2478.1992.tb00549.x

Laws, R.M., L. Hatton, and M. Haartsen. 1990. Computer modeling of clustered airguns. *First Break* 8(9): 331–338.

Lundsten, T. 2010. *JIP Recording Overview*. rev 7 edition. PGS Geophysical.

MacGillivray, A.O. 2006. *Acoustic Modelling Study of Seismic Airgun Noise in Queen Charlotte Basin*. MSc Thesis. University of Victoria, Victoria, BC. 98 pp.

MacGillivray, A.O. in press. An Airgun Array Source Model Accounting for High-frequency Sound Emissions During Firing and Solutions to the IAMW Source Test Cases. *IEEE Journal of Oceanic Engineering*.

Matthews, M.-N.R. and A.O. MacGillivray. 2013. Comparing modeled and measured sound levels from a seismic survey in the Canadian Beaufort Sea. *Proceedings of Meetings on Acoustics* 19(1): 1-8. https://doi.org/10.1121/1.4800553

Mattsson, A. and M. Jenkerson. 2008. *Single Airgun and Cluster Measurement Project*. *Joint Industry Programme (JIP) on Exploration and Production Sound and Marine Life Proramme Review*, October 28-30. International Association of Oil and Gas Producers, Houston, TX.

McCauley, R.D., J. Fewtrell, A.J. Duncan, C. Jenner, M.-N. Jenner, J.D. Penrose, R.I.T. Prince, A. Adhitya, J. Murdoch, et al. 2000. Marine seismic surveys: A study of environmental implications. *Australian Petroleum Production Exploration Association (APPEA) Journal* 40(1): 692-708. https://doi.org/10.1071/AJ99048.

Mooney, T.A., R. Hanlon, P.T. Madsen, J. Christensen-Dalsgaard, D.R. Ketten, and P.E. Nachtigall. 2012. Potential for Sound Sensitivity in Cephalopods. (Chapter 28) *In* Popper, A.N. and A.D. Hawkins (eds.). *The Effects of Noise on Aquatic Life*. Volume 730. Springer, New York. pp 125-128. https://link.springer.com/chapter/10.1007%2F978-1-4419-7311-5_28.

Mueller-Blenkle, C., P.K. McGregor, A.B. Gill, M.H. Andersson, J. Metcalfe, V. Bendall, P. Sigray, D.T. Wood, and F. Thomsen. 2010. *Effects of Pile-driving Noise on the Behaviour of Marine Fish*. COWRIE Ref: Fish 06-08; Cefas Ref: C3371. 62 pp.

Paffenholz, J., P. Docherty, R. Shurtleff, and D. Hays. 2006. Shear Wave Noise on OBS Vz Data - Part II Elastic Modeling of Scatterers in the Seabed. *68th EAGE Conference and Exhibition incorporating SPE EUROPEC 2006*.

Popper, A.N., R.R. Fay, C. Platt, and O. Sand. 2003. Sound detection mechanisms and capabilities of teleost fishes. *In* Collin, S.P. and N.J. Marshall (eds.). *Sensory Processing in Aquatic Environments*. Springer-Verlag, New York. pp 3-38.

Popper, A.N., M.B. Halvorsen, A. Kane, D.L. Miller, M.E. Smith, J. Song, P. Stein, and L.E. Wysocki. 2007. The effects of high-intensity, low-frequency active sonar on rainbow trout. *Journal of the Acoustical Society of America* 122(1): 623-635. http://dx.doi.org/10.1121/1.2735115.

Popper, A.N., A.D. Hawkins, R.R. Fay, D.A. Mann, S. Bartol, T.J. Carlson, S. Coombs, W.T. Ellison, R.L. Gentry, et al. 2014. *Sound Exposure Guidelines for Fishes and Sea Turtles: A Technical Report prepared by ANSI-Accredited Standards Committee S3/SC1 and registered with ANSI*. ASA S3/SC1.4 TR-2014. SpringerBriefs in Oceanography. ASA Press and Springer. https://doi.org/10.1007/978-3-319-06659-2.

Popper, A.N. and A.D. Hawkins. 2018. The importance of particle motion to fishes and invertebrates. *Journal of the Acoustical Society of America* 143(1): 470-488.

Racca, R.G., M.E. Austin, A. Rutenko, and K. Bröker. 2015. Monitoring the gray whale sound exposure mitigation zone and estimating acoustic transmission during a 4-D seismic survey, Sakhalin Island, Russia. *Endangered Species Research* 29(2): 131-146. https://doi.org/10.3354/esr00703.

Sarà, G., J.M. Dean, D. D'Amato, G. Buscaino, A. Oliveri, S. Genovese, S. Ferro, G. Buffa, M. Lo Martire, et al. 2007. Effect of boat noise on the behaviour of bluefin tuna *Thunnus thynnus* in the Mediterranean Sea. *Marine Ecology Progress Series* 331: 243-253. http://www.jstor.org/stable/24871131.

Ziolkowski, A. 1970. A method for calculating the output pressure waveform from an air gun. *Geophysical Journal of the Royal Astronomical Society* 21(2): 137-161. https://doi.org/10.1111/j.1365-246X.1970.tb01773.x.

Ziolkowski, A., G. Parkes, L. Hatton, and T. Haugland. 1982. The signature of an air gun array: Computation from near-field measurements including interactions. *Geophysics* 47(10): 1413-1421. https://doi.org/10.1190/1.1441289.

Glossary

azimuth
A horizontal angle relative to a reference direction, which is often magnetic north or the direction of travel. In navigation it is also called bearing.

bar
Unit of pressure equal to 100 kPa, which is approximately equal to the atmospheric pressure on Earth at sea level. 1 bar is equal to 10^6 Pa or 10^{11} µPa.

broadband sound level
The total sound pressure level measured over a specified frequency range. If the frequency range is unspecified, it refers to the entire measured frequency range.

decibel (dB)
One-tenth of a bel. Unit of level when the base of the logarithm is the tenth root of ten, and the quantities concerned are proportional to power (ANSI S1.1-1994 R2004).

frequency
The rate of oscillation of a periodic function measured in cycles-per-unit-time. The reciprocal of the period. Unit: hertz (Hz). Symbol: *f*. 1 Hz is equal to 1 cycle per second.

hertz (Hz)
A unit of frequency defined as one cycle per second.

hydrophone
An underwater sound pressure transducer. A passive electronic device for recording or listening to underwater sound.

particle acceleration
The rate of change of particle velocity. Unit: metres per second squared (m/s^2). Symbol: *a*.

particle velocity
The physical speed of a particle in a material moving back and forth in the direction of the pressure wave. Unit: metres per second (m/s). Symbol: *v*.

peak pressure level (PK)
The maximum instantaneous sound pressure level, in a stated frequency band, within a stated period. Also called zero-to-peak pressure level. Unit: decibel (dB).

power spectrum density
The acoustic signal power per unit frequency as measured at a single frequency. Unit: $\mu Pa^2/Hz$, or $\mu Pa^2 \cdot s$.

power spectral density level
The decibel level ($10\log_{10}$) of the power spectrum density, usually presented in 1 Hz bins. Unit: dB re 1 $\mu Pa^2/Hz$.

pressure, acoustic
The deviation from the ambient hydrostatic pressure caused by a sound wave. Also called overpressure. Unit: pascal (Pa). Symbol: *p*.

pressure, hydrostatic
The pressure at any given depth in a static liquid that is the result of the weight of the liquid acting on a unit area at that depth, plus any pressure acting on the surface of the liquid. Unit: pascal (Pa).

received level
The sound level measured at a receiver.

rms
root-mean-square.

signature
Pressure signal generated by a source.

sound
A time-varying pressure disturbance generated by mechanical vibration waves travelling through a fluid medium such as air or water.

spectrum
An acoustic signal represented in terms of its power (or energy) distribution compared with frequency.

transmission loss (TL)
The decibel reduction in sound level between two stated points that results from sound spreading away from an acoustic source subject to the influence of the surrounding environment. Also called propagation loss.

Appendix A. GeoSpectrum's Calibration Report

Calibration of M20 directional data recorded during the Svein Vaage airgun study

Contractor report

Provided as a deliverable under Jasco project P001276

Authorized by:

Signature: _____

Prepared by: Matt Coffin

GeoSpectrum Technologies Inc.
10 Akerley Blvd., Unit 19
Dartmouth, NS B3B 1J4
Phone: (902) 406-4111
Fax: (902) 435-8987

Project Manager: Joe Hood, (902) 406-4111 Ext 230
Project Authority: Alex MacGillivray, Project Manager / Project Scientist, (250) 483-3300 Ext 2011
Submitted: 21 Dec 2016

GeoSpectrum Document number: 2016-351
Document version: R1

Calibration of M20 directional data recorded during the Svein Vaage airgun study, Contractor report, 2016-351, R1

Document distribution and history

DOCUMENT DISTRIBUTION	
Copies	**Provided to**
1	GeoSpectrum Technologies Inc. Project # 811
1	Jasco Project Authority (Alex MacGillivray)

DOCUMENT HISTORY				
Document Version	**Date**	**Prepared**	**Approved**	**Description of change**
0	Nov 30, 2016	MC	JH	Original Draft
1	Dec 21, 2016	MC	JH	Addressed comments from PA

Table of contents

List of figures

List of tables

Contractor report

1 Introduction

This contractor report documents work performed under project P001276 for Project Authority (PA) Alex MacGillivray. The work was performed from Nov-Dec 2016.

The objectives of this contract were to calibrate GeoSpectrum Technologies Inc. M20 directional data collected during Svein Vaage broadband airgun study conducted by PGS in 2010. The M20 is a directional sensor comprised of a single omni-directional hydrophone, and three directional accelerometers. During the study, multiple M20 sensors were stationed at various positions relative to an airgun source and recorded seismic pulses. GeoSpectrum was tasked with applying the correct calibration to convert the recorded directional data into physical units. This was achieved by:

- Obtaining the M20 time-series data from JASCO, with accompanying information regarding gains that had already been applied to the data.
- Undoing the applied corrections.
- Applying the frequency dependent magnitude and phase calibrations to the directional M20 data.

This task flow has been captured in IDL programs which read in the data provided by the PA, perform the data manipulation, and write the output back to IDL *.sav* files in the same format provided by the PA. Note that the PA provided considerable background information pertaining to the field study and the resulting data to facilitate this analysis. For brevity, much of this information is omitted from this report, and only information directly relevant to the processing discussed herein is provided.

2 M20 sensitivity characteristics

The M20 consists of an omni-directional hydrophone and three directional accelerometers. The frequency response of the omni hydrophone is shown in Figure 1, while the frequency dependent response of the directional sensors is shown in Figure 2. Both sensitivity curves assume a 0 dB pre-amp gain. Additionally, there is a frequency-dependent phase response of signals received on the directional channels, shown in Figure 3, where the phase flips by 180 degrees as a received signal passes through the resonant frequency of the directional sensors.

The curves shown in Figures Figure 1 and Figure 2 are a combination of in-water and in-air calibration. GeoSpectrum measured the sensitivity of M20 S/N 3 (named *BOW DEEP* during the field study) on March 11th, 2016. Data from 1-5 kHz were measured in GeoSpectrum's calibration tank, and in-air measurements using a shaker table were recorded at frequencies between 10 and 40 Hz. Although six M20s were employed during the field study, sensitivity measurements exist only for M20 S/N 3. Also, there is an approximately 5-year span between the field survey and the time of calibration. Therefore, the processing discussed herein assumes that:

- The sensitivity of all six M20s agrees reasonably well with the single, known sensitivity curve.
- The sensitivity of M20 S/N 3 has not changed in the time between the field study and the sensitivity measurement.

GeoSpectrum believes that these caveats have a low probability of affecting the results of this analysis.

The phase response of M20 S/N 3 was not measured. Therefore, the curve shown in Figure 3 was by adjusting the zero-crossing point of a newer M20 phase response to the resonant frequency of the directional M20 sensors used during the field study, which is approximately 2.4 kHz based on Figure 2[1]. Points below the lowest measured frequency, which is 1475 Hz after the adjustment, are extrapolated to a theoretical value of 90 degrees at 10 Hz.

[1] Newer versions of the M20 have a resonance at approximately 1 kHz.

Contractor report

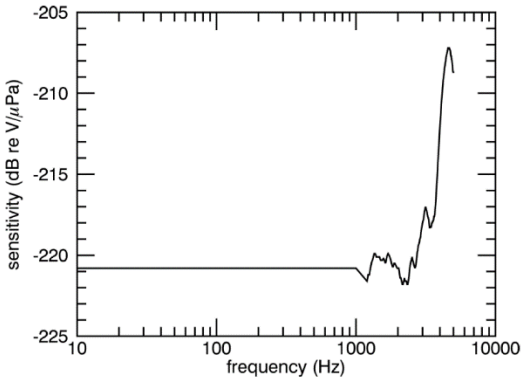

Figure 1: Sensitivity of the M20 omni-directional hydrophone with a 0 dB pre-amplifier gain.

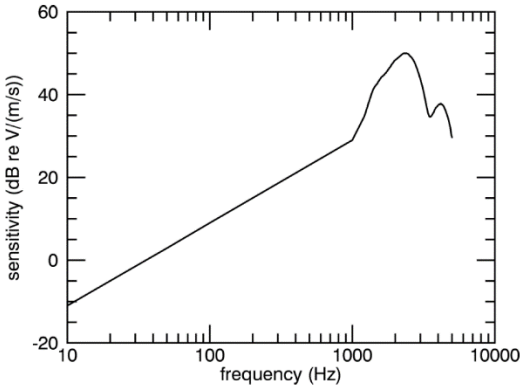

Figure 2: Sensitivity of the M20 directional sensors with a 0 dB pre-amplifier gain.

GeoSpectrum Technologies Inc. 3/20

Calibration of M20 directional data recorded during the Svein Vaage airgun study, Contractor report, 2016-351, R1

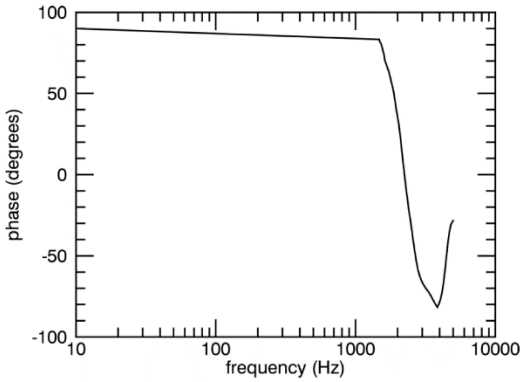

Figure 3: Phase response of the M20 directional sensors.

4/20 GeoSpectrum Technologies Inc.

3 Data calibration procedure

This section provides a brief overview of the data and how GeoSpectrum processed the directional time-series data to achieve physical units. Where applicable, the data processing procedure was validated using synthetic data such that the effects of the processing could be assessed without features of the real data set biasing the assessment. All processing described herein was performed using IDL, including its built-in *FFT* function for forward and inverse spectral processing.

3.1 Data overview

Data were provided in IDL *.sav* files, along with an accompanying IDL program, *load_jip_trace_from_sav.pro*, which loads the time-series data and accompanying metadata into IDL structures for further processing. The data are arranged with respect to sequence, shot, and channel number. This analysis focuses on sequences 282 to 307, which contain data for six M20 sensors[2]. Since each M20 has four data channels (i.e. the omni and three directional senors), there are 24 channels of interest in sequences. Three of the M20s had a 0 dB pre-amplifier gain, while the other three had a 20 dB gain. The relationship between channel number, sensor type, and preamplifier gain is shown in Table 1.

Table 1: Channel mapping and pre-amplifier gains for the six M20s used during sequences 282 to 307. Channel number is provided in the inner cells.

SENSOR TYPE	PRE-AMPLIFIER GAIN					
	0 dB	20 dB	0 db	0 db	20 db	20 db
SIN	25	29	33	37	41	45
COS	26	30	34	38	42	46
VERT	27	31	35	39	43	47
OMNI	28	32	36	40	44	48

The calibration is performed in two primary steps:

- Undoing the gains already applied to the time-series data to convert back to voltage levels.
- Applying the correct frequency-dependent magnitude and phase calibration curves to the raw voltage levels.

The following sections describe each of these steps.

[2] GeoSpectrum also processed data from sequences 188-204, which contain data for one, 0 dB M20. However, the bulk of the analysis was focused on sequences 282-307.

3.2 Reversal of pre-applied gains

Based on the supporting documentation, and in conjunction with conversations with the PA, GeoSpectrum assumed that:

- The data provided by the PA were in physical units (e.g. the directional data were intended to be in units of m/s^2, and the omni-directional data were intended to be in units of Pa).
- The sensitivity values provided represent and end-to-end system calibration that have been applied to the data to achieve presumed physical units. In other words, by reversing these calibration factors, the data can be converted back to voltage levels that would have been output directly by the M20.
- A single gain value was assumed for each sensor, rather than a frequency dependent sensitivity curve.

The calibration factors for the omni-directional hydrophone and directional accelerometers are shown in Table 2. In order to convert back to voltage levels, the calibration software reverses these gains.

Table 2: Assumed sensitivities of the M20 channels.

SENSOR	ASSUMED SENSITIVITY
Omni	7.08×10^{-6} V/Pa
directional (0 dB pre-amp)	8.4×10^{-3} V/(m/s^2)
directional (20 dB pre-amp)	8.4×10^{-2} V/(m/s^2)

3.3 Application of M20 phase and magnitude responses

Once the data are converted back to units of Volts, the magnitude and phase, if applicable, sensitivity curves are applied to convert the data to physical units. The phase and magnitude corrections are applied separately using the following procedure:

- Zero-pad the voltage time series by approximately 400%, with an equal amount of zeroes before and after the data.
- Compute the frequency spectrum of the zero-padded time series using an FFT.
- Compute the phase of the complex-valued spectrum from the arctangent of the real and imaginary components.
- Add the phase correction shown in Figure 3 to the spectrum (directional channels only)
- Scale the spectrum by the sensitivity curve shown in Figure 2 (directional) or Figure 1 (omni). For this and the previous step, the calibration curves shown in Figure 1 toFigure 3 are interpolated to the frequency scale of the data.
- Compute the inverse FFT to convert back to the time domain and then remove the zero padding.

4 Results

Data from B&K omni-directional hydrophones were compared to the corrected M20 omni-directional data. This check serves primarily to understand if the gain applied by PGS was correctly interpreted and subsequently reversed. Figure 4 and Figure 5 show a sample comparison between two B&K hydrophones (Figure 4) and six M20s (Figure 5). The comparison shows that predominant features visible in both the B&K and M20 time-series data are on the same order of magnitude. However, spectral analysis conducted by the PA indicates that while the M20 omni data agree well with the B&K data at all frequencies, the M20 directional data, when converted to µPa, are consistently higher than the B&K data by approximately 20 dB. Furthermore, the output of the M20 pre-amplifiers is limited to +/- 1V. However, after undoing the PGS gains to revert the data to units of Volts, the data regularly exceed this value, suggesting that the assumed directional sensitivity is incorrect. This effect is illustrated in the centre column of Figure 6, which is a diagnostic plot showing data for sequence 289, shot 11[3]. The plot shows the waveforms at three stages: before any corrections, after reversal of the assumed gain, and after application of the frequency-dependent sensitivity and phase curves. The centre column, which shows the signal levels in apparent Volts, clearly exceeds the 1 V limit for the directional sensors (channels 41, 42, and 43 – rows 1 to 3), while the voltage levels on the omni channel (channel 44 – row 4) are within the expected range of the pre-amplifier.

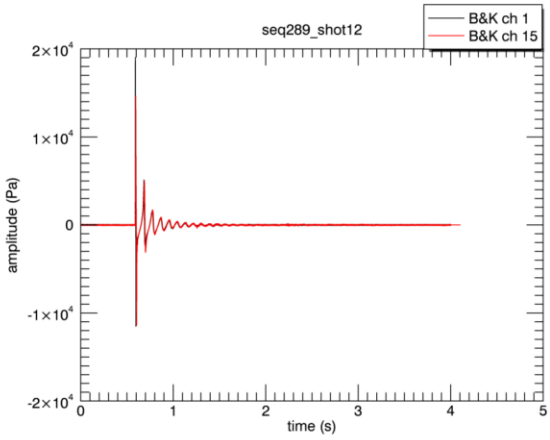

Figure 4: Calibrated time-series data recorded on two B&K hydrophones for a single shot.

[3] A diagnostic plot was generated for each shot, but due to the large number of plots, only one is included here as an example.

Calibration of M20 directional data recorded during the Svein Vaage airgun study, Contractor report, 2016-351, R1

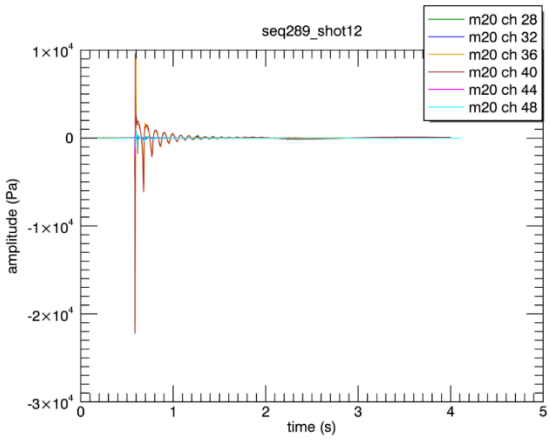

Figure 5: Calibrated time-series data recorded on six M20 omni-directional hydrophones for a single shot.

Figure 6 also shows that the accelerometer data, once corrected, contain significant low-frequency content with the seismic return often superimposed on the lower-frequency signals. A 10 Hz high-pass filter was effective in removing these low-frequency oscillations and enhanced the seismic return, although this step was only performed for data QA, and processed data provided to the PA do not have a high-pass filter applied.

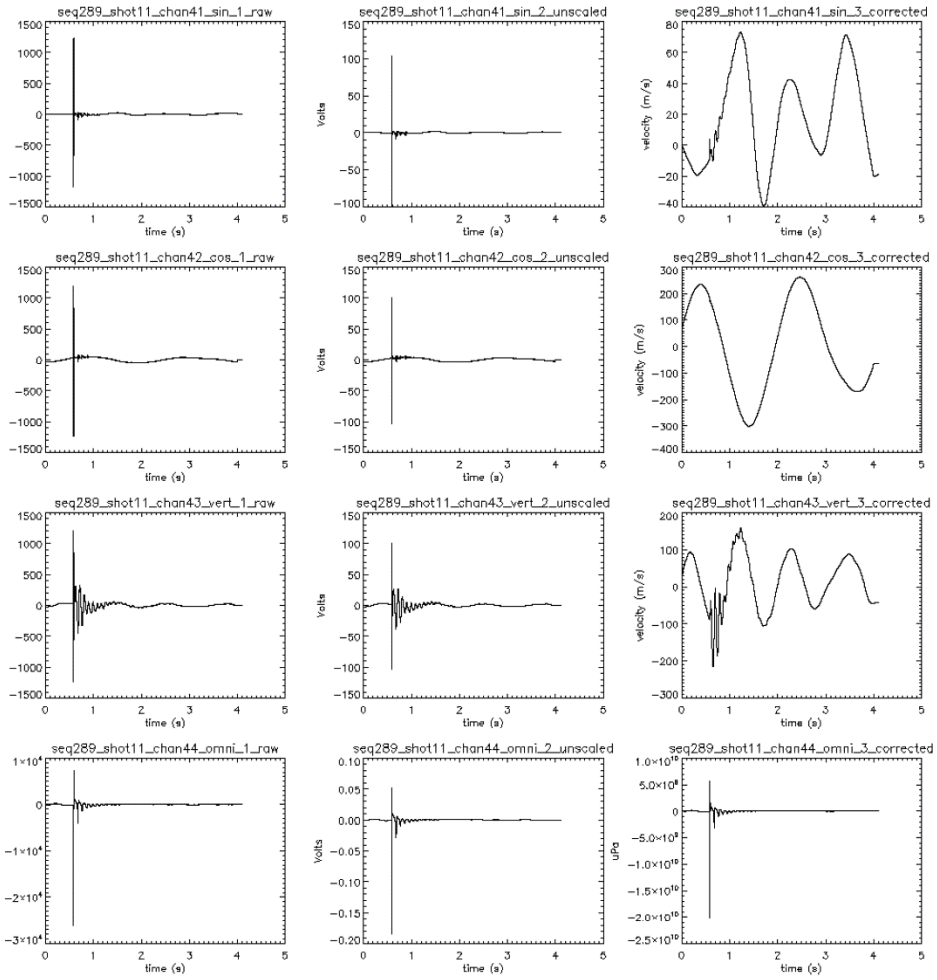

Figure 6: Sample diagnostic plot generated during data processing.
All plots show data for the same shot. The left column shows the raw time-series data, the centre column shows the data after the gain reversal, and the right column shows the data after the frequency-dependent sensitivities are applied. Each row shows data for a specific sensor, ordered sin, cos, vert, and omni from top to bottom.

5 Summary and conclusions

This report documents the effort undertaken by GeoSpectrum to calibrate M20 directional data recorded during a field study. Attempts to calibrate the data were performed by reversing sensitivities that had already been applied to the data, and then applying frequency-dependent sensitivity curves and phase curves for the directional sensors.

The results of the calibration procedure indicate that the procedure itself is reasonable, as a comparison between the calibrated M20 omni-directional hydrophone and reference B&K hydrophones show comparable signal levels. However, there is an outstanding discrepancy between the directional and omni-directional sensor data which will have to be corrected prior to further analyses of these data. The source of the discrepancy is unknown at the time of writing of this report, but it is believed to be due to an unaccounted gain applied during initial processing.

Contractor report

Annex A M20 omni-directional hydrophone sensitivity data

The following is the M20 omni-direcitonal hydrophone sensitivity in text form. The data are presented in two columns. The first column is frequency in Hz, while the second column is the sensitivity in dBV re 1 uPa. These data are plotted in Figure 1. These values assume a 0 dB pre-amplifier gain.

```
10.0,-220.8
20.0,-220.8
30.0,-220.8
50.0,-220.8
100.0,-220.8
1000.0,-220.8
1200.0,-221.6
1225.0,-221.2
1250.0,-221.2
1275.0,-220.7
1300.0,-220.4
1325.0,-220.2
1350.0,-219.9
1375.0,-219.9
1400.0,-220.1
1425.0,-220.1
1450.0,-220.1
1475.0,-220.1
1500.0,-220.3
1525.0,-220.3
1550.0,-220.3
1575.0,-220.2
1600.0,-220.3
1625.0,-220.5
1650.0,-220.3
1675.0,-220.0
1700.0,-219.9
1725.0,-220.0
1750.0,-220.1
1775.0,-220.3
1800.0,-220.5
1825.0,-220.7
1850.0,-220.7
1875.0,-220.5
1900.0,-220.5
1925.0,-220.6
1950.0,-220.7
1975.0,-220.8
2000.0,-220.8
2025.0,-220.8
2050.0,-221.1
```

GeoSpectrum Technologies Inc. 11/20

Calibration of M20 directional data recorded during the Svein Vaage airgun study, Contractor report, 2016-351, R1

```
2075.0,-221.4
2100.0,-221.4
2125.0,-221.6
2150.0,-221.8
2175.0,-221.8
2200.0,-221.6
2225.0,-221.4
2250.0,-221.6
2275.0,-221.6
2300.0,-221.6
2325.0,-221.8
2350.0,-221.8
2375.0,-221.6
2400.0,-221.3
2425.0,-220.9
2450.0,-220.6
2475.0,-220.4
2500.0,-220.3
2525.0,-220.1
2550.0,-220.3
2575.0,-220.4
2600.0,-220.6
2625.0,-220.7
2650.0,-220.8
2675.0,-220.7
2700.0,-220.5
2725.0,-220.2
2750.0,-219.8
2775.0,-219.7
2800.0,-219.4
2825.0,-219.3
2850.0,-219.2
2875.0,-219.0
2900.0,-218.9
2925.0,-218.6
2950.0,-218.4
2975.0,-218.2
3000.0,-218.0
3025.0,-217.9
3050.0,-217.8
3075.0,-217.5
3100.0,-217.3
3125.0,-217.2
3150.0,-217.0
3175.0,-217.1
3200.0,-217.2
3225.0,-217.3
3250.0,-217.5
3275.0,-217.6
3300.0,-217.7
3325.0,-217.8
3350.0,-218.1
```

12/20 GeoSpectrum Technologies Inc.

Contractor report

```
3375.0,-218.3
3400.0,-218.3
3425.0,-218.2
3450.0,-218.3
3475.0,-218.2
3500.0,-218.0
3525.0,-218.0
3550.0,-217.9
3575.0,-217.9
3600.0,-217.8
3625.0,-217.6
3650.0,-217.6
3675.0,-217.5
3700.0,-217.1
3725.0,-216.8
3750.0,-216.5
3775.0,-216.0
3800.0,-215.5
3825.0,-215.1
3850.0,-214.7
3875.0,-214.2
3900.0,-213.8
3925.0,-213.3
3950.0,-212.9
3975.0,-212.5
4000.0,-212.1
4025.0,-211.7
4050.0,-211.4
4075.0,-211.0
4100.0,-210.6
4125.0,-210.3
4150.0,-210.0
4175.0,-209.7
4200.0,-209.5
4225.0,-209.2
4250.0,-209.0
4275.0,-208.8
4300.0,-208.6
4325.0,-208.4
4350.0,-208.3
4375.0,-208.1
4400.0,-208.0
4425.0,-207.8
4450.0,-207.7
4475.0,-207.6
4500.0,-207.5
4525.0,-207.4
4550.0,-207.3
4575.0,-207.2
4600.0,-207.2
4625.0,-207.2
4650.0,-207.2
```

GeoSpectrum Technologies Inc. 13/20

Calibration of M20 directional data recorded during the Svein Vaage airgun study, Contractor report, 2016-351, R1

```
4675.0,-207.2
4700.0,-207.3
4725.0,-207.3
4750.0,-207.4
4775.0,-207.6
4800.0,-207.7
4825.0,-207.7
4850.0,-207.9
4875.0,-208.0
4900.0,-208.2
4925.0,-208.3
4950.0,-208.6
4975.0,-208.7
5000.0,-208.7
```

Contractor report

Annex B M20 directional accelerometer sensitivity data

The following is the M20 directional accelerometer sensitivity in text form. The data are presented in two columns. The first column is frequency in Hz, while the second column is the sensitivity in dBV re 1 m/s. These data are plotted in Figure 2. These values assume a 0 dB pre-amplifier gain.

```
10.0,-11.0
20.0,-5.0
30.0,-1.5
50.0,2.9
100.0,9.0
1000.0,29.0
1200.0,34.4
1225.0,35.1
1250.0,36.1
1275.0,37.0
1300.0,38.0
1325.0,38.8
1350.0,39.7
1375.0,40.5
1400.0,41.2
1425.0,41.7
1450.0,42.1
1475.0,42.4
1500.0,42.7
1525.0,43.2
1550.0,43.5
1575.0,43.9
1600.0,44.2
1625.0,44.4
1650.0,44.6
1675.0,44.8
1700.0,45.1
1725.0,45.3
1750.0,45.6
1775.0,45.9
1800.0,46.2
1825.0,46.5
1850.0,46.7
1875.0,47.1
1900.0,47.4
1925.0,47.6
1950.0,47.9
1975.0,48.2
2000.0,48.3
2025.0,48.5
2050.0,48.6
2075.0,48.8
```

Calibration of M20 directional data recorded during the Svein Vaage airgun study, Contractor report, 2016-351, R1

```
2100.0,48.9
2125.0,49.1
2150.0,49.2
2175.0,49.4
2200.0,49.5
2225.0,49.7
2250.0,49.8
2275.0,49.9
2300.0,50.0
2325.0,50.0
2350.0,49.9
2375.0,50.0
2400.0,50.0
2425.0,49.9
2450.0,49.9
2475.0,49.8
2500.0,49.6
2525.0,49.4
2550.0,49.3
2575.0,49.1
2600.0,49.0
2625.0,48.8
2650.0,48.6
2675.0,48.4
2700.0,48.1
2725.0,47.9
2750.0,47.6
2775.0,47.2
2800.0,46.9
2825.0,46.5
2850.0,46.2
2875.0,45.8
2900.0,45.4
2925.0,45.0
2950.0,44.6
2975.0,44.2
3000.0,43.8
3025.0,43.3
3050.0,42.9
3075.0,42.4
3100.0,42.0
3125.0,41.5
3150.0,41.0
3175.0,40.4
3200.0,39.8
3225.0,39.3
3250.0,38.7
3275.0,38.1
3300.0,37.6
3325.0,37.0
3350.0,36.5
3375.0,36.0
```

16/20 GeoSpectrum Technologies Inc.

```
3400.0,35.5
3425.0,35.2
3450.0,34.9
3475.0,34.7
3500.0,34.6
3525.0,34.6
3550.0,34.7
3575.0,34.8
3600.0,34.9
3625.0,35.1
3650.0,35.2
3675.0,35.4
3700.0,35.6
3725.0,35.7
3750.0,36.0
3775.0,36.2
3800.0,36.4
3825.0,36.6
3850.0,36.8
3875.0,36.9
3900.0,37.0
3925.0,37.1
3950.0,37.2
3975.0,37.3
4000.0,37.4
4025.0,37.5
4050.0,37.6
4075.0,37.6
4100.0,37.7
4125.0,37.7
4150.0,37.7
4175.0,37.8
4200.0,37.7
4225.0,37.7
4250.0,37.6
4275.0,37.6
4300.0,37.5
4325.0,37.4
4350.0,37.3
4375.0,37.2
4400.0,37.0
4425.0,36.8
4450.0,36.6
4475.0,36.4
4500.0,36.2
4525.0,36.0
4550.0,35.8
4575.0,35.5
4600.0,35.3
4625.0,35.0
4650.0,34.8
4675.0,34.6
```

Calibration of M20 directional data recorded during the Svein Vaage airgun study, Contractor report, 2016-351, R1

```
4700.0,34.3
4725.0,34.0
4750.0,33.7
4775.0,33.4
4800.0,33.0
4825.0,32.7
4850.0,32.3
4875.0,31.9
4900.0,31.4
4925.0,30.9
4950.0,30.3
4975.0,30.0
5000.0,29.7
```

18/20 GeoSpectrum Technologies Inc.

Annex C M20 directional accelerometer phase data

The following is the M20 directional accelerometer phase response in text form. The data are presented in two columns. The first column is frequency in Hz, while the second column is the phase response, in degrees, relative to the omni-directional hydrophone.

```
10,90
1475,83.3
1500,81.4
1525,80.7
1550,78.3
1575,76.0
1600,73.7
1625,70.0
1650,68.6
1675,67.0
1700,65.2
1725,63.9
1750,62.0
1775,59.7
1800,57.4
1825,55.3
1850,53.3
1875,50.7
1900,47.7
1925,44.5
1950,41.2
1975,38.1
2000,35.4
2025,32.9
2050,29.7
2075,26.1
2100,22.3
2125,18.1
2150,13.8
2175,9.7
2200,6.0
2225,2.4
2250,-1.2
2275,-5.0
2300,-8.5
2325,-11.7
2350,-14.6
2375,-17.5
2400,-21.4
2450,-25.9
2500,-31.2
2550,-36.7
2600,-41.9
2650,-46.8
```

Calibration of M20 directional data recorded during the Svein Vaage airgun study, Contractor report, 2016-351, R1

```
2700,-51.4
2750,-55.3
2800,-58.7
2850,-61.1
2900,-63.2
2950,-64.8
3000,-66.3
3050,-67.4
3100,-68.4
3150,-69.4
3200,-70.3
3250,-71.0
3300,-71.8
3350,-72.6
3400,-73.5
3450,-74.4
3500,-75.4
3550,-76.5
3600,-77.4
3650,-78.3
3700,-79.3
3750,-80.1
3800,-80.9
3850,-81.7
3900,-80.7
3950,-79.7
4000,-78.4
4050,-76.9
4100,-75.2
4150,-73.0
4200,-70.4
4250,-67.4
4300,-64.1
4350,-60.4
4400,-56.4
4450,-52.4
4500,-48.3
4550,-44.5
4600,-41.0
4650,-37.9
4700,-35.3
4750,-33.1
4800,-31.2
4850,-30.3
4900,-29.5
4950,-28.9
5000,-28.4
```

20/20 GeoSpectrum Technologies Inc.

Appendix B. Measured Acceleration Data

Tables B-1 and B-2 list peak, broadband rms, and band-limited rms acceleration for the 60 and 150 in^3 airguns, respectively. The corrections described in Section 2.2.3 have not been applied for these data. Note that broadband rms acceleration (30–1000 Hz) is related to the band-limited acceleration with the following formula:

$$a^2_{30\text{–}1000Hz} = a^2_{30\text{–}100Hz} + a^2_{100\text{–}300Hz} + a^2_{300\text{–}1000Hz} \ . \qquad \text{(B-1)}$$

Table B-1. 60 in^3 airgun (sequences 298–307): Peak, broadband rms, and band-limited rms acceleration. Acceleration units are m/s^2. Acceleration in the 10–30 Hz band is for the horizontal component only.

Sequence	Horizontal range (m)	Depth below surface (m)	Peak	rms (30–1000 Hz)	rms 10–30 Hz (horizontal)	rms (30–100 Hz)	rms (100–300 Hz)	rms (300–1000 Hz)
298	1.00	6	70.4827	1.7099	1.8318	1.1428	1.0561	0.7080
298	54.01	8	2.5783	0.0685	0.0037	0.0139	0.0425	0.0518
298	1.00	16	11.9956	0.3360	0.0476	0.1982	0.2215	0.1566
299	2.00	6	46.2364	1.1060	0.8484	0.6556	0.7171	0.5283
299	54.01	7	2.4061	0.0636	0.0038	0.0124	0.0363	0.0508
299	2.00	16	11.4734	0.3373	0.0491	0.1908	0.2244	0.1642
300	3.00	6	33.0329	0.7873	0.4562	0.4300	0.5302	0.3923
300	54.01	6	1.9331	0.0550	0.0032	0.0107	0.0304	0.0446
300	3.00	16	11.1393	0.3287	0.0499	0.1808	0.2197	0.1645
301	4.00	6	29.4523	0.6937	0.3707	0.3749	0.4669	0.3501
301	54.01	5	1.5471	0.0467	0.0033	0.0093	0.0256	0.0379
301	4.00	16	10.9089	0.3094	0.0490	0.1762	0.2052	0.1502
302	5.00	6	24.3039	0.6083	0.2681	0.3136	0.4155	0.3146
302	54.01	4	1.6336	0.0393	0.0035	0.0082	0.0219	0.0316
302	5.00	16	10.4530	0.3096	0.0489	0.1717	0.2071	0.1530
303	6.00	6	23.7528	0.5754	0.2395	0.3030	0.3871	0.2989
303	54.01	4	1.5110	0.0390	0.0037	0.0083	0.0217	0.0313
303	6.00	16	10.3559	0.2889	0.0480	0.1674	0.1848	0.1459
304	7.00	6	20.1070	0.5026	0.1728	0.2507	0.3409	0.2712
304	54.01	5	1.6291	0.0475	0.0031	0.0097	0.0266	0.0380
304	7.00	16	9.5715	0.2748	0.0456	0.1600	0.1760	0.1376
305	8.00	6	17.5087	0.4605	0.1533	0.2261	0.3144	0.2491
305	54.01	6	1.8826	0.0548	0.0037	0.0111	0.0317	0.0432
305	8.00	16	9.2798	0.2620	0.0357	0.1563	0.1634	0.1323
306	9.00	6	16.3540	0.4311	0.1302	0.2083	0.2973	0.2325
306	54.01	7	2.3792	0.0625	0.0042	0.0127	0.0377	0.0482
306	9.00	16	8.7207	0.2537	0.0355	0.1521	0.1580	0.1276
307	13.60	6	9.7673	0.2895	0.0427	0.1168	0.2244	0.1406
307	54.01	8	2.5013	0.0680	0.0038	0.0141	0.0423	0.0513
307	13.60	16	6.5777	0.2032	0.0290	0.1198	0.1344	0.0940

Table B-2. 150 in^3 airgun (sequences 282–296): Peak, broadband rms, and band-limited rms acceleration. Acceleration units are m/s^2. Acceleration in the 10–30 Hz band is for the horizontal component only.

Sequence	Horizontal range (m)	Depth below surface (m)	Peak	rms (30–1000 Hz)	rms 10–30 Hz (horizontal)	rms (30–100 Hz)	rms (100–300 Hz)	rms (300–1000 Hz)
282	2.00	6	64.0057	1.7075	1.5764	1.2712	0.9489	0.6314
282	54.01	8	2.4671	0.0698	0.0060	0.0155	0.0438	0.0520
282	2.00	16	14.0756	0.3885	0.0653	0.2542	0.2420	0.1667
283	3.00	6	54.3861	1.4180	1.1301	1.0250	0.8095	0.5510
283	54.01	7	2.5200	0.0650	0.0054	0.0140	0.0387	0.0502
283	3.00	16	14.0774	0.3860	0.0581	0.2500	0.2426	0.1661
284	4.00	6	46.1902	1.1862	0.8374	0.8212	0.7049	0.4835
284	54.01	6	2.4283	0.0608	0.0052	0.0129	0.0353	0.0477
284	4.00	16	13.8842	0.3851	0.0585	0.2438	0.2445	0.1703
285	5.00	6	34.9973	0.8717	0.5177	0.5483	0.5587	0.3832
285	54.01	5	3.0634	0.0679	0.0061	0.0115	0.0309	0.0590
285	5.00	16	13.2793	0.3612	0.0531	0.2286	0.2277	0.1625
286	6.00	6	28.9818	0.7110	0.3670	0.4126	0.4720	0.3351
286	54.01	4	1.5526	0.0388	0.0061	0.0105	0.0231	0.0293
286	6.00	16	12.5232	0.3466	0.0548	0.2205	0.2120	0.1629
287	7.00	6	24.5956	0.6241	0.2609	0.3510	0.4187	0.3013
287	54.01	4	1.6583	0.0395	0.0052	0.0097	0.0235	0.0302
287	7.00	16	12.0876	0.3345	0.0573	0.2146	0.2056	0.1536
288	8.00	6	22.5624	0.5653	0.2069	0.3054	0.3829	0.2822
288	54.01	4	1.6843	0.0399	0.0050	0.0099	0.0239	0.0304
288	8.00	16	11.2453	0.3203	0.0559	0.2060	0.1959	0.1476
289	9.00	6	19.4452	0.5411	0.1614	0.2787	0.3690	0.2798
289	54.01	4	1.7241	0.0412	0.0048	0.0095	0.0228	0.0330
289	9.00	16	10.8544	0.3165	0.0518	0.1983	0.1992	0.1454
290	2.00	6	63.1914	1.6173	1.4186	1.1776	0.9155	0.6217
290	54.01	5	2.5800	0.0700	0.0049	0.0150	0.0423	0.0534
290	2.00	16	14.2365	0.3887	0.0547	0.2545	0.2422	0.1660
291	3.00	6	48.4659	1.1959	0.8933	0.8214	0.7162	0.4915
291	54.01	5	2.7703	0.0681	0.0047	0.0151	0.0396	0.0533
291	3.00	16	14.0011	0.3746	0.0481	0.2416	0.2356	0.1625
292	4.00	6	36.9435	0.8739	0.5527	0.5393	0.5694	0.3854
292	54.01	5	2.5475	0.0671	0.0055	0.0150	0.0397	0.0520
292	4.00	16	13.2356	0.3546	0.0503	0.2255	0.2222	0.1597
293	5.00	6	33.7399	0.7904	0.4576	0.4721	0.5188	0.3640
293	54.01	5	2.6351	0.0680	0.0046	0.0150	0.0400	0.0529
293	5.00	16	13.2044	0.3455	0.0476	0.2221	0.2149	0.1543
294	6.00	7	30.0949	0.7310	0.3704	0.4199	0.4902	0.3429
294	54.01	5	2.9754	0.0745	0.0049	0.0153	0.0410	0.0603
294	6.00	16	12.6387	0.3502	0.0526	0.2207	0.2181	0.1622
295	7.00	7	26.8165	0.6423	0.2789	0.3645	0.4363	0.2988
295	54.01	5	2.8015	0.0728	0.0053	0.0154	0.0410	0.0581
295	7.00	16	11.9023	0.3257	0.0512	0.2099	0.2044	0.1421
296	8.00	7	24.1846	0.6043	0.2271	0.3295	0.4211	0.2810
296	54.01	5	2.9776	0.0750	0.0051	0.0155	0.0416	0.0604
296	8.00	16	11.8639	0.3297	0.0546	0.2089	0.2100	0.1441

Appendix C. Modelled Acceleration Data

Sections C.1 and C.2 contain modelled acceleration data and the ratio between modelled and measured acceleration for the 60 and 150 in^3 airguns, respectively. Receiver positions and measured acceleration data have been corrected as described in Section 2.2.3.

C.1. 60 in^3 Airgun

Table C.1-1. Modelled peak, broadband rms, and band-limited rms acceleration for the 60 in^3 airgun. Acceleration units are m/s^2. Acceleration in the 10–30 Hz band is for the horizontal component only.

Sequence	Horizontal range (m)	Depth below surface (m)	Peak	rms (30–1000 Hz)	rms 10–30 Hz (horizontal)	rms (30–100 Hz)	rms (100–300 Hz)	rms (300–1000 Hz)
298	3.37	6	116.8470	2.6144	1.4750	1.1055	1.5646	1.8018
298	54.01	8	7.6038	0.2128	0.0034	0.0231	0.1171	0.1762
298	1.00	16	36.7878	0.8637	0.0180	0.3149	0.4905	0.6391
299	3.43	6	114.3930	2.5599	1.4184	1.0734	1.5332	1.7681
299	54.01	7	7.5352	0.2134	0.0030	0.0209	0.1064	0.1838
299	2.00	16	36.2372	0.8531	0.0344	0.3111	0.4822	0.6329
300	5.19	6	73.3699	1.6845	0.6108	0.6084	1.0170	1.2040
300	54.01	6	7.3243	0.2114	0.0025	0.0186	0.0944	0.1882
300	3.00	16	35.3715	0.8367	0.0482	0.3052	0.4694	0.6234
301	5.70	6	66.4355	1.5426	0.5018	0.5423	0.9272	1.1125
301	54.01	5	6.8940	0.2032	0.0021	0.0164	0.0814	0.1855
301	4.00	16	34.2567	0.8159	0.0587	0.2975	0.4535	0.6110
302	6.62	6	56.7380	1.3481	0.3640	0.4546	0.7984	0.9901
302	54.01	4	6.6735	0.1853	0.0017	0.0143	0.0675	0.1720
302	5.00	16	32.9657	0.7916	0.0657	0.2886	0.4361	0.5956
303	6.88	6	54.5151	1.3032	0.3350	0.4350	0.7686	0.9615
303	54.01	4	6.6735	0.1853	0.0017	0.0143	0.0675	0.1720
303	6.00	16	31.5684	0.7643	0.0697	0.2789	0.4190	0.5764
304	7.93	6	47.0164	1.1493	0.2446	0.3703	0.6704	0.8591
304	54.01	5	6.8940	0.2032	0.0021	0.0164	0.0814	0.1855
304	7.00	16	30.1242	0.7354	0.0711	0.2687	0.4036	0.5541
305	8.69	6	42.7477	1.0632	0.1986	0.3337	0.6189	0.7992
305	54.01	6	7.3243	0.2114	0.0025	0.0186	0.0944	0.1882
305	8.00	16	28.6795	0.7067	0.0705	0.2584	0.3904	0.5304
306	9.33	6	39.7360	1.0039	0.1687	0.3077	0.5863	0.7560
306	54.01	7	7.5352	0.2134	0.0030	0.0209	0.1064	0.1838
306	9.00	16	27.2677	0.6793	0.0686	0.2480	0.3798	0.5065
307	14.54	6	25.1837	0.6982	0.0571	0.1764	0.4749	0.4809
307	54.01	8	7.6038	0.2128	0.0034	0.0231	0.1171	0.1762
307	13.60	16	21.6286	0.5615	0.0529	0.2031	0.3420	0.3970

Table C.1-2. Ratio of modelled to measured peak, broadband rms, and band-limited rms acceleration for the 60 in^3 airgun. A ratio of 1.0 indicates agreement between measured and modelled acceleration. Acceleration in the 10–30 Hz band is for the horizontal component only.

Sequence	Horizontal range (m)	Depth below surface (m)	Peak	rms (30–1000 Hz)	rms 10–30 Hz (horizontal)	rms (30–100 Hz)	rms (100–300 Hz)	rms (300–1000 Hz)
298	3.37	6	0.932	0.860	0.453	0.544	0.833	1.431
298	54.01	8	1.658	1.747	0.512	0.933	1.549	1.911
298	1.00	16	1.725	1.446	0.212	0.894	1.245	2.295
299	3.43	6	1.391	1.302	0.940	0.921	1.202	1.882
299	54.01	7	1.761	1.886	0.444	0.944	1.649	2.036
299	2.00	16	1.776	1.422	0.394	0.917	1.208	2.168
300	5.19	6	1.249	1.203	0.753	0.796	1.079	1.726
300	54.01	6	2.131	2.160	0.449	0.979	1.745	2.374
300	3.00	16	1.786	1.432	0.543	0.949	1.202	2.131
301	5.70	6	1.268	1.251	0.761	0.813	1.117	1.787
301	54.01	5	2.506	2.448	0.357	0.990	1.792	2.750
301	4.00	16	1.766	1.483	0.673	0.950	1.243	2.288
302	6.62	6	1.313	1.246	0.763	0.815	1.081	1.770
302	54.01	4	2.297	2.651	0.269	0.980	1.737	3.058
302	5.00	16	1.773	1.438	0.755	0.945	1.184	2.189
303	6.88	6	1.291	1.274	0.787	0.807	1.116	1.809
303	54.01	4	2.484	2.674	0.258	0.967	1.752	3.090
303	6.00	16	1.714	1.488	0.816	0.937	1.275	2.222
304	7.93	6	1.315	1.286	0.796	0.831	1.106	1.781
304	54.01	5	2.380	2.408	0.379	0.950	1.720	2.741
304	7.00	16	1.770	1.505	0.876	0.945	1.290	2.264
305	8.69	6	1.373	1.298	0.729	0.830	1.107	1.804
305	54.01	6	2.188	2.171	0.385	0.946	1.674	2.448
305	8.00	16	1.738	1.517	1.111	0.930	1.344	2.255
306	9.33	6	1.366	1.310	0.729	0.831	1.109	1.829
306	54.01	7	1.781	1.920	0.399	0.926	1.588	2.143
306	9.00	16	1.758	1.505	1.086	0.917	1.352	2.233
307	14.54	6	1.450	1.356	0.751	0.849	1.190	1.924
307	54.01	8	1.709	1.759	0.495	0.925	1.554	1.930
307	13.60	16	1.849	1.554	1.028	0.953	1.431	2.375

C.2. 150 in^3 Airgun

Table C.2-1. Modelled peak, broadband rms, and band-limited rms acceleration for the 150 in^3 airgun. Acceleration units are m/s^2. Acceleration in the 10–30 Hz band is for the horizontal component only.

Sequence	Horizontal range (m)	Depth below surface (m)	Peak	rms (30–1000 Hz)	rms 10–30 Hz (horizontal)	rms (30–100 Hz)	rms (100–300 Hz)	rms (300–1000 Hz)
282	3.59	6	87.4756	2.4470	1.7526	1.2741	1.6442	1.3044
282	54.01	8	5.3641	0.1955	0.0036	0.0290	0.1274	0.1454
282	2.00	16	28.1285	0.8254	0.0444	0.3899	0.5363	0.4929
283	4.12	6	74.8608	2.1011	1.3242	1.0439	1.4293	1.1429
283	54.01	7	5.1146	0.1892	0.0032	0.0261	0.1157	0.1474
283	3.00	16	27.4457	0.8088	0.0620	0.3824	0.5226	0.4859
284	4.64	6	65.4327	1.8496	1.0322	0.8849	1.2683	1.0222
284	54.01	6	5.1146	0.1797	0.0027	0.0233	0.1027	0.1457
284	4.00	16	26.5671	0.7878	0.0753	0.3727	0.5055	0.4767
285	5.69	6	52.3719	1.5118	0.6737	0.6838	1.0413	0.8610
285	54.01	5	5.1150	0.1657	0.0023	0.0206	0.0886	0.1386
285	5.00	16	25.5508	0.7636	0.0841	0.3614	0.4868	0.4652
286	6.66	6	44.1653	1.3060	0.4786	0.5669	0.8947	0.7667
286	54.01	4	5.2625	0.1459	0.0019	0.0180	0.0735	0.1247
286	6.00	16	24.4520	0.7374	0.0887	0.3491	0.4682	0.4511
287	7.65	6	38.0786	1.1543	0.3511	0.4835	0.7873	0.6938
287	54.01	4	5.2625	0.1459	0.0019	0.0180	0.0735	0.1247
287	7.00	16	23.3176	0.7102	0.0901	0.3363	0.4511	0.4342
288	8.31	6	34.9073	1.0752	0.2909	0.4403	0.7341	0.6521
288	54.01	4	5.2625	0.1459	0.0019	0.0180	0.0735	0.1247
288	8.00	16	22.1844	0.6829	0.0889	0.3232	0.4361	0.4151
289	9.34	6	30.8517	0.9749	0.2208	0.3848	0.6724	0.5930
289	54.01	4	5.2625	0.1459	0.0019	0.0180	0.0735	0.1247
289	9.00	16	21.0783	0.6561	0.0860	0.3102	0.4234	0.3944
290	3.74	6	83.4805	2.3361	1.6125	1.1990	1.5760	1.2534
290	54.01	5	5.1150	0.1657	0.0023	0.0206	0.0886	0.1386
290	2.00	16	28.1285	0.8254	0.0444	0.3899	0.5363	0.4929
291	4.51	6	67.6623	1.9084	1.0988	0.9214	1.3064	1.0506
291	54.01	5	5.1150	0.1657	0.0023	0.0206	0.0886	0.1386
291	3.00	16	27.4457	0.8088	0.0620	0.3824	0.5226	0.4859
292	5.57	6	53.6001	1.5431	0.7050	0.7018	1.0630	0.8755
292	54.01	5	5.1150	0.1657	0.0023	0.0206	0.0886	0.1386
292	4.00	16	26.5671	0.7878	0.0753	0.3727	0.5055	0.4767
293	6.10	6	48.5330	1.4150	0.5793	0.6283	0.9730	0.8165
293	54.01	5	5.1150	0.1657	0.0023	0.0206	0.0886	0.1386
293	5.00	16	25.5508	0.7636	0.0841	0.3614	0.4868	0.4652
294	6.57	7	44.2511	1.2950	0.4859	0.5802	0.8993	0.7320
294	54.01	5	5.1150	0.1657	0.0023	0.0206	0.0886	0.1386
294	6.00	16	24.4520	0.7374	0.0887	0.3491	0.4682	0.4511
295	7.37	7	39.2597	1.1705	0.3819	0.5118	0.8082	0.6765
295	54.01	5	5.1150	0.1657	0.0023	0.0206	0.0886	0.1386

Sequence	Horizontal range (m)	Depth below surface (m)	Peak	rms (30–1000 Hz)	rms 10–30 Hz (horizontal)	rms (30–100 Hz)	rms (100–300 Hz)	rms (300–1000 Hz)
295	7.00	16	23.3176	0.7102	0.0901	0.3363	0.4511	0.4342
296	7.97	7	36.1500	1.0936	0.3220	0.4697	0.7501	0.6442
296	54.01	5	5.1150	0.1657	0.0023	0.0206	0.0886	0.1386
296	8.00	16	22.1844	0.6829	0.0889	0.3232	0.4361	0.4151

Table C.2-2. Ratio of modelled to measured peak, broadband rms, and band-limited rms acceleration for the 150 in^3 airgun (corresponding to sequences 282–296). A ratio of 1.0 indicates agreement between measured and modelled acceleration. Acceleration in the 10–30 Hz band is for the horizontal component only.

Sequence	Horizontal range (m)	Depth below surface (m)	Peak	rms (30–1000 Hz)	rms 10–30 Hz (horizontal)	rms (30–100 Hz)	rms (100–300 Hz)	rms (300–1000 Hz)
282	3.59	6	0.769	0.806	0.625	0.564	0.974	1.162
282	54.01	8	1.223	1.575	0.337	1.051	1.637	1.574
282	2.00	16	1.124	1.195	0.382	0.863	1.246	1.663
283	4.12	6	0.774	0.833	0.659	0.573	0.993	1.166
283	54.01	7	1.141	1.637	0.333	1.047	1.681	1.652
283	3.00	16	1.096	1.178	0.601	0.860	1.211	1.645
284	4.64	6	0.797	0.877	0.693	0.606	1.012	1.189
284	54.01	6	1.184	1.663	0.297	1.020	1.638	1.718
284	4.00	16	1.076	1.150	0.724	0.860	1.162	1.574
285	5.69	6	0.842	0.975	0.732	0.701	1.048	1.264
285	54.01	5	0.939	1.373	0.213	1.004	1.609	1.321
285	5.00	16	1.082	1.189	0.890	0.889	1.203	1.610
286	6.66	6	0.857	1.033	0.733	0.773	1.066	1.286
286	54.01	4	1.906	2.116	0.172	0.959	1.789	2.397
286	6.00	16	1.098	1.196	0.910	0.890	1.242	1.557
287	7.65	6	0.871	1.040	0.757	0.775	1.057	1.295
287	54.01	4	1.785	2.075	0.199	1.039	1.757	2.321
287	7.00	16	1.085	1.194	0.884	0.881	1.234	1.590
288	8.31	6	0.870	1.070	0.791	0.811	1.078	1.300
288	54.01	4	1.757	2.056	0.208	1.023	1.731	2.310
288	8.00	16	1.109	1.199	0.895	0.882	1.252	1.582
289	9.34	6	0.892	1.013	0.769	0.776	1.025	1.192
289	54.01	4	1.716	1.990	0.218	1.062	1.815	2.125
289	9.00	16	1.092	1.166	0.934	0.880	1.195	1.525
290	3.74	6	0.743	0.812	0.639	0.573	0.968	1.134
290	54.01	5	1.115	1.330	0.265	0.772	1.177	1.458
290	2.00	16	1.111	1.194	0.457	0.862	1.245	1.670
291	4.51	6	0.785	0.897	0.692	0.631	1.026	1.202
291	54.01	5	1.038	1.368	0.276	0.768	1.257	1.462
291	3.00	16	1.102	1.214	0.726	0.890	1.247	1.681
292	5.57	6	0.816	0.993	0.717	0.732	1.050	1.278
292	54.01	5	1.129	1.389	0.237	0.772	1.256	1.500
292	4.00	16	1.129	1.249	0.843	0.930	1.279	1.678
293	6.10	6	0.809	1.007	0.712	0.748	1.055	1.261
293	54.01	5	1.092	1.371	0.282	0.774	1.246	1.473
293	5.00	16	1.088	1.243	0.994	0.915	1.274	1.695
294	6.57	7	0.827	0.996	0.738	0.777	1.032	1.200
294	54.01	5	0.967	1.251	0.262	0.758	1.214	1.292
294	6.00	16	1.088	1.184	0.948	0.890	1.207	1.564
295	7.37	7	0.823	1.025	0.770	0.790	1.042	1.273
295	54.01	5	1.027	1.280	0.246	0.751	1.216	1.342
295	7.00	16	1.102	1.226	0.990	0.901	1.241	1.718

Sequence	Horizontal range (m)	Depth below surface (m)	Peak	rms (30–1000 Hz)	rms 10–30 Hz (horizontal)	rms (30–100 Hz)	rms (100–300 Hz)	rms (300–1000 Hz)
296	7.97	7	0.841	1.018	0.797	0.802	1.002	1.289
296	54.01	5	0.966	1.243	0.255	0.748	1.198	1.290
296	8.00	16	1.052	1.165	0.916	0.870	1.168	1.620